A MODULAR OPEN SOURCE ARCHITECTURE FOR RAPID PROTOTYPING OF MEDICAL CAPSULE ROBOTS

By

Marco Beccani

Dissertation
Submitted to the Faculty of the
Graduate School of Vanderbilt University
in partial fulfillment of the requirements
for the degree of

DOCTOR OF PHILOSOPHY
in

Mechanical Engineering

December, 2015

Nashville, Tennessee

Approved:

Dr. Pietro Valdastri

Dr. Akos Lédeczi

Dr. Dr. Keith L. Obstein

Dr. Nilanjan Sarkar

Dr. Karl E. Zelik

ABSTRACT

Over the last decade, researchers have started exploring the design space of Medical Capsule Robots (MCRs): devices that can operate autonomously within the human body and can diagnose, prevent, monitor, and cure diseases. MCRs are miniature multifunctional devices whose applications are spanning from abdominal surgery to gastrointestinal (GI) endoscopy. MCRs are severely resource constrained devices in size and consequently, in available power and computational capacity. Although the research in the area of MCR is an active topic and has grown exponentially, available devices provide only diagnostic functionalities. In fact, the design process of an MCR is expensive and time consuming. Research groups that are active in this field are usually forced to follow a custom approach to develop MCRs from the ground up. The current state of the art lacks a platform to systematize the design of MCRs which could open this research field to a wider community and, at the same time, create better designs through advanced tool support.

This dissertation focuses on a modular open source architecture to enable the rapid prototyping of MCRs. The advantages of the proposed architecture include module reusability and a reconfigurable software library. Users will be able to build a capsule with functions of their own design by choosing components available from a hardware/software library or by introducing their own. This will prevent the need to design custom modules and face some of the technical challenges typical for MCR development. This doctoral dissertation describes the modular architecture in details and presents some applications where it was successfully adopted for the design of MCRs. Some of these include an MCR to restore wireless tissue palpation in Minimally Invasive Surgery (MIS), a drug delivery MCR, a module for magnetic localization, a wireless capsule for the measurement of resistant properties in the GI tract, and an embedded cane for gait patterns recognition.

Contents

List of Tables

List of Figures

Chapter I

INTRODUCTION

I.1 Background and Motivations: WCE

The GI tract, is home to some of the most deadly human diseases. Colorectal cancer (CRC) alone strikes more than 170,000 people in the USA each year and kills approximately 50,000 [2] with a projected 62% increase by 2030 [3]. Like other cancers of the GI tract, screening is crucial for CRC and increases the 5-year survival rate from 5%, in cases of late diagnosis, to 90%, in cases of early detection [4]. Currently, the preferred method for CRC screening is colonoscopy, but patient compliance with CRC screening programs is low. Third of the population at risk avoids the procedure due to the unpleasant preparations required of the patient, the pain and the potential risk of perforations when the leading tip of the endoscope is obstructed the need for sedation, and the perceived indignity of the procedure.

An appealing alternative to the conventional GI tract screening procedure, since its introduction in 2000 [5], is WCE. WCE entails the ingestion of a miniature pill-sized camera which moves passively through the digestive system. WCE enables visualization of the GI tract without discomforts such as intubation, insufflation, or sedation, thus offering an appealing alternative to traditional flexible scopebased endoscopy. Once the patient has swallowed the capsule, he/she can go back to normal activities without needing to stay in the hospital.

Clinical capsules have also been developed for purposes besides visualization. Given Imaging [6] Ltds Bravo ®and SmartPill ®Capsule collect non-visual data from the GI tract. The Bravo ®adheres to the esophagus by pinning suctioned tissue and remains fixed in esophagus and transmits pH data wirelessly to an external receiver. Such procedure has a duration of 48 h, but can be extended to 96 h[2]. Similarly, the SmartPill ®wirelessly transfers motility and pH data from throughout the digestive tract. Medimetrics [7] introduced IntelliCap ®which has been developed to study drug absorption in the GI tract. The Enterion ™Capsule (Quotient Clinical, England) is used in assessment of drug absorption in the GI tract. The CorTemp ®(HQ Inc., Palmetto, FL) telemetry capsule, originally developed by the Johns Hopkins Applied Physics Laboratory in collaboration with the Goddard Space Flight Center, is an FDA cleared device that monitors internal body temperature

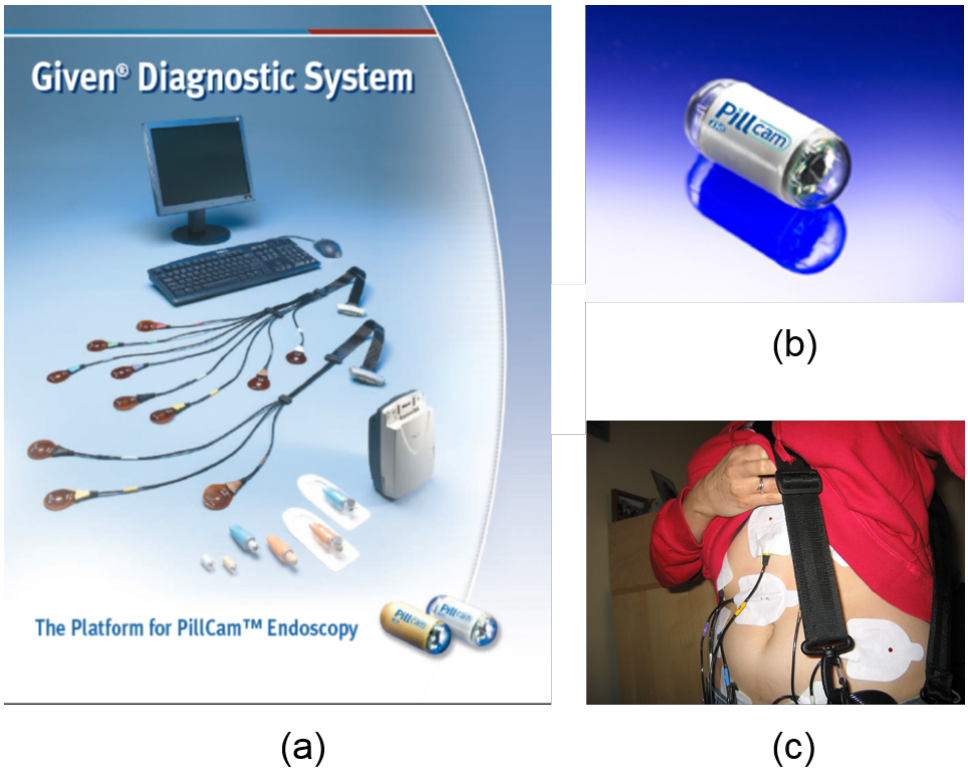

Figure I.1: (a) The Given Imaging Pillcam WCE commercial system. (b) The Given Imaging PillCam. (c) The weareable receiver weared by a patient.

while passing through the digestive system (CorTemp ®Core Body Temperature Monitoring System). The capsule wirelessly transmits data to a recorder worn by the patient and has been shown to be a reliable source for intestinal temperature measurement.

These clinically accepted technologies are less invasive than traditional flexible endoscopes, but are still subject to several limitations. The main limitations of this technology is that it has not successfully expanded to other anatomical districts, such as the stomach or the colon, where cancer strikes much more severely.Capsules are restricted to passive movement through the GI tract; (2) Capsule endoscopy systems lack position and orientation tracking systems that localize a capsule with respect to both body landmarks and a tridimensional world frame; (3) Effective drug delivery capsules for localized therapy have not yet been developed that enable the transition from research to clinical use; and (4) A unified model of capsule-gut interaction has not been developed.

I.2 MCR:State of the Art

Many diverse variants for MCR with sensors and/or actuators have been proposed in the literature, as reviewed in [8–10]. MCRs leverage extreme miniaturization to access

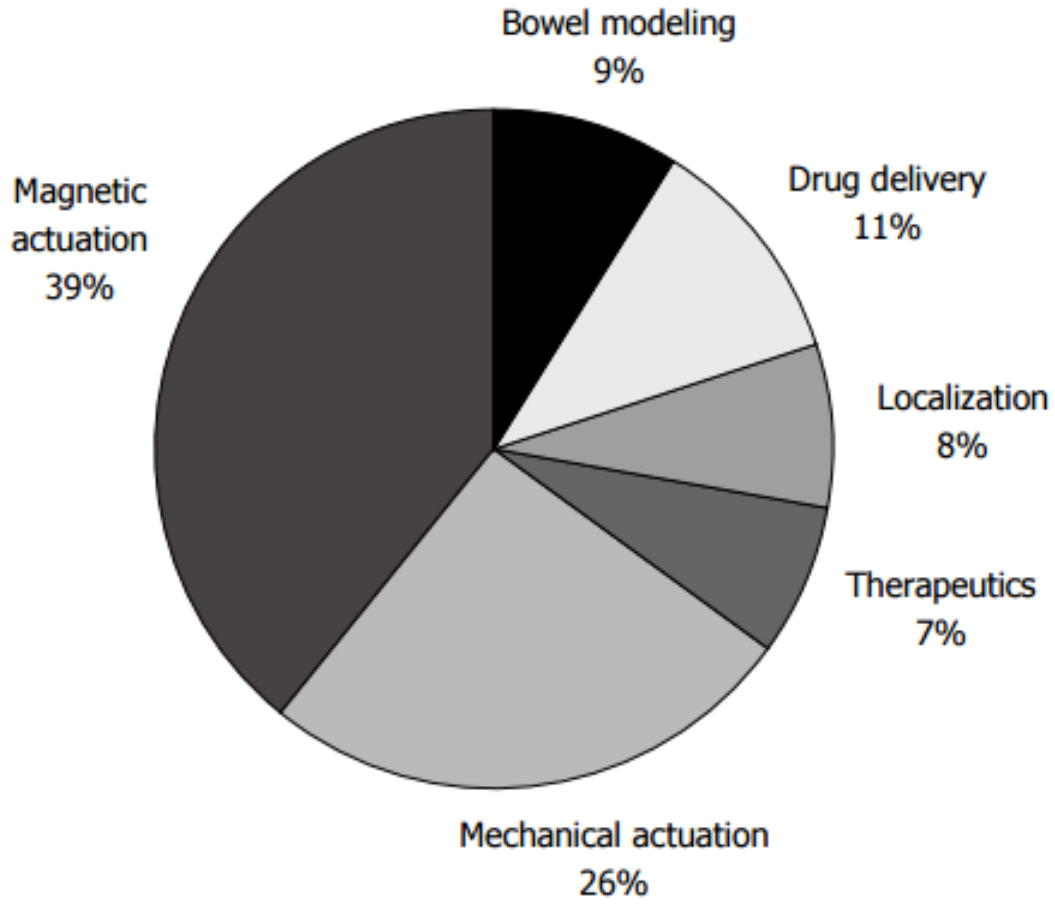

Figure I.2: Distribution of selected MCR as reported in [1].

and operate in environments that are out of reach for larger robots (i.e., typically 1 cm in diameter), and they are able to collect information and interact with the surrounding environment. As represented in Fig. I.2, MCR have been adopted to address different applications not available in WCE [11–15].

A selection of MCRs is represented in Fig. I.3: legs can propel a camera pill forward and backward inside the large intestine, while at the same time enlarging the lumen to provide adequate visualization. Valdastri and Webster developed a 12-leg capsule robot (Figure I.3.A), composed of 2 direct current (DC) brushless motors, magnetic encoders, a vision system, and a wireless microcontroller to crawl forward and backward inside the colon [16]. Use of magnets inside the capsule, acted upon by large externally generated magnetic fields, can also be used to controllably move a capsule as in [17, 18], where an industrial robot arm was used to hold and manipulate a large permanent magnet outside the patient. [18].

In this system, the capsule (Figure I.3.B) also contains magnetic field sensors and a 3D accelerometer to enable position and orientation detection via use of a computationally efficient magnetic field model. A wireless microcontroller embedded onboard acquires data from the sensors and sends it to the external unit, which computes the necessary external magnet motion to achieve the desired internal capsule motion. A hybrid MCRs that combine magnetic locomotion with either legs is shown in (Fig.I.3.C) [19]. Another way to enhance magnetic locomotion is to reduce capsule-tissue friction via mechanical vibration. In [20] the was proposed a capsule containing a wireless microcontroller, a vibratory DC brushed motor and a 3D accelerometer (FigureI.3.D). The stomach can be filled with water and provide a large open space ideal for inspection by a submarine-like capsule developed in [21]. This capsule, shown in Figure I.3.E, uses four independent propellers actuated by embedded DC brushed motors, and its speed and direction can be controlled with a joystick. In this case the signal coming from an embedded 3D accelerometer was used to balance the capsule thrust direction by controlling (via pulse width modulation) the rotational speed of each of the four motors. Swimming can also be accomplished via a flap-based mechanism, where flaps contain embedded small magnets interacting with a magnet spun by a single DC brushless motor onboard the capsule [22] (FigureI.3.F), thus generating a flapping motion and forward thrust. The first capsule that can carry out a surgical intervention was developed for controlled release of a surgical clip that can stop localized bleeding in the colon. The device (FigureI.3.G) uses embedded permanent magnets, enabling external locomotion via magnetic fields, and a pre-loaded clip, which can be fired by the action of a miniature integrated DC brushless motor, based on a wireless command [23]. Finally MCRs with enhanced visualization capabilities (i.e., panoramic vision and adjustable focus for the capsule in Fig.I.3.H and Fig.I.3.I, respectively).

Other MCR have been developed for MIS [24–26], as well for Natural Orifices Transluminal Endoscopic Surgery (NOTES) [27–30]. Overall, regardless their application, advances in the design and development of MCR require significant skills and effort in the prototyping, programming, debugging and miniaturizing of the device. The research groups are usually forced to create their own MCRs from the ground up. MCRs have severe/stringent power and space constraints, thus, forcing researchers to spend extra time and money on the difficult task of optimizing their hardware design, before beginning work on research. This amounts to a duplication of efforts by different research groups, which could be better applied to the innovation of MCR applications.

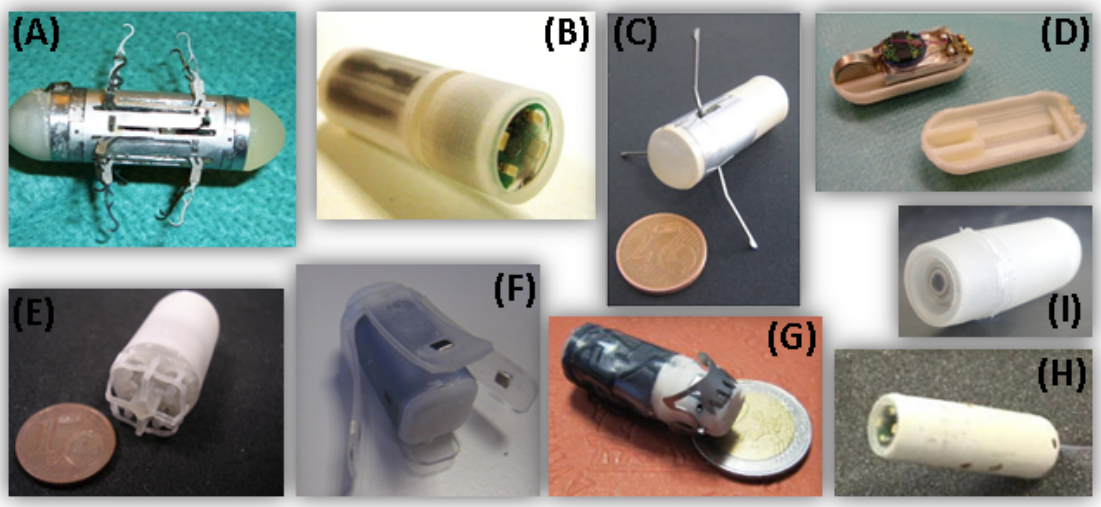

Figure I.3: Selection of MCR developed, diameter and length of each prototype are provided in mm in brackets: (A) 12-leg capsule (11 × 30). (B) Magnetic capsule (11 × 29). (C) Hybrid capsule (14 × 38) . (D) Vibration capsule (15 × 34). (E) 4-propeller swimming capsule (11 × 29). (F) Jellyfish-like swimming capsule (18 × 35). (G) Surgical clip releasing capsule (11 × 30). (H) Panoramic vision capsule (15 × 48). (I) Autofocus capsule (15 × 40).

I.3 Scientific Contribution

The scientific contribution of this work is to enable rapid prototyping of MCR through a modular architecture which can systematize their design process and make their development accessible to a wider community.

- We defined a modular architecture for the design of MCR. The architecture is schematically represented with the general modules in Fig. II.1. A central processing unit (CPU), can be programmed by the user to accomplish a specific task; a communication submodule, that links the device with user intent; a source of energy that powers the system; and sensors and actuators, both of which interact with the surrounding environment to accomplish one or more specific tasks. This architecture consists of ready-to-use modular hardware in the form of miniature boards featuring a microcontroller with radio, power management, sensor and actuation modules accompanied with a highly reconfigurable software stack.

- The vast majority of the MCR developed thus far, including the ones in I.3 and presented in section I.2, share the same crosscutting constraints such as (1) size—ideally, a capsule device should be small enough to swallow or to enter natural orifices

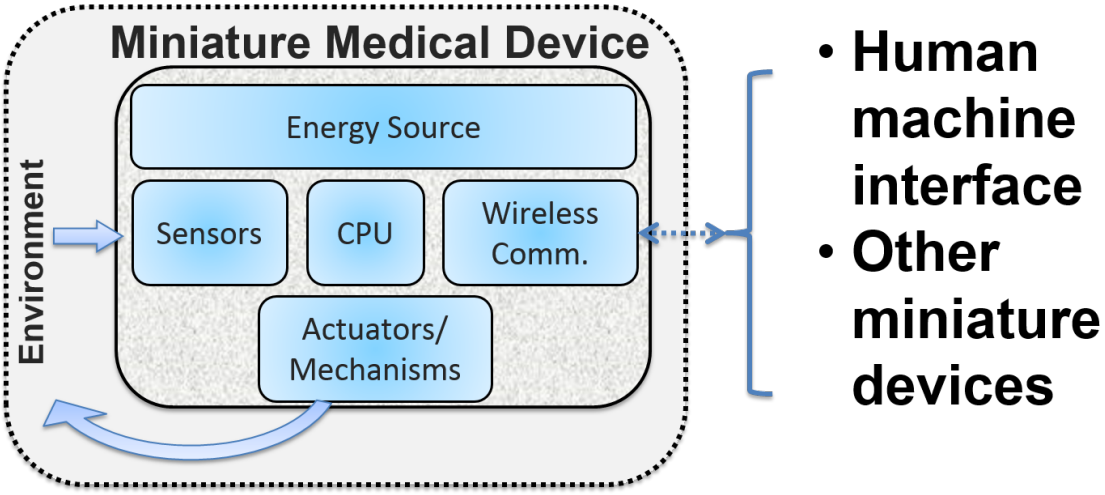

Figure I.4: Building modules of an MCR.

without requiring a dedicated incision; (2) power consumption—given the limited space available on board, energy is limited; (3) communication bandwidth—wireless signals must be transmitted through the human body with sufficient data rate; (4) fail-safe operation—since the device is deep inside the human body, medical personnel has no direct access to it; and (5) effective interaction with the target site according to the specific functions the device is required to fulfill. The modular architecture presented in this work has been abstracted from these constraints.

- The modular architecture presented in this war was successfully applied to the field of MCRs. In particular we developed different types of MCRs: a wireless palpation probe to restore the tactile feedback in MIS, an MCRs to study magnetic localization for WCE, an MCRs to measure the resistant properties in the GI tract, and a drug delivery MCRs.

I.4 Outline

This dissertation is organized as the following. Chapter II provides a detailed description of the modular architecture introducing its hardware and software components. Chapter III presents the most recent improvements of the architecture, these include new modules, a flexible backbone circuity for enhanced connectivity, and the integration of the modules with a component based Operating System (OS). Chapter IV describes in details how the proposed architecture was adopted to design a wireless probe to restore the tactile feedback in MIS [31–34]. V, describes a MCRs for magnetic localization of MCRs [35], measurements of the resistant properties in the GI tract [36], and drug delivery [37]. In

addition the architecture was successfully used to implement the hardware and firmware of a sensorized cane for gait patterns recognition [38]. Finally Chapter VI presents conclusions and summary of findings.

Chapter II

A MODULAR ARCHITECTURE FOR RAPID PROTOTYPING OF MEDICAL CAPSULE ROBOTS

This chapter describes the modular architecture for rapid prototyping of MCRs. The architecture consists of both hardware modules and firmware libraries that can be used for developing MCRs. In particular, each of the hardware modules developed to date targets one of the five major subsystems of MCRs, i.e. computation, wireless communication, power management, sensing and actuation. A list of the developed hardware modules and their capabilities is provided in this chapter with their main functionalities. The modules are small in size, low power, and have reconfigurable software libraries, which has been proven to work reliably for different types of MCRs. A design template for a generic MCR application implementing a robust communication protocol is presented in this chapter, together with its finite state machine abstraction, capturing all the architectural components involved. Finally the reliability of the wireless link is assessed for different levels of data transmission power and separation distances, as well as the current consumption for each module is quantified and the timing of the radio message transmission is characterized.

II.1 Architecture requirements

MCRs are tightly constrained in size and power consumption, and must be fail-safe and reliable in order to operate inside the human body. In addition, the modularity and re-usability of both the software and hardware components of MCRs would open this field to a wider community of researchers. In this section, we expand on these requirements and we lay the foundation for the proposed architecture.

Miniature Size

The diameter of a MCR is typically constrained by the entry point into the human body. In MIS [32], the MCR must fit the internal diameter of a surgical port, typically from 3 mm to 12 mm. For GI applications [19, 21, 39, 40], we can assume the diameter of commercially available WCEs, (i.e., 11 mm) as the benchmark [6]. Adopting these size constraints as a reference, all of the hardware modules presented in Section II.2 have been designed with a round-shaped Printed Circuit Board (PCB) having a maximum external diameter of 9.8 mm. modules can be stacked to achieve a cylindrical capsule-like shape.

Data Connectivity

To reach deep inside the human body, MCRs may be either wireless or softly tethered, depending on the specific application and/or the target anatomical district. In case of MIS,

NOTES or GI endoscopy in districts that are close to a natural orifice (e.g., the colon, oesophagus or stomach), a soft tether can be used to power the MCR and to easily retrieve the device at the end of the procedure. While in principle wired connectivity can be used to transmit data as well, increasing the number of wires in the tether may reduce its overall flexibility, thus affecting the mobility of the MCR [30]. Therefore, wireless data connectivity may still be a valid option for rapid the prototyping of soft-tethered MCRs, as discussed in [28].

Power Consumption in Case of Wireless Operation

Progress in battery energy density thus far has been slow compared with the pace of miniaturization in electronics. For this reason, batteries are typically the largest component of a wireless MCR [20, 21, 32]. Increasing battery capacity is typically required to achieve a longer operational time, but is rather expensive in terms of the space occupied on board the MCR. Moreover, in a modular system in which different kinds of sensors and actuators are embedded, and multiple tasks are performed, power consumption is not easily predictable *a priori*. For this reason, it is common practice to use low power Integrated Circuits (ICs) to limit the MCR's power consumption [41]. In addition, switches or General Purpose Input/Output (GPIO) pins should be used to power down sub-modules whenever their contribution is not required. Similarly, the firmware development must include techniques to reduce power consumption, such as selecting the lowest transmission power that still allows for wireless connection or reducing the data sampling rate to the minimum required by the specific application.

Safety and Reliability

In order to move towards clinical trials, a MCR must comply with regulatory requirements (e.g., U.S. Food and Drug Administration (FDA) 510(k) or Investigational Device Exemption (IDE), European CE Approval Process for Medical Devices). The adoption of standardized hardware and software modules that are compliant with regulatory requirements would facilitate and speed up the clinical translation of innovative MCRs. The authors designed the modules based on FDA guidelines [42], and are maintaining the appropriate documentation related to the design process. This documentation can be made available upon request for MCR designers interested in clinical trials. The authors are also closely watching the evolution occurring in the field of international standards for the interoperability of wireless medical devices [43]. However, at the time of writing, no international standard is specifically addressing wireless communication from a device inside the human body to a collector point outside the patient.

In terms of safety of operation, one main constraint for intra-body devices is the operating temperature. Developed hardware modules should not increase a patient's body temperature by more than 1°C, as reported in [44]. This requisite has been taken into account when testing modules, as reported in Section II.2. The requirement in temperature variation is also related to the electromagnetic energy density of the RF waves carrying the telemetric signal. According to [44], the reference level for general public exposure to time-varying electric and magnetic fields is 10 W/m^2 for a signal frequency of 2.4 GHz, which is used by the modules. Staying below this level would ensure that the body temperature increase due to wireless communication remains below 1°C. This requisite has also been considered during testing.

Concerning reliability, MCRs are beyond reach once they have been deployed in the human body. Therefore, fail-safe operation becomes a required feature. All hardware and supporting software must be extensively tested to prevent unexpected behaviours or failures, while the firmware must include mechanisms to guarantee robustness during the device's operation (e.g., communication error checking, watchdog timers). A main contribution in terms of robustness may come from the open source community [45,46]. Once the platform starts to be adopted by researchers, the user community will identify bugs and sources of error that the authors did not envisage at the time of writing, such as preventing a malicious attack against it, as in [47].

Modularity

The architecture of a MCR consists of the following general hardware modules: (1) a CPU that can be programmed by the user to accomplish a specific task; (2) a communication sub-module that links the device with user intent; (3) a source of energy that powers the system; (4) sensors and (5) actuators, both of which interact with the surrounding environment to accomplish one or more specific tasks [8,48]. While sensors and actuators are specific to the application, CPU, wireless connectivity and power management modules can be designed to fit a number of different scenarios. Following this approach, specific actuation and sensing modules can be connected with the generic modules to achieve the desired MCR functionalities. This allows the user to focus on interfacing the modules rather than designing them. When developers need functionalities that cannot be accomplished with the available modules, novel components can be developed and interfaced with existing blocs. This alleviates the burden of having to design each individual module of a MCR, and shortens the time-to-prototype for novel MCRs.

The main downside of a modular approach, however, is that a system made of modules is not optimized for the particular application, and it usually requires more space compared

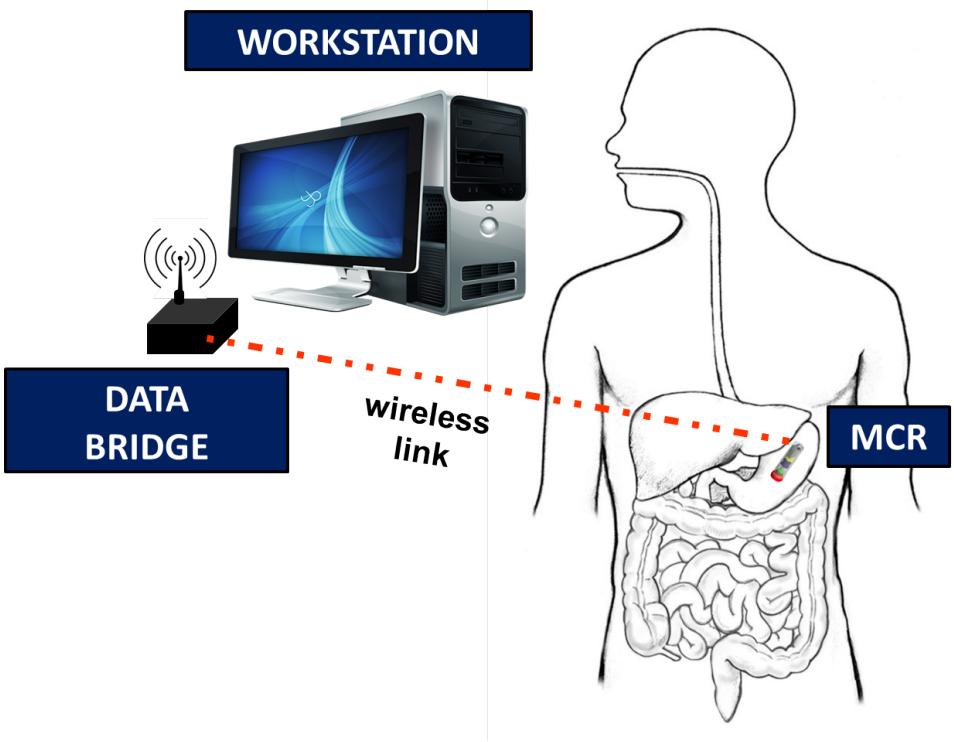

Figure II.1: A platform, including the MCR, the data bridge and the workstation.

to a custom device. The best course of action for MCR designers would therefore be to validate their hypotheses and preliminary designs using the platform, and then move to a custom approach as soon as they are satisfied with the results. Software modularity is also pursued within the platform by providing the users with interface layers to the hardware modules.

Reconfigurability

Reconfigurability is the ability of a modular system to be rearranged, adding or removing either hardware or software components in order to adapt to variable requirements. Reconfigurable hardware plays an important role in designing MCRs, since most developers look for the best performance with a very limited power budget. Each miniature module is associated with a block of code (or a library) that can be included or removed from the main code at the time of design, along with the corresponding sensor or actuator module addition or removal.

II.2 Architecture overview

As represented in Figure II.1, a system based on this modular architecture consists of three separate subsystems: the MCR, the data bridge and the workstation. Each subsystem

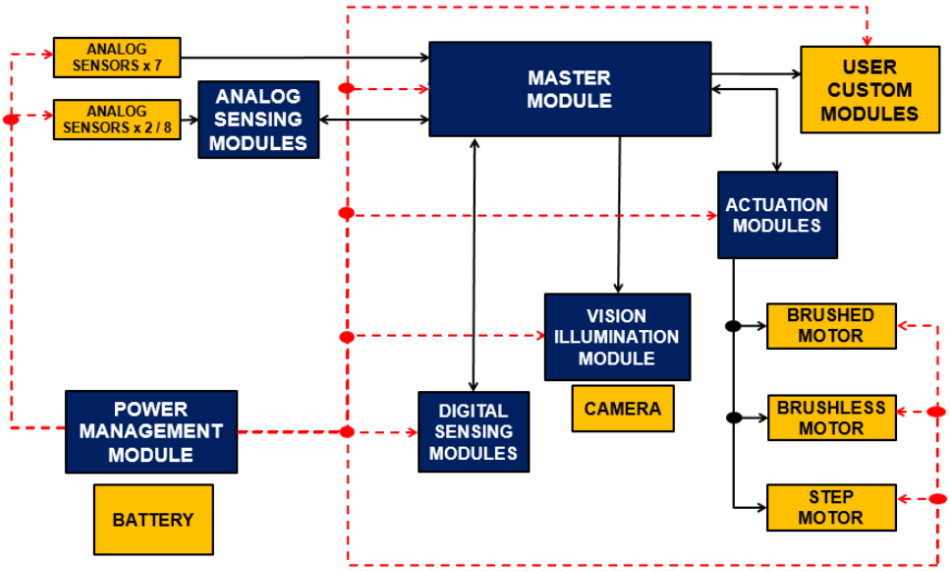

Figure II.2: The Modular Architecture. The modules in blue are described in this work and are provided open source, while the modules in orange should be added by the developer.

is made of different hardware components and is programmed with dedicated firmware/-software.

Concerning the hardware, the MCR embeds miniature modules connected together by the developer to accomplish the desired task. Each miniature module provides a distinct functionality, such as wireless communication, powering, digital or analogue sensing, actuation, vision and illumination. These modules are presented in the Section II.2. Bidirectional data communication between the MCR and the workstation is handled by the data bridge, described in Section II.2. Finally, the workstation consists of a Personal Computer (PC), where the user interface is implemented.

Hardware Overview

In this section, we provide a description of the architecture hardware, covering the individual MCR modules in Sections II.2 to II.2, and the data bridge in Section II.2.

Miniature MCR Hardware

Referring to Figure II.2 and Table II.1, the 14 modules developed for architecture can be categorized according to six different types: master, digital sensing, analogue sensing,

Module Name	Type	Function	IC	⌀ [mm]	I_{ACTIVE} [mA]	I_{IDLE} [mA]
Master	Master	CPU and Wireless Communication	CC2530	9.8	36 (Max)	0.009
3DA	Digital Sensing	3D Accelerometer	LIS331DLH	9	0.25	0.01
3DG	Digital Sensing	3D Gyroscope	L3GD20	9	6.1	0.005
3DM	Digital Sensing	3D Magnetometer	LIS3MDL	9	0.27	0.001
3DAG	Digital Sensing	3D Accel. / Gyro.	LIS330DLC	9.8	6.11	0.005
3DAM	Digital Sensing	3D Accel./ Magnet.	LSM303D	9.8	0.3	0.001
3DAMG	Digital Sensing	3D Accel. / Magnet. / Gyro.	LSM9DS0	9.8	6.15	0.005
PT	Digital Sensing	Pressure/Temperature	MPL115A1	9.8	0.005	0.001
8ADC	Analogue Sensing	8 Channels ADC	AD7689	9.8	3.78	0.005
2AF&ADC	Analogue Sensing	2 Channels Front End & ADC	AD623 & ADS8320	9.8	2.57	0.001
BSDCC	Actuation	Brushed DC Controller	A3901	9.5	4.8	0.005
BSLDCC	Actuation	Brushless DC Controller	BH67172NUX	9.8	4.5	0.009
VI	Vision/Illumination	Vision/Illumination	NUD533	9.8	30	1.1
PMM	Power Management	Power/Battery Monitoring	TPS33	9.8	0.18	-

Table II.1: Main features of the modules.

actuation, power management and vision/illumination. For each specific module, Table II.1 reports the name, the type, the function, the core IC, the diameter and the current consumption for both active and idle modes (i.e., I_{ACTIVE} and I_{IDLE}, respectively), derived as described in Section II.2. The maximum module thickness is 1.54 mm. Solderable pads are available on each module for wired connectivity, while the schematics and PCB layouts are provided in the open source repository. It is worth mentioning that user-defined modules can be connected to the master module via one of the communication or data acquisition peripherals, or by using the available GPIO pins. If the developer wishes to replace the master module with a different microprocessor, the other modules can still be integrated in the MCR, as they are provided with standard connectivity.

Master Module

The master module is the programmable component of a based MCR and is also responsible for wireless communication with the data bridge. As represented in Figure II.2, other functionalities include data acquisition (directly from a sensor or through a dedicated front end), the generation of control signals for the actuators, and the management of active/idle mode for the other modules. The core IC in the master module is an 8051-based wireless microcontroller (CC2530, Texas Instruments, USA) [49]. It features an 802.15.4 radio transceiver, 8 kB of Random Access Memory (RAM), 256 kB of flash, GPIO pins, Serial Peripheral Interface (SPI), an eight-channel Analogue-to-Digital Converter (ADC) with a 12-bit resolution, energy management, sensor data processing and Pulse Width Modulation (PWM) generation for actuator driving. The board layout of the master module was designed with 19 solderable GPIOs pads for interfacing with the other hardware components.

Concerning wireless connectivity, the CC2530 IC package comes with two unbalanced output pins that need to match a 50 Ω impedance with a single termination. This matching

is typically obtained by passive discrete RF front-ends, consisting of dedicated high-precision capacitors and inductors. However, this is not an optimized solution in terms of the component count and PCB surface required. Therefore, a matching impedance balun low-pass filter was selected (2450BM15A0002, Johanson Technology, USA) for the master module. The routing from the unbalanced RF pins is symmetrical to the balun, with tracks of the same length and width, thus reducing RF absorptions by working in combination with a ground-shielded plane underneath. Concerning the antenna, it consists of a quarter-wave monopole, obtained by a copper wire soldered nearby the balun on a specially designed pad.

Selecting this specific IC as the core of the Master Module has a double advantage in terms of size. First, a single module can fulfil both wireless communication and data management functions. Second, the antenna for a 2.4 GHz communication is typically smaller than what would be required if using a lower carrier frequency. On the other hand, 2.4 GHz is very close to the resonance frequency of water molecules and, thus, it is not an optimal solution for devices working inside the human body due to tissue attenuation of the electromagnetic signal. While our previous work shows that the solution proposed here is suitable for feasibility studies and *in vivo* trials in porcine models [50], the optimal solution when transitioning to design optimization is a carrier frequency in the 433 MHz band [51].

Power Management Module

The PMM provides regulated power from the battery to the rest of the modules. The PMM (architecture is represented in Figure II.3 (a)) allows the developer to use different powering solutions. In particular, this module integrates a Low Drop Output (LDO) to generate a single supply-fixed 3.3 V voltage, providing up to 500 mA of current. The PMM also generates a variable regulated output voltage within the range of 0 V to 3.3 V, and two equal fixed dual-supply $\pm 1.65\ V$ voltages. This module features circuit protection to prevent an incorrect battery connection and Electrostatic Discharge (ESD). The core ICs for this module are a LDO (TPS33, Texas Instruments, USA) and a dual operational amplifier (AD8617, Analog Devices, USA). The PMM also implements a battery monitor by partitioning the battery voltage. This signal can then be connected to an ADC input pin of the master module.

Digital Sensing Modules

As reported in Table II.1, we have implemented seven different sensor modules with a digital interface to the master module. The master module can configure the sensor and retrieve the data via SPI communication. To save power whenever the application allows, the master module can control the active/idle mode of the sensor via GPIOs connections. The available digital sensing modules at the time of writing – with their identifier in brackets –

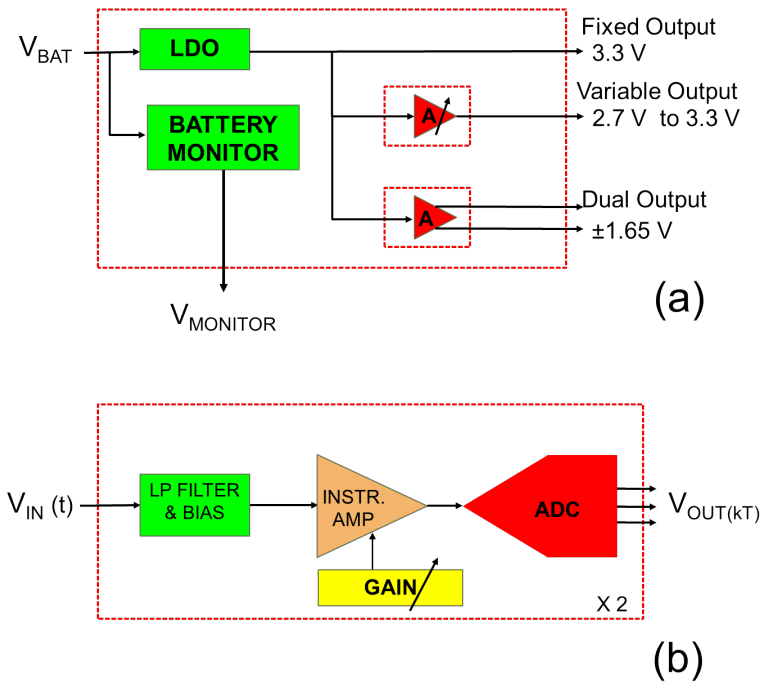

Figure II.3: The architecture of the PMM module (a) and the 2AF&ADC module (b), respectively.

include a triaxial accelerometer (3DA), a triaxial gyroscope (3DG), a triaxial magnetometer (3DM), a triaxial accelerometer combined with a triaxial gyroscope (3DAG), a triaxial accelerometer combined with a triaxial magnetometer (3DAG), a full nine-Degrees of Freedom (DOF) Inertial Measurement Unit (IMU) (3DAMG), and a pressure and temperature (PT) sensor. Core ICs, board diameters and current consumptions are provided in Table II.1. The sensor configuration and data collections are handled by the interface library described in Section II.2. If the developer needs to use a different digital module, it can be connected directly to the SPI port of the master module.

Analogue Sensing Modules

Whenever a 12-bit resolution is acceptable for the specific application, analogue sensors can be connected directly to the ADC embedded in the master module, as suggested in Figure II.2. If a higher resolution is required, the eight ADC module can be integrated in the MCR. This module embeds an ADC (AD7689, Analog Devices, USA) with eight single-ended channels (or four differential), a resolution of 16 bits per channel and a 250 kHz sampling rate.

Another available module – the 2AF&ADC – includes a two-channel analogue front end for conditioning the sensor signals before digitalization. This module features hardware bias correction, double-ended or single-ended sensor interface, gain selection, and single or dual supply operation (±1.65 V). The block diagram for this module is represented in Figure II.3 (b) and consists of low-pass filters and gain selectors for the instrumentation amplifier (AD623, Analog Devices, USA) and a 16-bit resolution ADC (ADS8320, Texas Instruments, USA) [49].

Both analogue sensing modules described in this Section exchange data with the master module via the SPI interface.

Actuation Modules

Two different modules are currently available for driving miniature actuators by reading PWM signals from the master module.

A first board (BSDCC) was designed to drive up to four brushed Direct Current (DC) motors, or four vibrating mass motors, or two step motors. This module integrates a dual full-bridge low-voltage motor driver (A3901, Allegro Microsystems, USA).

A second module – the BSLDCC – is capable of driving up to two brushless motors via two identical ICs (BH67172NUX, ROHM Semiconductor, Japan). This board is also able to read the rotor relative position through Back Electromotive Force (BEMF) feedback, and change the direction of rotation depending on the status of a digital input pin connected to the GPIO port of the master module.

Vision and Illumination Module

MCR applications may include the use of a vision module [26, 28, 52]. Since the master module only provides low data-rate wireless connectivity, a dedicated telemetry channel is required for image transmission. A number of miniature wireless cameras that integrate telemetry are available off-the-shelf, including the CMDX-15, CMDX-23, CMDX-6, CMDX-58 (RF LINKS, USA) [53], and can be integrated within the platform. Miniature wired camera can be used [54] for prototyping or soft-tethered applications.

Regarding illumination, which is always required for acquiring endoscopic images, we have developed a dedicated module (VI) consisting of a Light Emission Diode (LED) driver (TPS61161, Texas Instruments, USA) and four white LEDs connected in series. LED brightness is controlled by the master module via a PWM signal. The driving current can reach up to 120 mA. This module also includes a digital switch (MIC94044, Microrel, USA) to power the wireless camera. The switch can be connected to a GPIO on the master module. As represented in Figure II.4, the VI board comes with an off-centred circular opening (diameter of 4 mm) to accommodate the optics of the camera. Should a

larger opening be required, the number of LEDs can be reduced. Extreme care is required in integrating the camera, the illumination and the optics (i.e., in order to avoid image degradation due to reflection and back scattering, the camera needs to be optically isolated from the LEDs).

The Data Bridge

The current version of the data bridge consists of the same wireless microcontroller used in the master module (CC2530, Texas Instruments, USA), a Universal Serial Bus (USB)-to-Universal Asynchronous Receiver/Transmitter (UART) converter (FT232R, Future Logic Devices, UK), and 19 GPIOs available to developers for connecting external peripherals. As represented at the top of Figure II.4, the data bridge is a 25 mm $\times$ 30 mm $\times$ 1.54 mm PCB board that can be powered over the USB connection with the workstation.

Regarding the RF connectivity, the data bridge implements the same circuitry as the master module (i.e., the balun and the quarter-wave monopole antenna). Experimental data reported in Section II.2 shows a reliable connection within 2 m of separation distance during *in vivo* trials. If the wireless link needs to cover a larger range, a power amplifier (e.g., CC2590, Texas Instruments, USA) must be integrated in the data bridge.

The Firmware Stack

As represented in Figure II.5, the firmware stack consists of three layers of libraries that build on top of the physical layer. The interface layer and the modules layer together constitute the Hardware Abstraction Layer (HAL). The application layer is where developers implement the main routine that defines and instantiates the tasks for the modules.

The firmware stack is written in the *ANSI C* programming language and can be compiled by any standard C compiler, such as Code Composer (Texas Instruments, USA), IAR Embedded Workbench (IAR Systems, USA) or Eclipse (Eclipse Foundation, CAN) [49, 55, 56].

The Interface Layer

This layer provides functionalities for the developer to interface the MCR master module, either to the data bridge via radio communication, or to the other hardware modules via SPI, PWM, ADC, GPIOs or UART peripherals. In particular, the SPI interface can be used to configure and receive data from the digital sensing modules or to gather data from the ADC channels in the analogue sensing modules. Actuation can be controlled via the PWM interface or by the GPIOs pins used as ON/OFF switches. Another possible function for the PWM interface is to regulate LED brightness in the illumination module.

As the MCRs are battery operated, the interface layer gives the developer several macros to handle the master module power modes and the battery monitor in the PMM module.

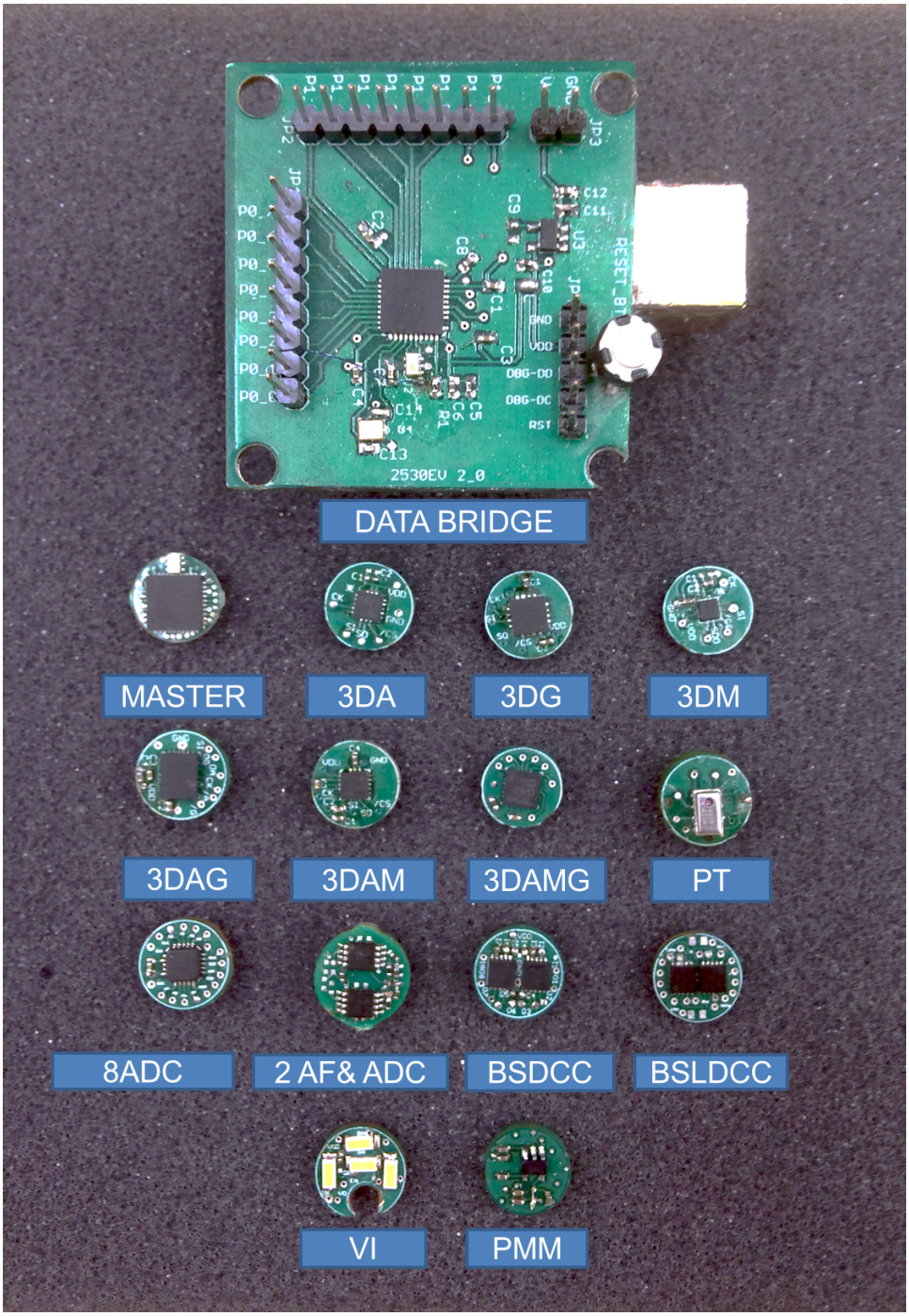

Figure II.4: The platform hardware modules.

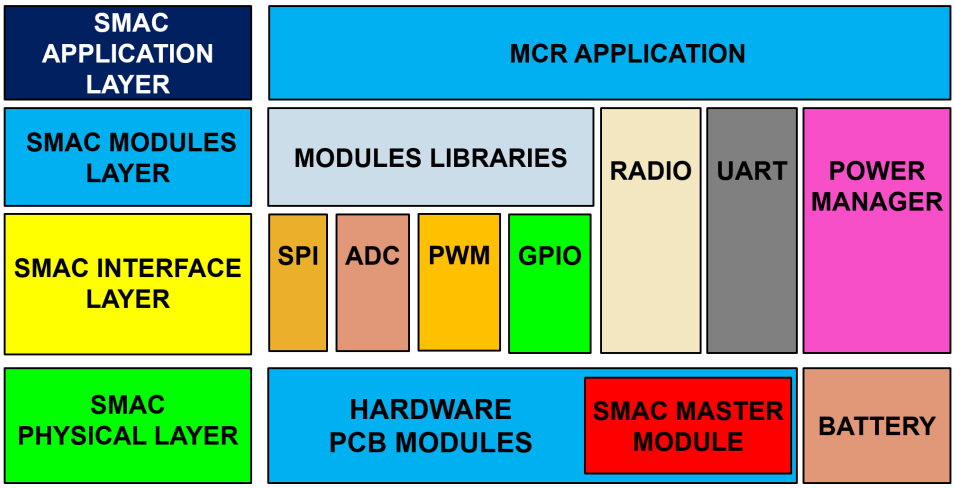

Figure II.5: The firmware stack.

Regarding wireless communication, a dedicated radio library provides macros to configure the 2.4 GHz RF wireless link and set connection parameters, such as security key, RF channel, frequency tuning and device addresses. The radio interface is capable of transferring data within a defined time-out, varying the RF power to save battery lifetime, and measuring the RSSI. The radio message, represented in Figure II.6, has the IEEE 802.15.4 Physical Layer (PHY)/Medium Access Control (MAC) standard frame [57], with a formatted payload that includes a message header, a package counter, the battery level, a time stamp, the master module core IC temperature, RSSI, the data length, a variable-size data slot, and a message-end code. The maximum data payload is 108 bytes per message. Typically, the payload contains messages and sensor data in case of communication from the MCR, or messages and commands when travelling in the opposite direction (i.e., from the data bridge to the MCR).

As proposed in the example illustrated in Section II.2, the payload can be used as a shared package across platform subsystems to allow state synchronization. This can be achieved by using a common message syntax, data types, encoding rules and nomenclature. This approach also allows the application to detect the status of data transmission, to check reception errors and to assess data corruption. These features are very useful in notifying the workstation of any possible failure in the MCR.

When the developer is programming the microcontroller in the data bridge, the interface layer provides UART communication with the workstation, as well as radio communication with the MCR and control over the GPIO pins.

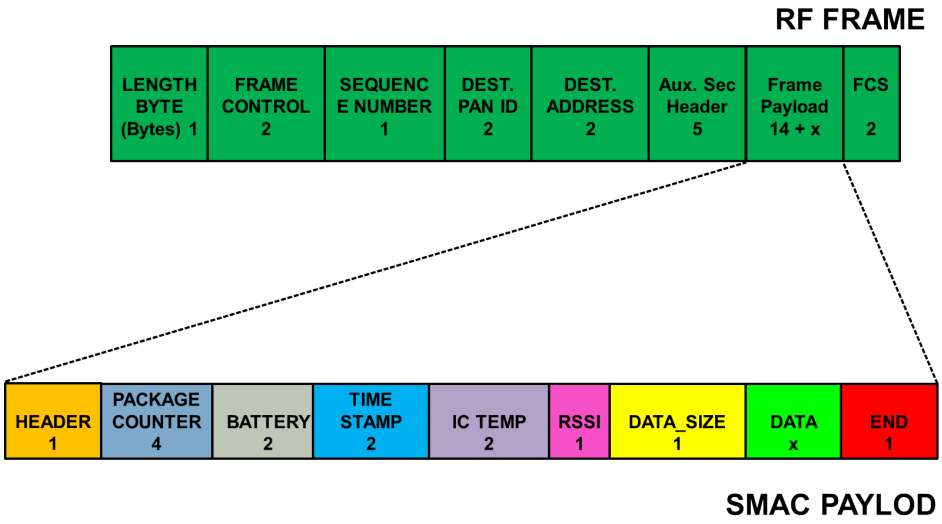

Figure II.6: The radio message and the RF frame descriptor.

The Modules Layer

This layer provides libraries for each specific hardware module. These libraries are linked in the application through a configuration file, which defines the MCR configuration. Each library consists of primitives for the interface layer to access the internal functionalities of the specific module. These macros can be used to read/write the module registers, access the module GPIOs or operate the core IC. For example, if we consider an MCR integrating an analogue sensor, a digital sensing module (e.g., 3DG), an analogue sensing module (e.g., 2AF&ADC), and an actuation module to control a DC brushless motor (e.g., BSLDCC), the developer must define the configuration file to include the corresponding embedded module libraries, as reported in the C-code example shown in Listing II.1.

Listing II.1: A configuration file example

```
/* CONFIGURATION FILE EXAMPLE */
#include "interface.h"
/* Includes modules interfaces stacks*/
#ifndef CONFIG_H_
#define CONFIG_H_
// Modules Inclusion
// Defines all the SMAC modules
// If a module is defined as TRUE
// its library will be compiled
```

```
#define 3DA  0
#define 3DG  1
#define 2AFEADC 1
...
...
...
#define BSLDCC 1
// process the libraries inclusions
// based on what defined
#ifdef 3DA
#include "3DA.h"
#endif
#ifdef 3DG
#include "3DG.h"
#endif
#ifdef 2AFEADC
#include "2AFEADC.h"
#endif
...
...
...
#ifdef BSLDCC
#include "BSLDCC.h"
#endif
#endif
```

This layer allows the developer to easily reconfigure the MCR in case a hardware module needs to be added, removed or replaced by a different one. Any library describing user custom modules can be straightforwardly integrated in the modules layer.

The Application Layer

The application layer consists of a main routine where the developer implements the MCR application. Inbound commands for the HAL are included here through the macros defined in the configuration file. These commands include sampling, actuation and data transfer through the radio interface to the data bridge. The developer can incorporate into the application layer custom algorithms to accomplish the desired MCR tasks.

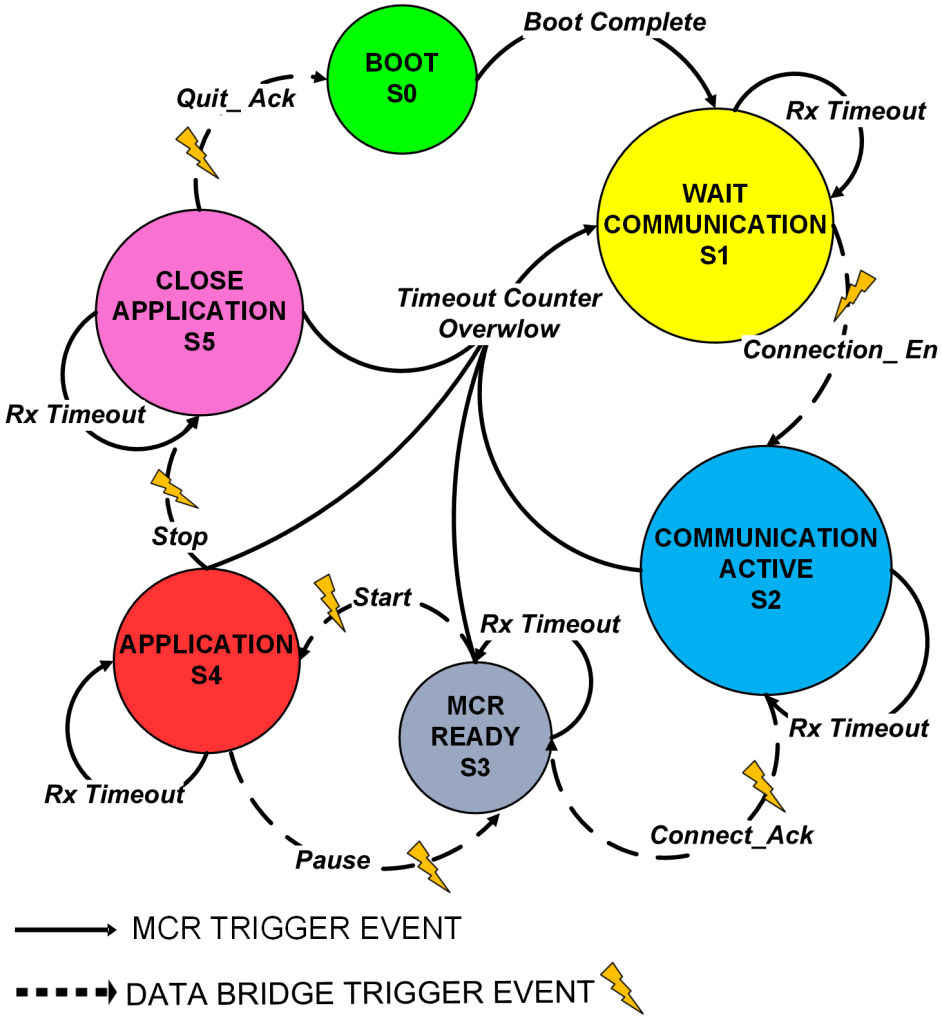

Figure II.7: FSM diagram for the MCR.

An Application Example

The application example provided in this section describes a robust handshaking protocol for wireless communication between the MCR and the user interface running on the workstation. This protocol was successfully implemented in [31, 32, 36].

The application used in this example includes two different firmware codes – one for the MCR and one for the data bridge – that can be represented as two separate FSM diagrams. The FSMs implemented in the MCR and in the data bridge are shown in Figure II.7 and Figure II.8, respectively, while the FSMs interaction with the workstation is presented in the time-flow diagram in Figure II.9. Each of the FSMs consist of six numbered states (i.e., $S0$ to $S5$). State transition from a certain state to another for both the FSMs are

caused by *triggering events*, such as condition changes, timer expiration, firmware failures or workstation commands from user input devices (e.g., a keyboard, a joy-pad or a mouse).

The three subsystems, after powering up, are in a *BOOT* state to configure themselves upon the configuration file settings. For example, the MCR configures the communication interface parameters (i.e., RF and SPI), as well as the embedded hardware modules. When the *BOOT* completes, the subsystems change their own state according to their FSMs. The MCR switches into the *WAIT COMMUNICATION* state, the data bridge into the *WAIT WORKSTATION ACTIVE* state, and the workstation into the *WAIT USER COMMAND* state. These are passive states in which packages are broadcast from the MCR to the rest of the platform, regardless of an established connection, and the workstation can access the shared payload fields, such as the battery level or the RSSI, or send notification to the user that the MCR has successfully booted up.

In the *WAIT COMMUNICATION* state, the MCR periodically switches between Low Power Mode (LPM) (*i.e., SLEEP* and *IDLE*) and attempts to establish the communication with the data bridge. When the MCR is *IDLE*, it executes sequentially the following tasks: radio activation, *Connection_En* message transmission, and reception of the data bridge acknowledgement, the *Connect_En*. This acknowledgement is accepted only when it arrives within a predefined time frame (typically in the order of a few ms), otherwise a time out event will occur, forcing the MCR back to the *SLEEP* LPM. This sequence repeats until the communication with the data bridge is established through the *Connect_En* command, triggered from user input devices. On this event, the workstation and the data bridge change their states respectively to *WORKSTATION ACTIVE* and *BRIDGE ACTIVE*, and subsequently, the MCR switches to *COMMUNICATION ACTIVE*. In the *COMMUNICATION ACTIVE* state, the MCR has to notify whether the communication was established with all the subsystems (e.g., itself and the workstation). Thus, it replies to the data bridge with the *Connect_Ack* message and changes its state to *MCR READY*, waiting for the *Ready* radio acknowledgement. To guarantee robust handshaking messaging, both the FSMs implement the reception of acknowledgements within firmware time outs. Every time a time out event occurs, no frame is detected and a time out counter is increased. The MCR retries the previous message transmission until the next acknowledge is received, or a *Time out Overflow Event* occurs, which triggers back the MCR to the *WAIT COMMUNICATION* state. The same mechanism is implemented by the data bridge which, after receiving the *Connect_Ack*, changes its state into *BRIDGE READY*, waiting for the *Ready* workstation message as shown in Figure II.9. Any error in the communication to or from both the MCR

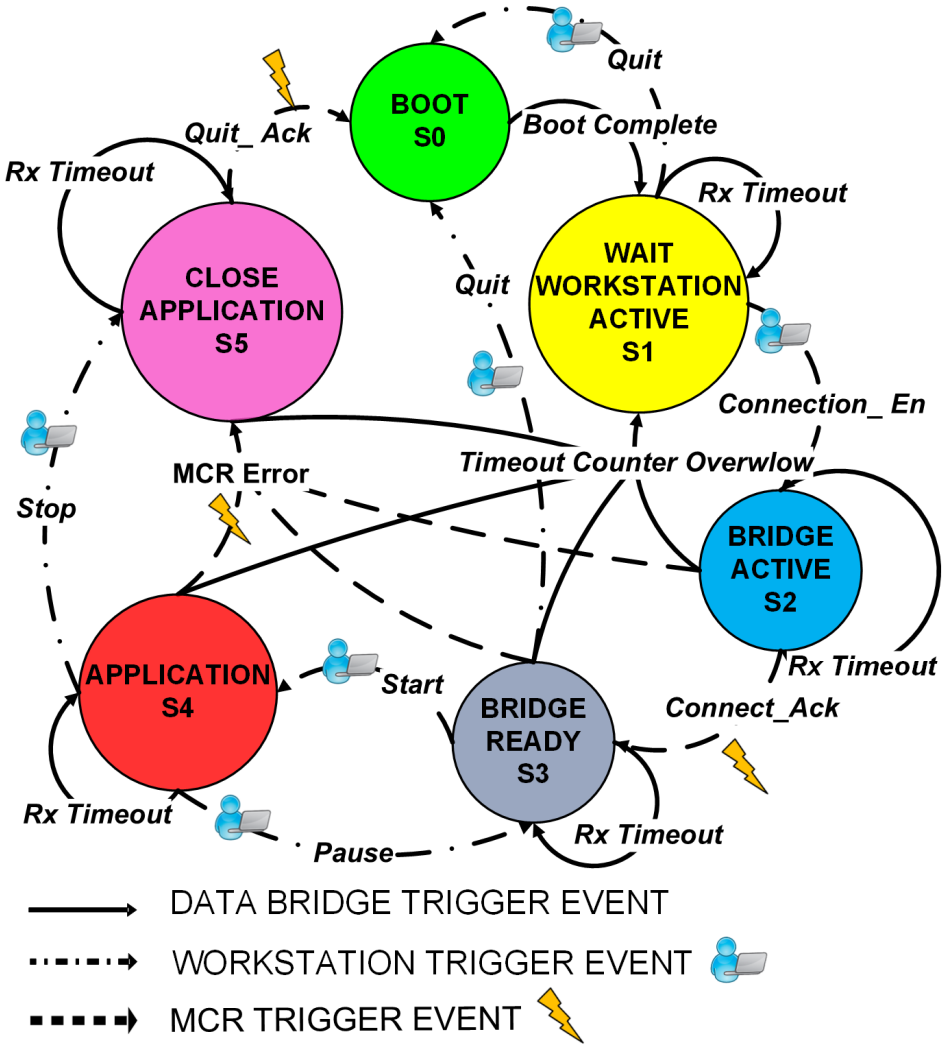

Figure II.8: FSM diagram for the data bridge.

and the data bridge forces their states to *WAIT COMMUNICATION*, while the workstation is notified by error messaging. Once the *Ready* and *Ready_Ack* messages are received by all the subsystems, the entire platform waits in the *READY* state for user input device commands, such as *Start*, *Pause*, and *Stop*.

The user command *Start* executes the main application, and the command *Pause* stops its execution and forces each subsystem back to $S3$, the *READY* state. In the *APPLICATION* state, the battery charge level and the RSSI are checked constantly in addition to the RF time out. This improves the robustness and the reliability of the platform by notifying the user if packages get lost, if the battery level is low, or if the RF signal strength is weak. The data flow in the *APPLICATION* state is bidirectional and the workstation can control

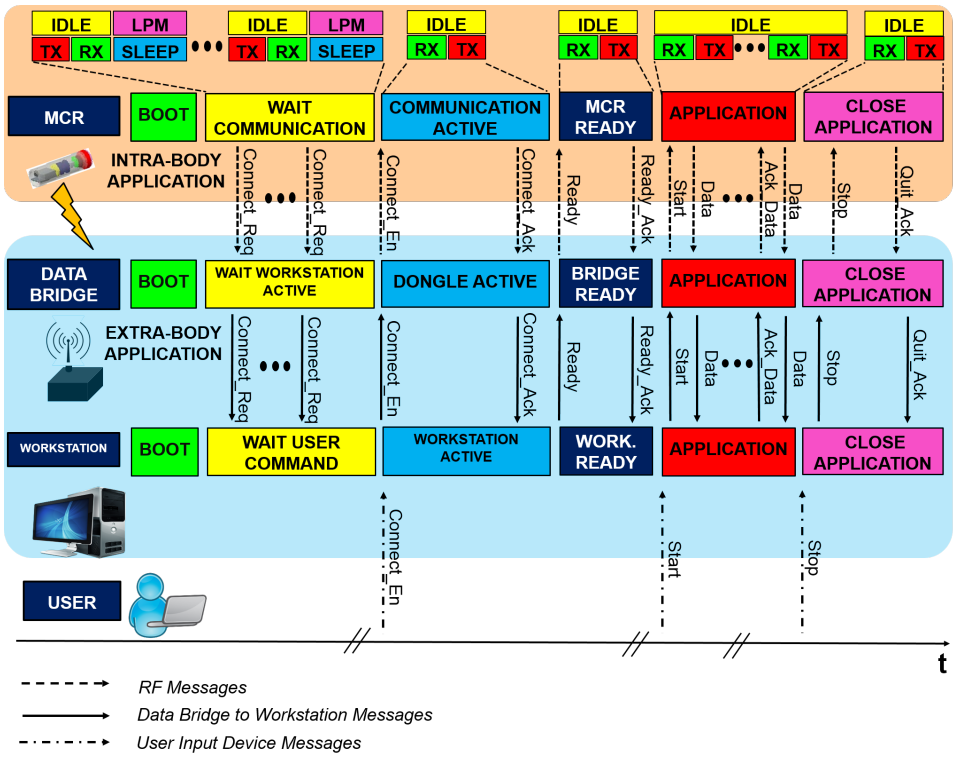

Figure II.9: Time flow diagram representing the handshaking protocol among the MCR, the data bridge and the workstation.

the MCR by sending commands for actuators or data for embedded algorithms. Finally, the *Stop* command forces the subsystems to $S5$, the *CLOSE APPLICATION* state, in which the communications are closed. Here, each subsystem 'falls back' to the *BOOT* state after the *Quit_Ack* message.

EXPERIMENTAL RESULTS

We conducted experimental trials aimed to test the reliability and the quality of the wireless connection between the MCR and the data bridge. We also measured the transmission power, P_{TX}, required to establish a connection at different separation distances. We experimentally quantified the current consumption for each module and we characterized the timing of a radio message transmission. The MCR's temperature was monitored during an *in vivo* trial on a porcine model to confirm that the temperature increase was below 1°C.

***In Vitro* Trial**

The MCR used for this trial consisted of a master module, a PMM, a PT module and a 50 mAh battery (LP50, Plantraco, CAN). All the modules were enclosed in a rapid

prototyped (Objet 30, Objet Geometries Ltd., USA) cylindrical shell (30 mm length, 11 mm diameter). The MCR was submerged in the centre of a 25 cm diameter glass tank, filled with 1.5 l of saline solution to emulate tissue absorption of RF [58]. Weight was added into the shell to achieve neutral buoyancy for the MCR.

The main application for the MCR attempted to establish communication at 14 different levels of P_{TX}, ranging from -18 dBm to 4.5 dBm, and to send pressure and temperature data acquired from the PT module. The data bridge was programmed with P_{TX} at 4.5 dBm. If the MCR received an acknowledgement from the data bridge within a time out period of 5 ms, a confirmation message was broadcast back to the workstation to notify that wireless communication was established successfully for the P_{TX} level used. The sleep time in between consecutive communications was set to 94 ms. The experiment consisted of 100 attempts for each of the 14 transmission power levels, for a total of 1,400 attempts. This test was repeated with the MCR at five different distances from the data bridge (i.e., 0 m, 0.3 m, 0.6 m, 1 m and 2 m).

For P_{TX} below -4 dBm, the connection probability – defined as the number of successful connections over the 100 attempts – was 95 % for a 0.3 m distance, but dropped below 10 % as the distance was increased. For larger P_{TX}, the experimental results are represented in Figure II.10 (a) for the connection probability, and in Figure II.10 (b) for the RSSI of the message received by the data bridge.

In order to save power, the developer may want to reduce P_{TX} to the minimum value that still allows for a reliable connection at a certain separation distance. As a guideline, for applications in which the two RF units are within 0.5 m, data can be broadcast with P_{TX} at -4 dBm. If the distance increases up to 2 m, then P_{TX} should be within -3 dBm and 2.5 dBm in order to achieve a connection probability of at least 75 %.

The maximum value of the plane wave power density emitted by the MCR was measured in order to compare it with the safety regulations discussed in Section II.1. Measurements were obtained by a portable field strength meter (8053, PMM, Italy) located in closest proximity to the antenna. The transmission power P_{TX} was set to the maximum level (i.e., 4.5 dBm). The instrument probe was oriented along the maximum radiation direction of the antenna, measuring 0.01 W/m^2. This value is considerably lower than the reference levels for general public exposure to time-varying electric and magnetic fields provided in [44].

Power Consumption

In order to quantify the current consumption of each module for both active and idle modes, the voltage drop across a 10-Ω resistor placed in series to the positive voltage supply terminal was recorded with a digital oscilloscope (Tektronix, TDS12014C, USA).

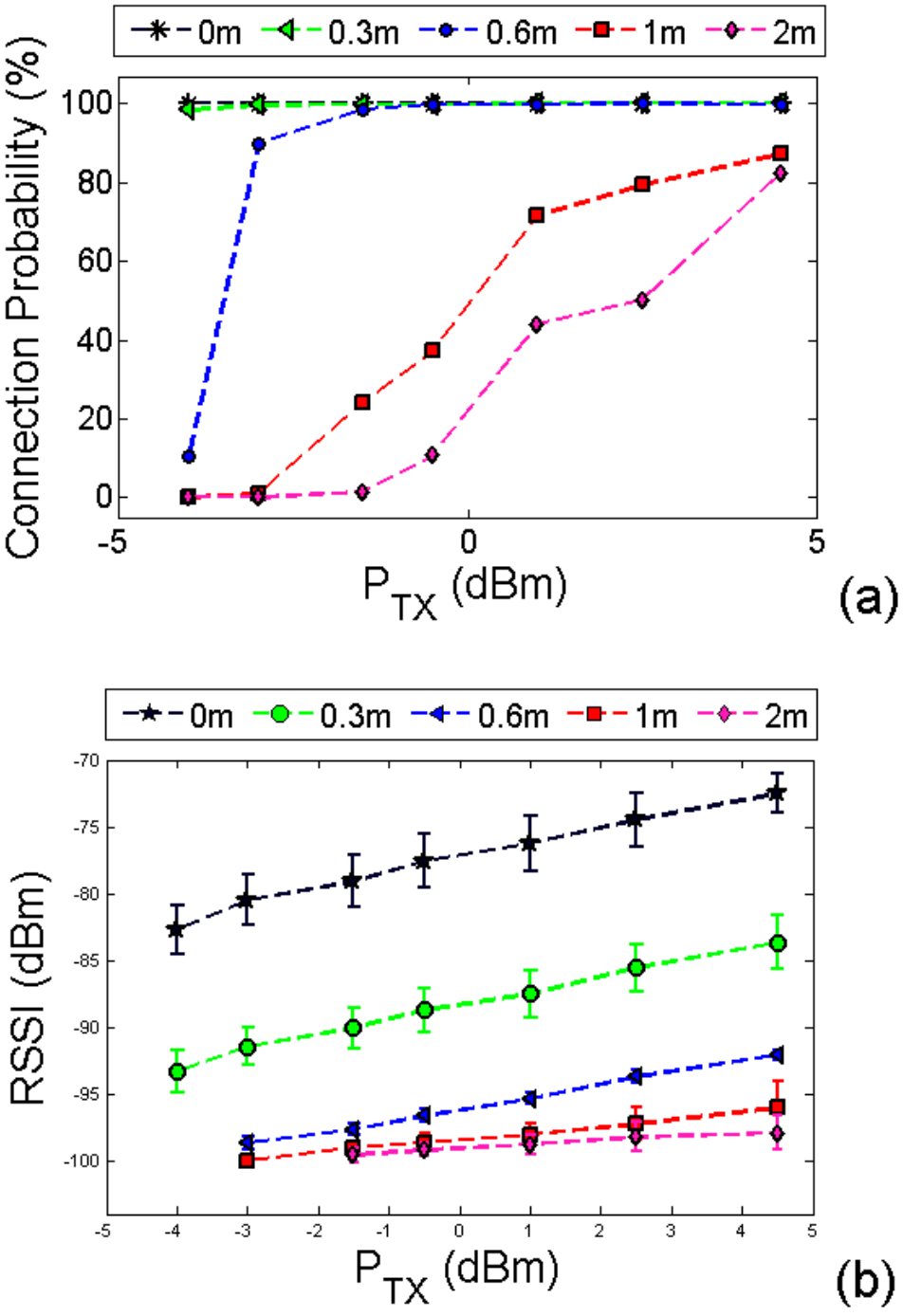

Figure II.10: (a) Probability to establish communication with the data bridge at different transmission power levels and distances. (b) The measured RSSI for the message received by the data bridge at different transmission power levels and distances.

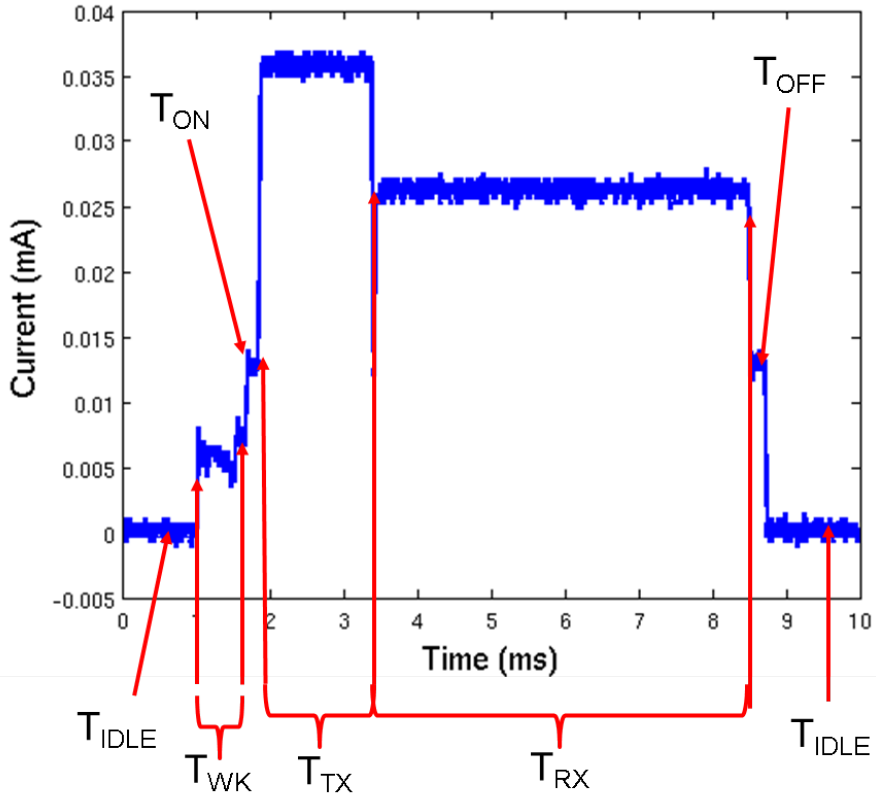

Figure II.11: Current consumption profile for a master module transmitting a radio message at full P_{TX} with a 5 ms acknowledgement time out.

The experimental values of I_{ACTIVE} and I_{IDLE} acquired for each module with a voltage supply of 3.3 V are reported in Table II.1. It is worth mentioning that the values of I_{IDLE} for the 3DA, 3DM, 3DAG, 3DAM, 3DAMG, PT, 8ADC and 2AF&ADC modules were measured by driving the onboard digital components into low-power mode. Regarding the actuation and illumination modules (i.e., BSDCC, BSLDCC, and VI), I_{IDLE} was measured with no motors connected and with the LEDs off, respectively.

The current consumption of the master module was characterized with the same setup, but with a different protocol. In particular, we focused on analysing the wireless transmission of a radio message during the APPLICATION state (S4 in the example described in section II.2). The plot in Fig. II.11 shows the single phases of a message transmission and acknowledgement time out expiration with the master module operating at a transmission power P_{TX} of 4.5 dBm and a 5 ms time out. After a period T_{IDLE}, the MCR exits from the idle mode and switches on the digital core during T_{WK}. After an additional T_{ON}, the

radio is active and a radio message with 0 bytes of data is sent during T_{TX}. Referring to Fig. II.6, the message transmitted in this example consists of 29 bytes (i.e., the RF frame and the payload with no data) and takes 1.38 ms. If data are transmitted, the T_{TX} period increases by 47 μs per byte sent. Once the radio transmission is over, the master module switches to the radio receive mode for T_{RX}, until an acknowledgement is received or the time out expires. In this example, we let the time out expire; thus, T_{RX} is 5 ms. Next, the radio and the core switch off during T_{OFF}, and the master module goes back to idle mode. This example can be generalized considering that T_{IDLE} is decided by the user depending on the level of responsiveness required by the MCR for the specific application, and that T_{ON} or T_{OFF} can be expanded in case of sensor data acquisition or actuator operation (both actions that typically do not require the radio in active mode). The experimental values of current consumption for each specific state of the microcontroller are I_{IDLE} = 9 μA, I_{WK} = 5.8 mA, I_{ON} = I_{OFF} = 12.9 mA, I_{TX} = 36 mA, and I_{RX} = 26.3 mA. It is worth mentioning that these values deviate from what is reported in the data sheet [49] by less than 2%.

As detailed in [50], the battery lifetime can be estimated by using the following average current consumption:

$$\overline{I} = \frac{\sum_i I_i T_i}{\sum_i T_i}, \tag{II.1}$$

where I_i and T_i are the current consumption and the time interval related to a single action performed by the MCR within a periodic operation. Considering a worst case scenario of no sleep between consecutive message transmissions (i.e., T_{IDLE} null), 29.69 mA is the average current drained by the master module in the example of Fig. II.11.

Equation II.1 can be used to predict $\overline{I}$ for a generic MCR by including the current consumption values reported in Table II.1 for the specific modules composing the MCR, and by considering the time periods when each module is active or idle. Once $\overline{I}$ is available, the battery lifetime in hours can be estimated simply by dividing the battery capacity – typically provided in Ah (Ampere-hours) – by the average current consumption.

***In Vivo* Trial**

The reliability of the wireless connection and the temperature behaviour of the same MCR described in Section II.2 were assessed *in vivo* on an anaesthetized porcine model. The porcine surgery was performed at Vanderbilt University under IACUC protocol M/14/014. A 56 kg female Yorkshire swine was used for this study. After intravenous sedation, an over-tube (Guardus Gastro, US endoscopy, USA) was placed in the upper GI tract to facilitate the endoscopic introduction of the MCR into the stomach.

In this case, the wireless connectivity test was focused on pressure and temperature data streaming from the MCR to the data bridge at different levels of P_{TX} and different distances of the data bridge from the animal. The communication protocol described in Section II.2 was adopted, and 200 bytes of payload were transmitted for each value of P_{TX} (range: -4 dBm..4.5 dBm) and distance (0 m, 1 m, 2 m, and 3 m). The application implemented error checking to notify the workstation for missing packages. A package was considered lost after three transmission retries. The experimental results are presented in Figure II.12.

The minimum RSSI needed to achieve a package loss below 20% was -86.9 ±0.62 dBm at 0 m with a P_{TX} of -4 dBm, -98.21 ±0.34 dBm at 1 m with a P_{TX} of 1.5 dBm, -98.57 ±0.55 dBm at 2 m with a P_{TX} of 2.5 dBm, and -99.19 ±0.48 dBm at 3 m with a P_{TX} of 2.5 dBm.

With a P_{TX} of 2.5 dBm, we were able to achieve a package loss below 20% within 2 m of the animal. In this configuration, the average current consumption of the MCR during data broadcasting was 25.9 mA. Considering the main application data streaming frequency of 166 Hz, the MCR was able to transmit data for 110 minutes with a 50 mAh battery.

Regarding the thermal behaviour of the MCR, the temperature acquired by the PT module reached a plateau of 37°C within about 10 minutes after introducing the capsule into the stomach of the animal. Afterwards, the recorded temperature variation was within 0.6°C.

II.3 Conclusions

In this chapter we introduced a platform to foster the development of MCRs. With its modular and reconfigurable approach, pursued at both the hardware and firmware levels, the platform gives the MCRs research community a number of constitutive bricks that can be assembled together to obtain different functionalities. This approach has the potential to lower the barriers to design space exploration in terms of the effort and skills required, thus allowing a wider community to experiment with novel MCR designs.

Our main contribution is ready-to-use modular hardware in the form of miniature, round boards, accompanied with a highly reconfigurable and open source software stack. The low power operation, safety and reliability of wireless communication were experimentally assessed via *in vitro* and *in vivo* trials. Aside from what is currently presented in this chapter, developers will be able to implement additional modules and to integrate custom solutions into the architecture by following its guidelines. This will expand the component libraries and provide even further support to the MCR design community.

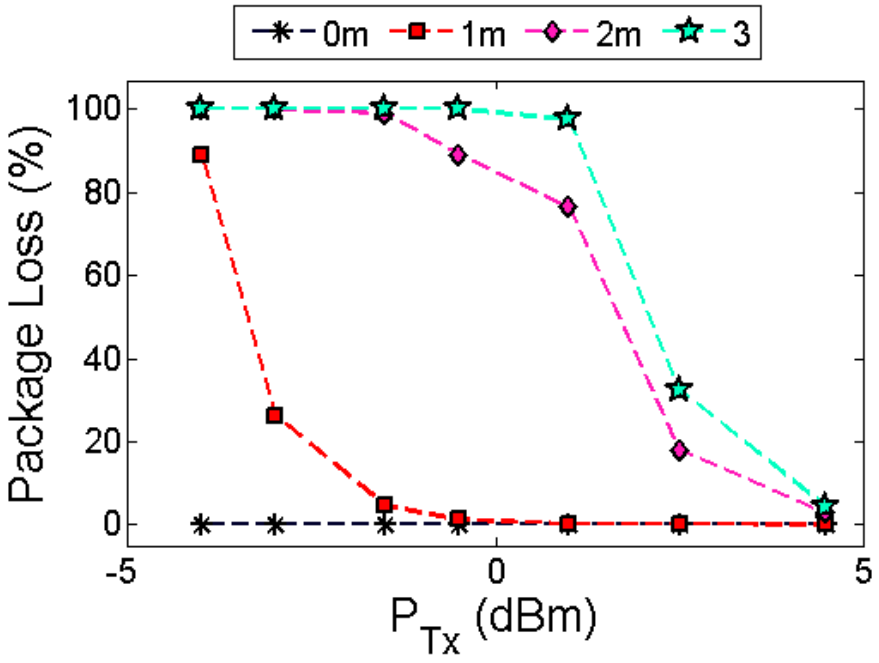

Figure II.12: Percentage of lost packages during the *in vivo* trial.

II.4 Discussion

In terms of the limitations of the current platform, better physical connectivity between the modules must be implemented to improve reliability and further reduce the effort required to assemble a specific MCR. Currently, the authors are exploring flexible and magnetic connectivity to address this issue.

Wireless connectivity for the STORM Lab Modular Architecture for Capsules (SMAC) modules across biological tissues is limited to 2 m. This is typically sufficient for exchanging data between a MCR inside the body of the patient and the data bridge in close vicinity. If a larger distance needs to be covered by the wireless communication, a power amplifier must be integrated in the data bridge, or use different carrier (i.e. 433 MHz).

Future work will aim to extend the SMAC libraries to include additional microprocessors, sensor and actuator modules, and wireless transceivers implementing different communication protocols and carrier frequencies (e.g., Low Power Bluetooth, 433 MHz).

Chapter III

FURTHER DEVELOPMENT OF THE ARCHITECTURE

In this chapter is described further development of the architecture presented in chapter II. Both the hardware and software limitations of the previous version of the architecture are here addressed. In particular the hardware modules have been improved resulting in a better connectivity thanks to a developed flexible circuit that provides exchangeability and easy reconfigurability of the different modules up on the application. Furthermore the platform can now support different wireless telemetries and CPU. In addition, to speed up the prototyping process, the MCR is programmed using TinyOS instead of bare-bone C. We present the hardware architecture of the platform, and the motivation for using TinyOS. To show the viability of TinyOS, we present results from an experiment involving sensing, actuation and wireless communication.

III.1 Systematic design of MCR

The modular architecture to design of pill-size medical devices, presented in chapter II, presented some limitations that have been addressed with further development. In details:

- **Connectivity for faster and easier assembly of MCR**
  Better physical connectivity between the modules had to be implemented to improve reliability and further reduce the effort required to assemble a specific MCR. The connectivity is provided by solderable pads which are available on each module for wired connectivity. However, having a library of hardware modules still requires the developer time for soldering and assembling the MCR prototype. Having a connectivity mechanism without the need of physically solder together the modules would reduce the prototyping time as well as increase the MCR reliability.

- **Extended modules library for design optimization**
  Optimal designs require multiple choices for the individual submodules including CPU, wireless communication, sensors and actuators. This can be achieved by extending the libraries to include additional microprocessors, sensor and actuator modules, and wireless transceivers implementing different communication protocols and carrier frequencies (e.g., Low Power Bluetooth, 433 MHz).

- **Tool chain and software libraries**
  The architecture software like for the other state-of-the-art MCR has being developed

from scratch and implemented in a relatively low-level language such as C. It typically runs directly on top of the hardware with no operating system. Although the modular architecture provides to the developer a set of open source libraries debugging and fine-tuning hand-crafted applications is time consuming, error-prone, and requires extensive expertise with limited opportunities for effective code reuse. The firmware stack as now is written in the C programming language and can be compiled by any standard C compiler, such as Code Composer (Texas Instruments, USA), IAR Embedded Workbench (IAR Systems, USA) or Eclipse (Eclipse Foundation, CAN) [49,55,56] but it runs as an HAL without the support of an operating system.

A better connectivity can be implemented with a **a flexible circuit**: this circuit consists of a versatile communication and power distribution backbone with multiple connectors for greatly reducing the time needed to assemble MCR prototypes. The different hardware modules can be mounted before to fold the circuit which forms the body of the MCR as shown in Figure III.1. The flexible circuit has a width of 10.4 mm and a length of 72.5 mm and can be folded down to a 14 mm length when all slots are populated. The backbone can host up to five different modules using 30-pin miniature connectors. The central connector is dedicated for the CPU module, while the other four slots accept arbitrary modules, thus providing extreme flexibility to the designer. Data connectivity is achieved by sharing SPI, Inter-Integrated Circuit (I^2C), ADC inputs, and GPIOs with the CPU module. Furthermore this circuit can be plugged to a debugger board with an Flat Printed Circuit Cable (FPC) connector for programming and debugging. This connectivity feature was implemented on the the flexible circuitry to easily interface with the rest of the hardware. Developers, once their application is completed, can cut this extra part from the flexible and since any module can be interfaced with the board with mating adaptor board, it can be reprogrammed anytime.

Development of MCR can result a challenging process considering the small size of the hardware and the few available test-points. Developers need to test intensively their custom modules while implementing their application before moving to the flexible board as well as access easily the hardware pins. Furthermore MCRs communicate data with other subsystems (e.g. a data bridge) that are typically connected to a personal computer. Therefore a development and programming board was developed to assist users in developing application with our platform. In particular user can test on this hardware any applications before migrating to the miniaturized module using the same GPIO for their application. Radio modules can be mounted on a dedicate connectors for testing, as well as any other hardware

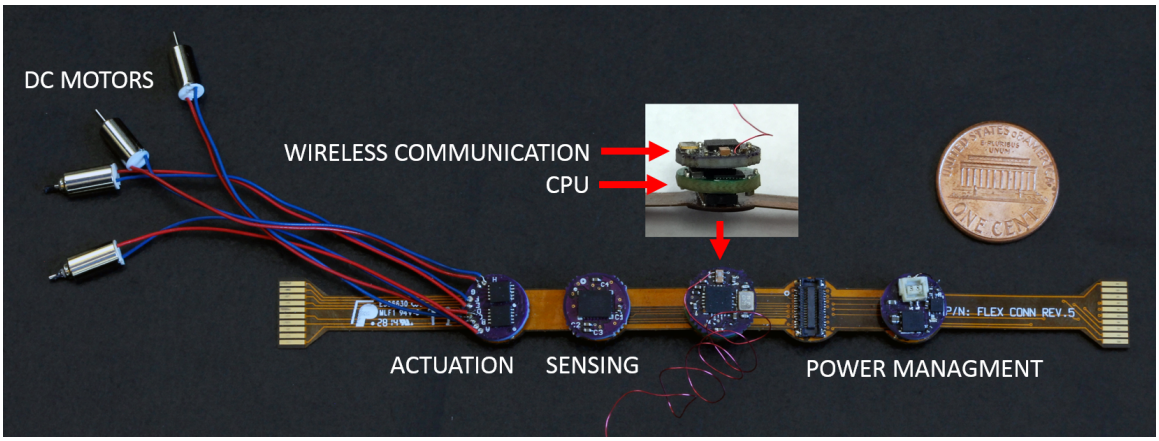

Figure III.1: The flexible circuit with hardware modules before folding in a shape that can be integrated inside an MCR. The flexible circuit can host up to five different modules. In this case the wireless communication module is plugged on the CPU module in the central slot. The other slots are respectively hosting an actuation module, a sensing module and the power managing module.

Module Name	Functionality	IC	Diameter (mm)	Thickness (mm)	Max Consumption (mA)
MCU	Microcontroller	MSP430F5528	10.5	3.84	2.32
433 MHz Transceiver	Wireless Communication	CC1101	10.5	3.94	29.2
6DOFAG	Sensing	LIS330DLC	10	4.04	0.01
6DOFAG	Sensing	LIS330DLC	10	4.04	0.01
Power	Power Management	NCP606, LTC4065, LTC2942	10	3.84	500 (Max)

Table III.1: Summary of currently available modules

module. The board furthermore, implements USB programmer and serial communication with the personal computer.

An extended library of modules The modules described in the previous chapter thus has been extended in addition to the ones in this table. In particular, we have included two new wireless communication modules, respectively a 433 MHz and a 2.4 Bluetooth low power module. The architecture now features a step up module that is able to provide to actuators up to 5 V when more corrent/torque is needed. Furthermore, in order to be placed in the flexible circuit that can be folded all the modules have been manufactured with a tickness of 0.7 mm with the exception of the microcontroller (MCU) and the wireless communication that are still 1.6 mm tick.

Finally, to open up the area of MCRs to people who are not experts in embedded software **a high-level—primarily visual—design environment user interface** would significantly lowers the barrier of entry into MCRs. This environment would use a model-based approach where all hardware modules and software components are represented by a component model. Users select models from a library and build their application by

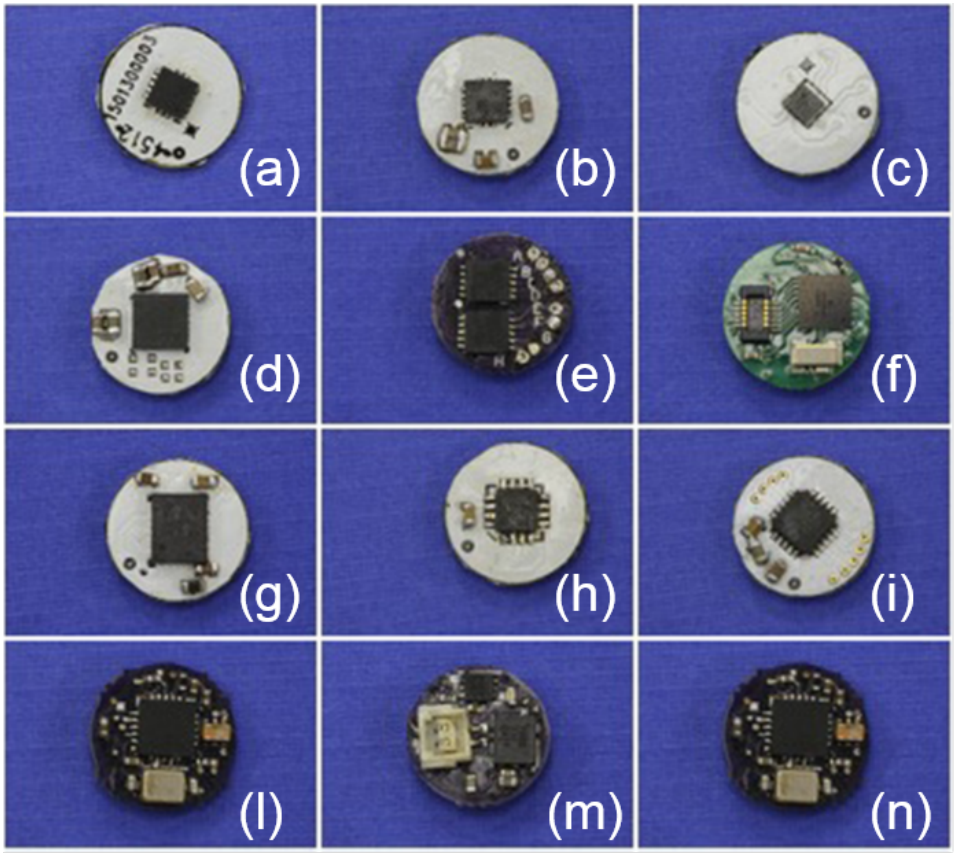

Figure III.2: The architecture modules.

composing the models on a visual canvas. Its creation requires software components corresponding to the existing modules. Therefore TinyOS, was selected as a possible operative system for the architecture and it lays the foundation for an integrated design environment. TinyOS, [59] is a configurable modular operating system that was specifically designed for resource-constrained platforms such as Wireless Sensor Networks (WSN). The component based programming paradigm of TinyOS creates a one-to-one map between hardware modules and TinyOS components. Component models will be added to this repository as new hardware modules are created by various researchers. The repository will serve as a channel of collaboration fostering design reuse. The development of design environment for MCR goes beyond this proposal but the presented modular architecture lays for its creation.

III.2 Results

The viability of an MCR is strongly correlated with its power consumption. Energy sources for MCR are usually limited to less than 100 mAh due to battery size constraints. Therefore, an MCR has to conserve its energy in order to last long enough to perform its task. Typically, MCR applications consist of a repeating pattern of sensing, wireless communication and actuation. Thus, we designed our experiment to exercise these components separately while taking current measurements. It is worth noting that, while actuators consume the most power, they are difficult to use for a comparative analysis because they are highly application specific. We have included them in our experiment in order to present a fully working MCR. The main focus of the experiment was to measure the average power consumption of the platform configured as a typical MCR prototype. Of particular focus was the wireless communication module because it is the one component that consumes the most power (other than the actuators) and is used frequently in all MCR applications. Additionally, we wanted to measure the responsiveness of TinyOS and the amount of overhead it placed on the system.

Our bench-top experiment consisted of the MCR embedding the main MCU module, the 433 MHz Transceiver module, the BDCC actuation module, the 6DOFAG sensing module and the power module. Two brushed DC motors (MK04 S-24, Didel, Switzerland) were then connected to the BDCC output lines. As regards to power, a 30 mAh, 3.7 V rechargeable LiPo battery (Shenzhen Hondark Electronics Co., Ltd., China, 12 mm $\times$ 10 mm $\times$ 2 mm in size) was used in the power module which supplied regulated voltage to the rest of the MCR circuitry. The modules were then mounted on the flexible circuitry, and the voltage drop across a 10-Ω resistor placed in series to the positive supply terminal of the battery was sampled with a digital oscilloscope (Tektronix, TDS12014C, USA).

The setup also included a base station that was collecting sensor data from the MCR

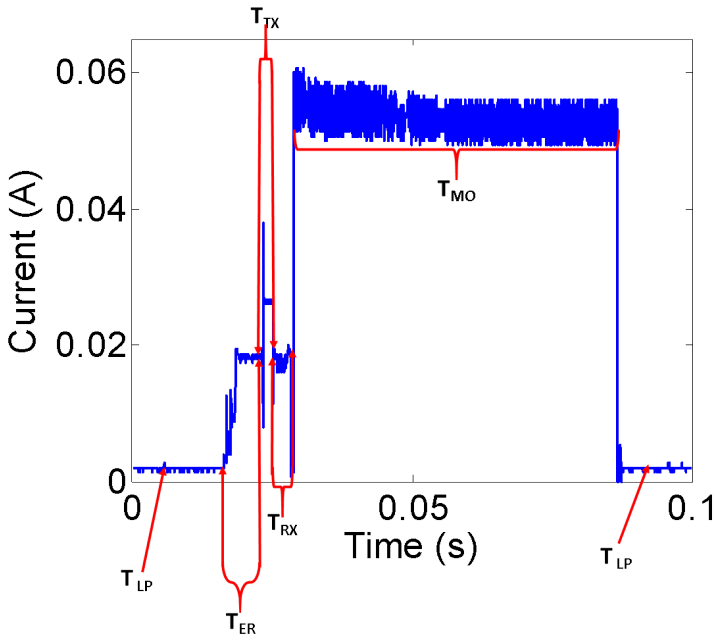

Figure III.3: Current consumption of the MCR prototype showing levels of current consumed for different system states.

and sending actuation commands. The MCR was running a TinyOS application which had a periodic pattern of:

1. acquiring data from the sensing module,
2. sending a radio message with the acquired data,
3. waiting for an actuation command from the base station,
4. driving the motors and finally,
5. going back to idle state until the next data acquisition.

The sensor sampling rate, the duty cycle of the PWM signal for the motor, and the motor-on time were controlled in the MCR application by commands sent from the base station. The plot in III.3 shows a single instance of the periodic message transmission with the MCR operating at a transmission power P_{TX} of 10 dBm and a sampling rate of 0.5 Hz, with the motor being actuated for 60ms with a 50% duty cycle PWM signal. During the time interval T_{LP} the MCU was either in an idle state or acquiring data from the sensing module, while the wireless module was inactive in a low power mode. After the sensor data acquisition, the MCR turned on the wireless module in T_{ER} (2.68 ms) and transmitted the

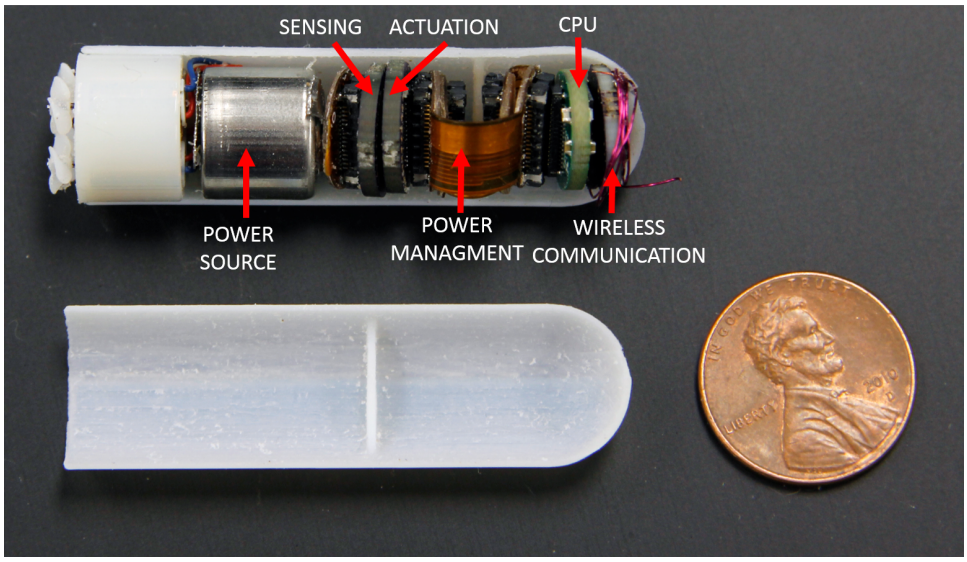

Figure III.4: The swimming capsule without the lateral shell to show the internal hardware components.

wireless message at a data rate of 125 Kbps during T_{TX} (1.8 ms). The transmitted message consisted of 18 bytes, 6 of which were the acquired sensor data while the rest were the IEEE 802.15.4 header and other overhead used by the TinyOS MAC and CC1101 physical layer. Once the radio transmission was completed, the MCU entered reception mode for T_{RX} of 2.9 ms during which it received a message from the base station that consisted of 6 bytes of payload including the actuation command, the sampling rate, the motor-on time, T_{MO}, and the PWM duty cycle. During T_{MO} the wireless module is is put in low power mode while motors are driven for the requested time interval. Subsequently the system went back to the idle state until the next data acquisition.

The average experimental values of current consumption for each specific state were I_{LP} =1.8 mA, I_{ER} = 14.5 mA, I_{TX} = 26.6 mA with a peak of 28.3 mA, I_{RX} =17 mA, and I_{MO} = 52.6 mA. Excluding the motor, the average current consumption for the sensing and communication tasks was 17.2 mA, which is 49% less than the typical current consumption exhibited by 2.4 GHz based MCR platforms as reported in [60]. The result shows that the hardware platform achieves the level of low power operation required by typical MCRs applications. It also shows that no significant overhead was accrued by using TinyOS. The responsiveness of TinyOS and the performance of the wireless communication module are on par with other MCR systems that implement real-time control using bare-bone C (no OS) or using a pseudo-kernel approach [61].

III.3 Conclusion

In this chapter we have introduced the further steps toward an open architecture and supporting design environment for MCR. The designer - whether an expert or a novice in embedded systems - will be able to focus on selecting pre-designed modules and programming the MCR to fulfill a specific task, rather than designing, fabricating, and connecting together miniature electronic boards. This will speed up the time-to-prototype, reducing the gap from concept to experimentation.

Future work will aim to extend the library to include additional microprocessors, sensor and actuator modules, and wireless transceivers implementing different communication protocols and carrier frequencies (e.g. Low Power Bluetooth). In particular, the authors are exploring to extend the proposed platform to ARM Cortex microprocessors (e.g. the CC2650 from Texas Instruments). This module consists of a 2.4 GHz radio and a high performance ARM CPU, which will further reduce the folded capsule size. Other devices that integrate similar CPUs and other wireless communication protocols will be made available in the future.

III.4 Discussion

The main downside of a modular approach, however, is that a system made of modules is not optimized for the particular application, and it usually causes overall an increment of the system size if compared to a custom device. The best course of action for MCR designers would therefore be to validate their hypotheses and preliminary designs using the proposed platform, and then move to a custom approach as soon as they are satisfied with the results. At that stage, compliance with regulatory standards and guidelines (e.g. IEC 60601) must also be addressed. While the current modules available in the on-line repository should be compliant with the IEC 60601 standard, a rigorous risk analysis and compliance check were both outside the scope of our work.

The proposed approach for rapid prototyping of capsule robots follows the "democratization" of embedded systems promoted by the introduction of Arduino and other open source platforms, and lends itself to adoption well beyond medical research. In particular, we plan to release a simplified version of our architecture that can be adopted by pre-college students and by the growing number of tech enthusiasts from the maker movement. While it is too soon to speculate on the broader implications of the adoption of our approach, we hope that lowering the barriers to the design of new medical capsule robots will lead to a day when colorectal cancer screening will be as easy as swallowing a capsule.

Chapter IV

AN EXTENSIVE EXAMPLE APPLICATION OF THE ARCHITECTURE: WIRELESS TISSUE PALPATION

This chapter focuses on one of the applications where the modular architecture was used in order to design an MCR aiming to restore the tactile feedback in MIS procedures through wireless tissue palpation. Section IV.1 gives a brief overview on the state of the art on restoring perception in MIS. Section IV.2 introduces the first assessment of Wireless Tissue Palpation a single DOF. In its first implementation the device was driven using a a 6 DOF robotic arm. For a better maneuverability and usability of the device, in section IV.3 we discuss the outcomes of the second version of the device. This device features 3 DOFs real time localization and a pressure sensor head embedded in silicone rubber while actuation is provided by the surgeon using a laparoscopic grasper. This section presents the results of the device assessment in both *in-vivo* and *ex-vivo* trials. Section IV.4, describes further results derived from the silicone head characterization and finally section IV.5 presents some more results obtained with the device on *ex-vivo* organs (*i.e* liver, prostate).

IV.1 The role of tissue palpation in MIS

Restoring tactile and kinesthetic sensations in MIS and robotic MIS has been an active research topic for more than two decades [62, 63], with one of the first systems used in a human dating back 1994 [64]. A relevant number of MIS instruments with force and/or tactile sensors have been developed to acquire *in vivo* data for tissue modeling and simulation [65–68], to improve the outcomes of the surgical procedure – preventing excessive forces from being applied to the tissues [69–73], or to explore tissues and organs by palpation [74–77]. This last functionality is particularly relevant whenever location and boundaries of a hidden tumor must be located – registration with pre-operative imaging is not effective for soft tissues [74, 76], or to identify buried structures (*e.g.*, nerves or blood vessels) that must be avoided during the surgical procedure. MIS devices for tissue palpation developed to date exploit different approaches, such as grasping [63, 67, 71], rolling indentation [74], or vertical indentation [65, 66, 68, 75, 76].

However, the fact that no commercial MIS instruments with embedded force and/or tactile sensors have been adopted clinically so far [78] illustrates that there exists a significant roadblock preventing the translation of potentially transformative prototypes into clinical practice. Focusing on MIS palpation devices, a possible barrier may be that surgeons are

not yet willing to devote a surgical port to an instrument whose sole purpose is to palpate tissues.

IV.2 Wireless Tissue Palpation: proof of concept for a single degree of freedom

Focusing on MIS palpation devices, a possible barrier may be that surgeons are not yet willing to devote a surgical port to an instrument whose sole purpose is to palpate tissues. Therefore, providing a tissue indenter that does not require port space may overcome this potential adoption barrier. Therefore a wireless approach to tissue indentation, where a magnetic palpation device can be deployed through a standard trocar and operated without requiring a dedicated entry port was presented by the author in [31]

Referring to Fig. IV.1, the approach we propose takes advantage of an external magnetic field source and an intra-body wireless palpation device (WPD) – embedded with a miniature permanent magnet and wireless electronics. The WPD can be introduced into the abdominal cavity through a standard trocar and positioned on the target by a laparoscopic grasper. Then, tissue indentation can be obtained by properly modulating the gradient of the external magnetic field. In order to generate kinesthetic data, the indentation depth and the pressure applied on the tissue must be known at any given time. In this pilot study, we restricted the investigation to a single degree of freedom (*i.e.*, vertical indentation) as a first step toward proving the feasibility of the proposed approach.

A permanent magnet mounted at the end effector of a robotic manipulator was adopted as external magnetic field source. Considering the two magnets (*i.e.*, the one inside the WPD and the one at the external manipulator) oriented as in Fig. IV.1, we studied the indentation of a tissue sample along the vertical direction by cyclically translating the external magnet along the Z axis. Neglecting gravity and assuming a pure vertical motion for the WPD, the pressure exerted on the tissue is provided by the ratio of the intermagnetic force along the Z axis, F_z, and the area of the WPD face in contact with the tissue. At the equilibrium, the intensity of F_z can be measured by placing a load cell in between the external permanent magnet and the end effector of the manipulator, as suggested in [79]. For vertical indentation as represented in Fig. IV.1, gravitational force acting on the WPD can be considered as a preload on the tissue and factored out as an offset in the indentation trial. For any other configuration, an accelerometer can be embedded in the WPD to provide the inclination, thus allowing to quantify the exact contribution of the gravity force, should this vary during indentation. In this work, the inertial sensor is primarily used to verify the assumption of pure vertical motion for the WPD.

The indentation depth $\delta(t)$ can be evaluated by measuring the Z component of the magnetic field at the WPD. In particular, referring to Fig. IV.1 and focusing on the tissue

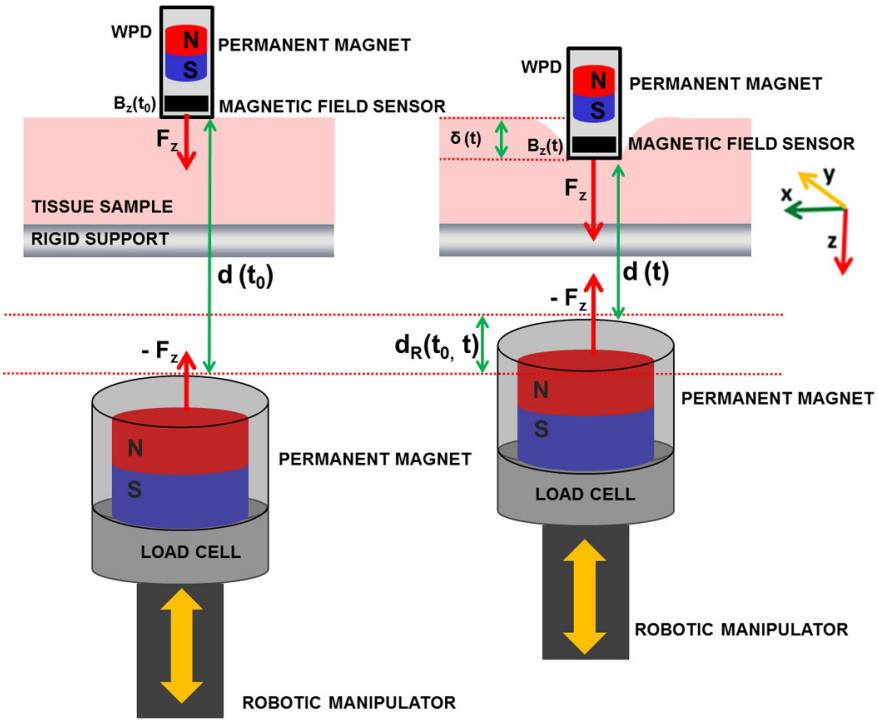

Figure IV.1: Schematic diagram for wireless vertical indentation at the initial time t_0 (left) and at a generic time t (right) during the loading phase.

loading phase, it is possible to express the distance between the external magnet and the internal magnet at the generic instant t as:

$$d(t) = d(t_0) - \delta(t) - d_R(t_0, t) \tag{IV.1}$$

where $d_R(t_0, t)$ is the vertical distance traveled by the robotic manipulator since the beginning of the loading phase occurred in t_0. Since the motion of the external magnet is limited to the Z axis and the WPD is aligned on that same direction in virtue of magnetic coupling, we can assume that the Z component of the magnetic field at the WPD, $B_z(t)$, is an univocal function of $d(t)$ [80]:

$$B_z(t) = \Phi[d(t)] \tag{IV.2}$$

that can be numerically quantified through experimental calibration. Therefore, the indentation depth $\delta(t)$ can be expressed by merging Eq. IV.2 with Eq. IV.1 and rearranging the terms as:

$$\delta(t) = \Phi[B_z(t_0)]^{-1} - \Phi[B_z(t)]^{-1} - d_R(t_0, t). \tag{IV.3}$$

Since the value of $d_R(t_0, t)$ is available from the robotic manipulator encoders and $B_z(t)$ can be measured by placing a Hall effect sensor in the WPD, the total indentation depth can be computed at any given time during the loading phase. The same mathematical formulation applies – *mutatis mutandis* – to the tissue unloading phase.

A relevant assumption for the proposed approach consists of considering all the tissue deformation occurring at the interface with the WPD. This holds true for the schematization represented in Figure IV.1 – where the tissue being tested is laying on a rigid support. However, it may not be valid during *in vivo* conditions, where a stiffer organ may lay on a softer tissue. This approximation is, however, well accepted in the field of *in vivo* tissue indentation, as long as the indentation depth is relevantly smaller (approximately 10-15% of the total thickness) than the organ under test.

Experimental Platform Overview

The experimental platform used to assess wireless tissue palpation for a single degree of freedom is represented in Fig. IV.2. It mainly consists of the WPD, the robotic manipulator, and the tissue being tested.

The WPD cylindrical shell is embedded with a permanent magnet, a sensing module, a wireless microcontroller, and a battery (Fig. IV.3). We selected an off-the-shelf cylindrical NdFeB permanent magnet (K&J Magnetics, Inc., USA), 11 mm in diameter and 11 mm in

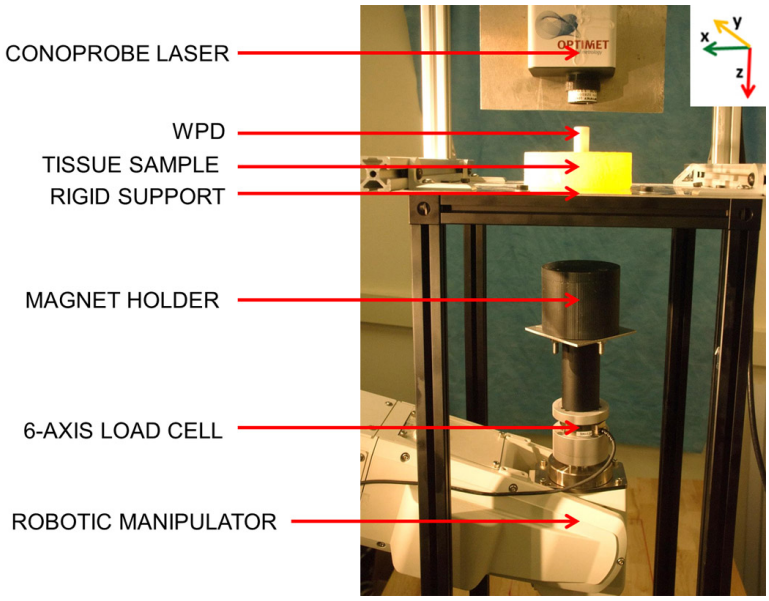

Figure IV.2: Robotic platform for wireless vertical indentation. The four edges of the rigid support lay on a black supporting frame. The conoprobe laser is used for indentation depth validation.

height, with N52 axial magnetization (magnetic remanence of 1.48 T). The sensing module consisted of a Hall effect sensor (CYP15A, ChenYang Technologies GmbH & Co. KG, Germany) to measure B_z, and a triaxial accelerometer (LIS331AL, STMicroelectronics, Switzerland) – to verify that the WPD motion during indentation was limited to the Z direction.

An analog signal conditioning stage connected to the Hall effect sensor output allowed for canceling out the offset due to the onboard permanent magnet (*i.e.*, 100 mT), for applying a low-pass filter (cut-off frequency of 30 Hz), and for amplifying the magnetic field signal (x29), resulting in a resolution of 0.32 mT and a sensing range of $\pm$130 mT. An analog to digital converter (ADC) (ADS8320, Texas Instrument, USA) was used to acquire this voltage with a sampling rate of 1 kHz and a resolution of 16 bits. The result of the conversion was then transmitted through a serial synchronous interface to the wireless microcontroller (CC2530, Texas Instruments, USA). The signals generated by the accelerometer – that did not required a 16-bit resolution for the sake of their purpose – were acquired directly by the microcontroller through its embedded 12-bit ADC at 100 Hz. Accuracy results after digitalization were 0.35 mT for the Hall effect sensor and 1.4 degree for the accelerometer used as inclinometer. Real-time clock timestamps were associated with each single measurement to enable synchronization with signals acquired by the external platform. The data were

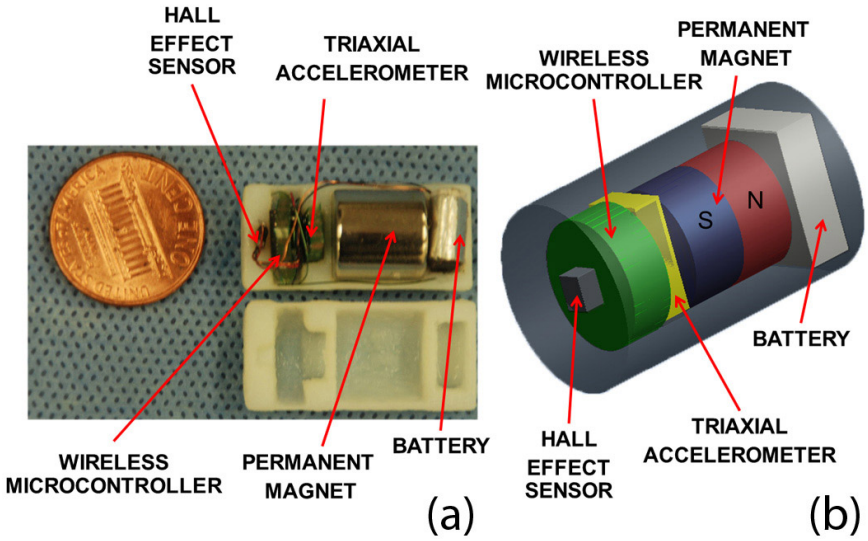

Figure IV.3: Picture (a) and schematic view (b) of the wireless palpation device.

transmitted over a 2.4 GHz carrier frequency to a receiving unit located in the same room and connected to a personal computer, where data were unbundled, displayed, and stored. The use of a 2.4 GHz carrier frequency was demonstrated to be effective in transmitting data through living tissues in [50, 81]. The wireless microcontroller was integrated into a custom-made 9.8 mm diameter printed circuit board, together with radiofrequency components. A digital switch driven by the microcontroller was placed between the battery and the sensing circuitry, to save battery power when measurements were not required.

A 15 mAh, 3.7 V rechargeable LiPo battery (030815, Shenzhen Hondark Electronics Co., Ltd., China) was used as the onboard power supply. The battery layout (originally 8 mm $\times$ 15 mm $\times$ 3 mm) was reduced to fit the cylindrical shell. Considering that data acquisition and transmission requires an average of 33 mA, battery lifetime was almost 30 minutes. Operational lifetime can easily be extended to fit application requirements by maintaining the WPD in sleep mode (average current consumption of 1.5 μA) and waking up the system by remote triggering whenever a palpation task is going to be performed.

As represented in Figure IV.3, all the components were integrated inside a cylindrical plastic shell fabricated by rapid prototyping (OBJECT 30, Object Geometries Ltd, USA). Thanks to its small size (12.7 mm in diameter and 27.5 mm in height), the WPD can be introduced through a 12-mm surgical trocar (*e.g.*, the 5-12 Vesaport Plus, Covidien, USA has an inner diameter of 13 mm). An axial-symmetric design was pursued in order to keep the WPD center of mass along its main axis, thus guaranteeing an uniform pressure on the tissue. Considering vertical indentation, the WPD surface area in contact with the tissue

was 113 mm^2, while the total weight was 117 mN (*i.e.*, WPD mass was 12 g). It is worth mentioning that a tether can be connected to the WPD, should the surgeon feel the need for a fast retrieval of the palpation device in case of failure.

Concerning the external part of the platform – represented in Fig. IV.2 – an off-the-shelf cylindrical NdFeB permanent magnet (50 mm in diameter and 50 mm in height, weight 772 g), with N52 axial magnetization (magnetic remanence of 1.48 T), was adopted. Considering an average thickness of the abdominal wall upon insufflation of 30 mm [82], this magnet was selected on the basis of numerical analysis [83] to operate at a distance along Z ranging from 35 mm to 75 mm away from the WPD. In this region, the simulated absolute values of the field gradient range from 3.75 T/m to 0.6 T/m, respectively. Considering the features of the magnet embedded in the WPD, the expected intermagnetic force spans from 4.7 N to 0.75 N. Should the required working distance be increased due to specific patient constraints (*e.g.*, larger body mass index), an external magnet with different features can be selected by running numerical simulations again.

The magnet was embedded in a plastic holder connected to a 6-axis load cell (MINI45, Ati Indutrial Automation, Inc., USA), having a resolution of 65 mN for the Z component of the force. The magnet-load cell assembly was mounted at the end effector of a six degrees of freedom industrial robot (RV6SDL, Mitsubishi Corp., Japan), presenting a motion resolution of 1 μm along the Z direction. It is worth mentioning that the holder was designed so to space the magnet enough from the load cell and the manipulator to prevent electromagnetic interferences. Data from the load cell were acquired by a dedicated acquisition board (NI-PCI 6224, National Instruments, USA) at a sampling frequency of 10 kHz, and merged with the manipulator position and the signals coming from the WPD.

The tissue sample being tested – silicone samples (M-F Liquid Plastic, MF Manufacturing, USA) with different stiffnesses or porcine liver, depending on the trial – was placed on a 2 mm thick rigid support, as represented in Fig. IV.2.

Finally, the algorithm described by Eq. IV.3 was implemented in Matlab (Mathworks, USA) upon experimental calibration. In particular, the numerical function Φ^{-1} was evaluated by placing the WPD directly on the rigid support and by recording $B_z(t)$ while moving the external magnet at a constant speed (*i.e.*, 3.12 mm/s) from a starting position 75 mm away from the rigid support along the Z axis (*i.e.*, d_R varying from 0 mm to 75 mm, where for $d_R = 75$ mm the top part of the holder was almost in contact with the lower side of the rigid support). This measurement was performed for five loading-unloading cycles, and the values were averaged. Given the exponential decay of the magnetic field with distance, a fifth-order polynomial function was used to fit Φ^{-1}, thus obtaining:

$$d(t) = \Phi^{-1}[B_z(t)] = \sum_{i=0}^{5} a_i \cdot B_z(t)^i \tag{IV.4}$$

with $a_0 = 185.6$ mm, $a_1 = -6.95 \cdot 10^3$ mm/T, $a_2 = 1.57 \cdot 10^4$ mm/T^2, $a_3 = -2 \cdot 10^7$ mm/T^3, $a_4 = 1.31 \cdot 10^7$ mm/T^4, $a_5 = -3.51 \cdot 10^7$ mm/T^5. The square of the correlation coefficient for the proposed fitting was $R^2 = 0.99998$.

Since we are proposing a novel method to quantify the elastic modulus of the material being tested, it is interesting to analyze in detail the error we should expect. Assuming vertical indentation, the error in measuring the stress straightforwardly depends on the accuracy of the load cell (*i.e.*, 65 mN). Concerning the indentation depth, the polynomial function in Eq. IV.4 is applied to a sensor reading affected by a given uncertainty ΔB_z. Considering $\delta(t)$ as expressed in Eq. IV.3, we can write its absolute error as a function of ΔB_z and Δd_R:

$$|\Delta\delta| <= |\frac{\partial \Phi^{-1}[B_z(t)]}{\partial B_z(t)}| \cdot |\Delta B_z| + |\Delta d_R|. \tag{IV.5}$$

Considering Eq. IV.3 and a negligible error in d_R – a reasonable assumption given the high manipulator position resolution, we then have

$$|\Delta\delta| = |\sum_{i=1}^{5} i \cdot a_i \cdot B_z(t)^{i-1}| \cdot |\Delta B_z|. \tag{IV.6}$$

This equation clearly shows how the accuracy of the proposed method depends upon the strength of the magnetic field at the WPD, which, for the proposed platform, is a function of the distance between the external magnet and the WPD. Thus, higher accuracy is obtained in a stronger magnetic field (*i.e.*, the shorter the distance between the WPD and the external magnet).

Experimental Results

Experimental validation of single degree of freedom wireless palpation consisted in three different trials. First, the effectiveness of the algorithm in reconstructing the indentation depth from magnetic field values was assessed. Then, three silicone tissue samples, each with a different elastic modulus, were indented with the proposed approach, and the results compared with standard indentation. Finally, a lump was embedded in a porcine liver and wireless palpation was used to identify differences in tissue stiffness.

Indentation algorithm assessment

An optical conoscopic holography sensor (Conoprobe, Optimet, USA) was adopted as reference measurement system. The conoprobe laser was pointed at the upper circular

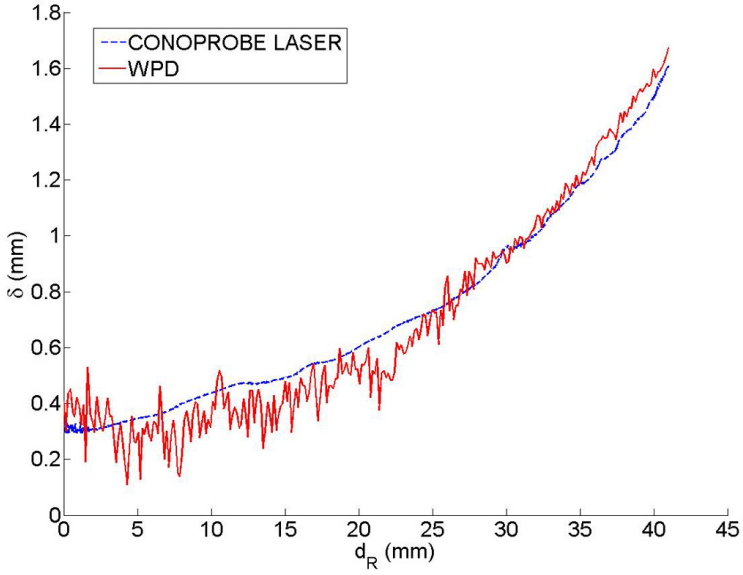

Figure IV.4: Tissue indentation depth plotted as a function of d_R and measured via the conoprobe laser and via the proposed WPD approach.

surface of the WPD, as shown in Fig. IV.2. The indentation test was performed on a squared silicone tissue sample (elastic modulus 64.49 kPa, thickness 35 mm, lateral side 75 mm) for d_R varying at a constant speed (*i.e.*, 3.12 mm/s) from 0 mm to 41 mm, where for $d_R = 41$ mm the top part of the external magnet holder was almost in contact with the lower side of the rigid support. Five loading-unloading trials were completed and error analysis was performed on the acquired data. Accelerometer output confirmed that WPD motion was only occurring along the Z direction.

A typical loading plot for $\delta(t)$ acquired with both the reference system and the proposed approach is represented in Fig. IV.4 as a function of d_R. Considering the tissue sample thickness, the rigid support, and the recorded indentation depth, the distance d from the external magnet to the WPD varied from 75 mm to 35 mm during the trials.

Concerning the error, the Hall effect sensor measurements presented a maximum measurement error of ± 0.3 mT. By using this value in Eq. IV.6 as ΔB_z, it is possible to plot an envelope of the expected maximum measurement error of the tissue indentation depth δ as a function of the distance d (Fig. IV.5). For all of the acquired measurements, the difference between the conoprobe laser reading and the reconstructed δ always fell within the envelope. One example is given in Fig. IV.5. From the same plot it is possible to see that the measurement error for δ is $\pm$ 0.1 mm at 35 mm, and increasing to $\pm$ 0.5 mm at 75 mm.

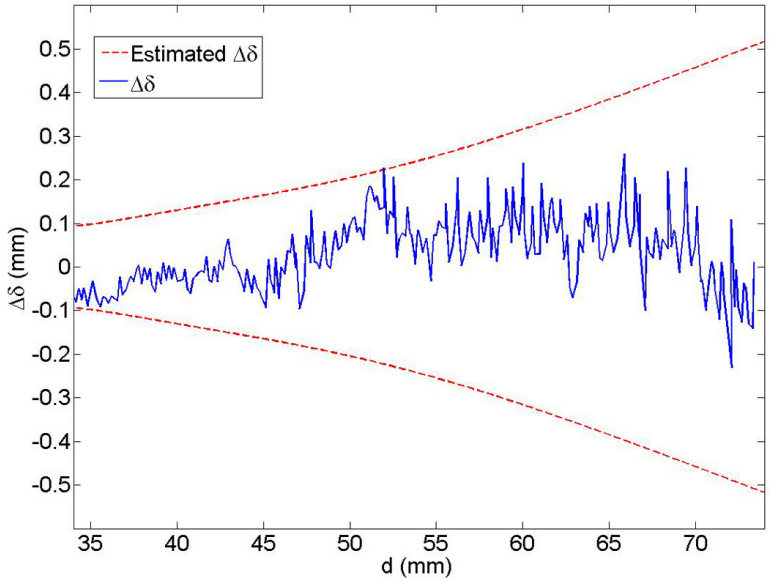

Figure IV.5: Tissue indentation depth error $\Delta\delta$ as a function of d for the WPD approach. The two dashed lines represent the envelope of the maximum measurement error for the tissue indentation depth, $\Delta\delta$, as a function of the distance d.

In vitro trials

In order to validate the effectiveness of wireless palpation to detect the elastic modulus like done when using a traditional indenter, three squared silicone tissue simulators (thickness 35 mm, lateral side 75 mm) were fabricated, each with a different proportion of hardener (*i.e.*, 20%, 25%, and 30%), thus resulting in different elastic moduli E1, E2, and E3 [84]. A traditional vertical indenter was obtained by replacing the magnet holder with a cylindrical probe at the interface with the load cell. The probe was designed to have the same contact area as the WPD. The indenter probe was first driven to touch the surface of the tissue layer with a preload of 0.2 N. Five loading-unloading trials – reaching an indentation depth of 3 mm – were performed for each tissue sample at a constant speed of 3.12 mm/s. Stress-strain plots obtained from a single loading are represented in Fig.IV.6a. Elastic moduli obtained by least square fitting were E1 = 50.75 kPa ($R^2 = 0.9973$), E2 = 64.49 kPa ($R^2 = 0.9935$), and E3 = 93.92 kPa ($R^2 = 0.9972$).

Wireless palpation was then performed on the same three samples. Five loading-unloading trials were performed by following the same protocol described for the assessment of the indentation algorithm (see Sec. IV.2). The results are reported in Fig. IV.6b. Also in this case, accelerometer data confirmed that WPD motion was always occurring along the Z direction. Indentation force reached 1.26 N, while indentation depth ranged from 0.85

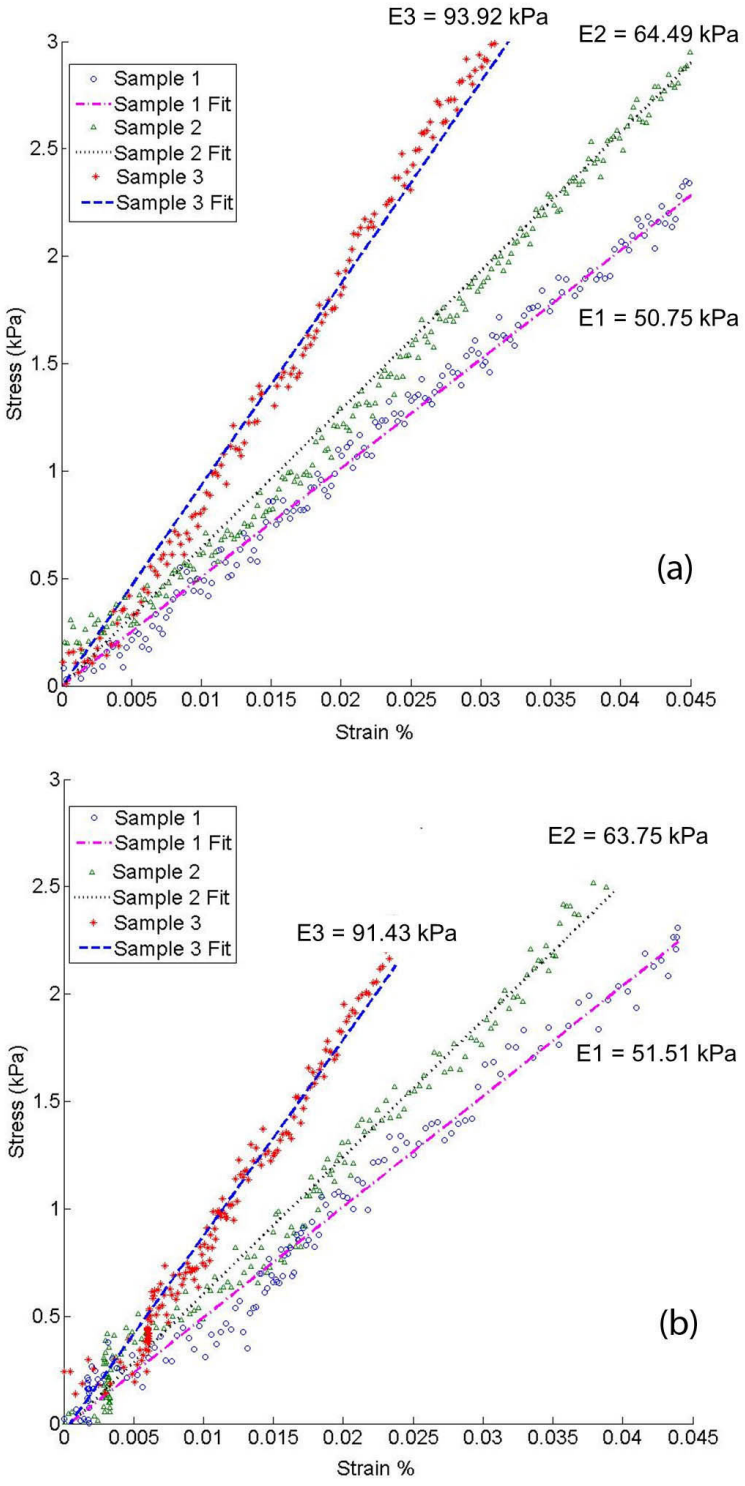

Figure IV.6: Experimental data acquired by standard indentation (a) and by wireless indentation (b) for three different silicone tissue samples.

mm for the stiffer sample to 1.57 mm for the softer sample. Elastic moduli obtained by least square fitting were E1 = 51.51 kPa ($R^2 = 0.9825$), E2 = 63.75 kPa ($R^2 = 0.9802$), and E3 = 91.43 kPa ($R^2 = 0.9608$). Considering all the performed trials, the average relative error for wireless palpation in measuring the elastic module was 1.5%, 1.1% and 2.8% for the tissue samples having E1, E2, and E3, respectively. The largest relative error occurred for the stiffer tissue sample. This can be explained by considering that the indentation depth for this sample was the smallest, thus the distance between the WPD and the external magnet was the largest among the trials, leading to the largest error.

Results

The result results lead to the conclusion that wireless vertical indentation is feasible in a laboratory setting, showing comparable results to traditional indentation techniques. Considering all the performed trials, the average relative error for wireless palpation in measuring the elastic module was below 3% for the tissue samples of different stiffness.

Given these encouraging – yet preliminary – results, the next step was to demonstrate wireless palpation in a more realistic setting, where the motion of the palpation device is not limited to a single axis. This further step requires real-time pose (*i.e.*, position and orientation) detection for the WPD, that can be used together with three-dimensional manipulation [17, 85, 86] to explore organ surfaces.

IV.3 Wireless Tissue Palpation for intraoperative detection of lumps in soft tissue

Consequently with the application of the modular architecture with a magnetic localization algorith presented in Di Natali in [35], we introduced for the first time an intraoperative wireless palpation probe (WPP) – schematically represented in Fig. IV.7 – that can be deployed through a trocar incision and directly controlled by the surgeon to create a stiffness distribution map. Such a map can then be used to localize tumor margins during soft tissue surgery, thus improving intraoperative diagnostic and interventional decisions. Wireless operation prevents the need for a dedicated port and reduces the chance of instrument clashing in the operating field. The research results for this application are here summarized and presented in Appendix D.

In this work, tissue reaction pressure is acquired by a barometric pressure sensor embedded in a silicone rubber at the probing surface of the WPP. A threshold value P_{th}, independent from $\mathbf{r}$, is defined by calibration and takes into account both bias and noise of the pressure sensor. A single indentation starts as $P(\mathbf{r}) > P_{th}$. The pressure sensing head showed a sensitivity of $P_s = 34$ Pa (*i.e.,* considering the probing area, this is equivalent to

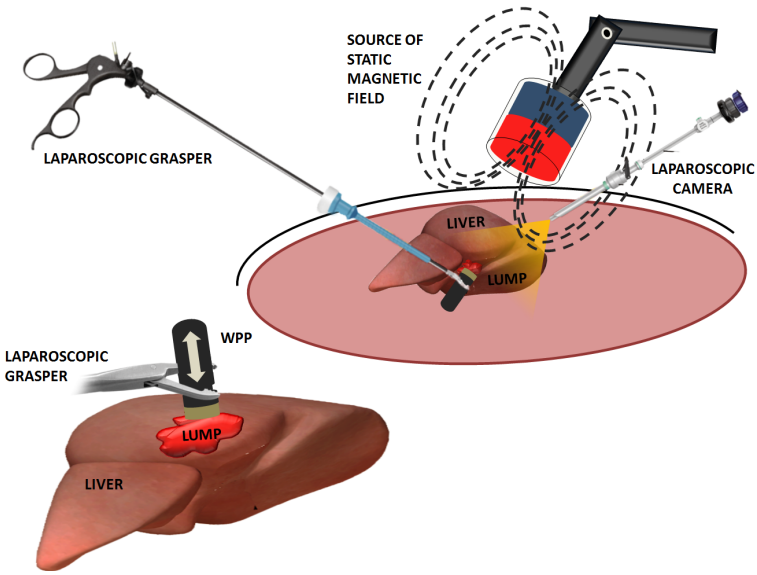

Figure IV.7: Principle of operation for wireless tissue palpation using a wireless palpation probe (WPP).

5 g or 0.049 N), while saturation occurred at $P_{SAT} = 5$ kPa (*i.e.,* considering the probing area, this is equivalent to 730 g or 7.16 N).

Real-time localization of the WPP serves two purposes. First, the position where indentation is taking place must be recorded in three degrees of freedom (DoF) in order to reconstruct the stiffness map. In this case, we assume the position $\mathbf{r}$ of each indentation to be coincident with WPP position as the indentation begins (*i.e.*, $\mathbf{r}_0$). A second goal for WPP tracking is to derive $\delta(\mathbf{r})$. In this case, real-time estimation of $\mathbf{r}$ and rotations of the WPP around x and y are required. Therefore, the WPP position and orientation in five DoF must be available in real-time. This is achieved by an on-board localization module, working in synergy with an external source of static magnetic field, as represented in Fig. IV.7. The on-board module consists of three orthogonally mounted magnetic field sensors and a triaxial accelerometer – used here as an inclinometer – that provides WPP rotations around x and y. The WPP position vector $\mathbf{r}$ is derived from the magnetic field sensor readings, as suggested in [35]. The average absolute localization errors were equal to 4.7 mm ($\pm$4.5 mm) for x, 4.1 mm ($\pm$5.8 mm) for y, and 4.5 mm ($\pm$2.2 mm) for z. The laparoscopic grasper increased the localization error to 9.8 mm ($\pm$5.1 mm) for x, 11.3 mm ($\pm$6.6 mm) for y, and 10.6 mm ($\pm$4.6 mm) for z. However, we observed that the contribution of the laparoscopic grasper does not vary substantially within the workspace, thus it can be assumed as a constant offset that factors out when reconstructing the stiffness map. The indentation depth average absolute error resulted in 0.68 mm ($\pm$0.44 mm).

The WPP prototype, represented in Fig. IV.8, has a cylindrical shape (15 mm in diameter, 60 mm in length, 9.5 g total mass) with a grasping site close to the pressure sensor head. The cylindrical plastic shell fabricated by rapid prototyping and it hosts a pressure sensing head, a localization module with a dedicated signal conditioning stage, a power regulation unit, a rechargeable battery, and a wireless microcontroller.

To estimate the ability of the WPP in detecting different local stiffnesses, two different synthetic tissue samples were fabricated combining two different ratios of liquid plastic and hardener (PVC Regular Liquid Plastic – Hardener, MF Manufacturing, USA – Sample 1: 1 to 10 ratio, resulting in an elastic modulus of 220 kPa; Sample 2: 1 to 2 ratio, resulting in an elastic module of 45 kPa). The local stiffnesses measured with the traditional indenter were equal to $E_1 = 2.12$ kPa/mm, $E_2 = 8.52$ kPa/mm, while the results obtained with the WPP were $E_{1WPP} = 2.02$ kPa/mm, $E_{2WPP} = 8.79$ kPa/mm. Experimental plots obtained from a single loading are represented in Fig. IV.6. Overall, the WPP was effective in detecting the local stiffness of different samples with an average relative error equal to 4.7% for sample 1 and 3% for sample 2.

The feasibility of wireless tissue palpation was then assessed *in vivo* on an anastetized porcine model. The primary measure of interest was to acquire a volumetric stiffness map of a segment of the liver where agar-gel was injected to simulate a hepatic tumor. The map acquired *in vivo* by wireless palpation was then compared with a stiffness map obtained *post-mortem* within 12 hours after the procedure using a standard uniaxial material tester.

The WPP was introduced in the abdominal cavity through one of the 12-mm trocar incisions before the placement of the port. The external source of magnetic field and the external transceiver were placed in the close vicinities of the right side of the animal, as represented in Fig. IV.9.B. The surgeon used a standard laparoscopic grasper to operate the WPP under endoscopic guidance (see Fig. IV.10). A lateral screen showed in real-time WPP position in three DoF, indentation pressure, and indentation depth (see Fig. IV.9.A).

Once the right segment of the liver was identified, the surgeon palpated the organ in different positions, always targeting at least 3 mm as the indentation depth. To prevent localization artifacts, the surgeon verified that the liver was not moving during palpation and that adequate support was provided by the rib cage and the surrounding organs. Tissue stiffness was acquired on a total of 30 different points on the liver surface. This required about 5 minutes. The local stiffness map, represented in Fig. IV.11, was then generated by the algorithm and displayed on the lateral screen, overlaying the current position of the WPP.

Immediately after euthanization, the liver was harvested from the animal for *ex vivo*

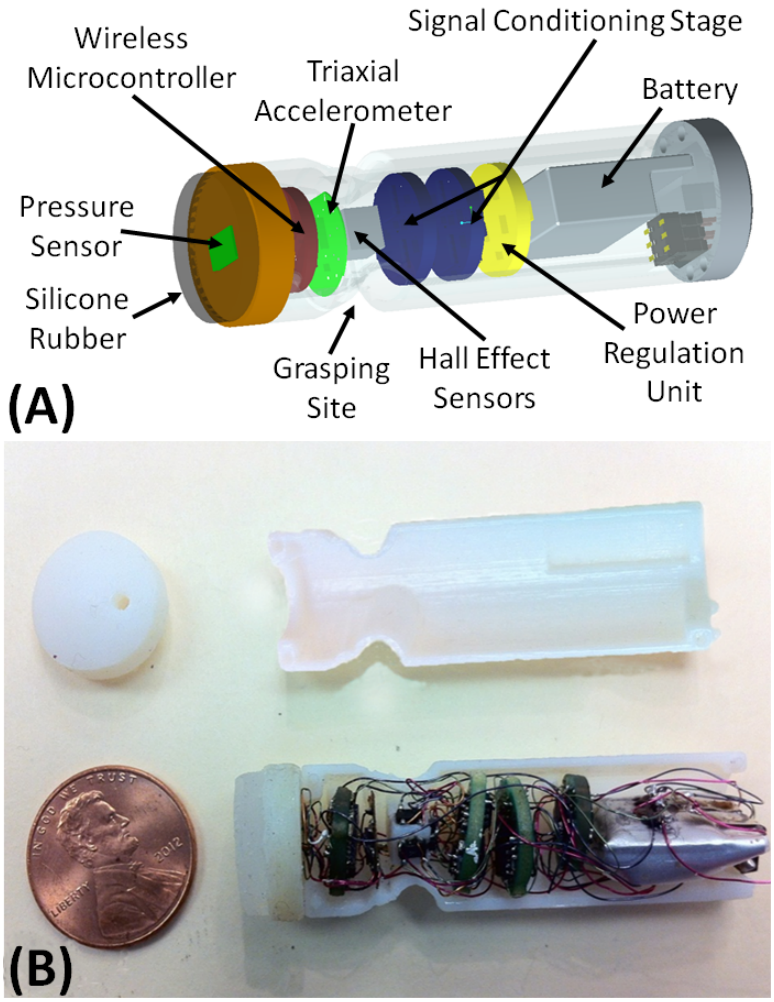

Figure IV.8: (A) Schematic view and (B) picture of the wireless palpation probe. The signal conditioning stage, the triaxial accelerometer, the power regulation unit, and the wireless microcontroller are mounted on separate printed circuit boards (PCB) with a diameter of 9.9 mm. In particular, the signal conditioning stage was separated into two boards due to PCB area constraints.

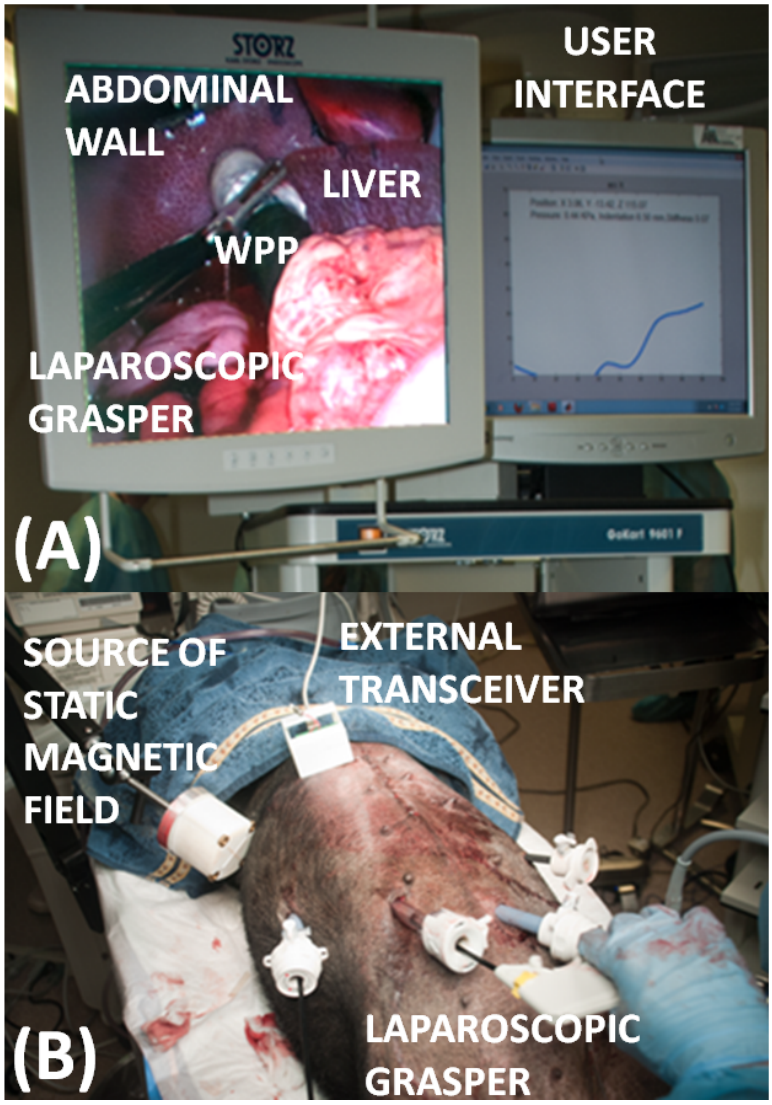

Figure IV.9: Picture of the surgical setup during the *in vivo* trial. (A) Snapshot of the laparoscopic camera view and the user interface during the creation of the volumetric stiffness map. (B) Picture of the surgical field.

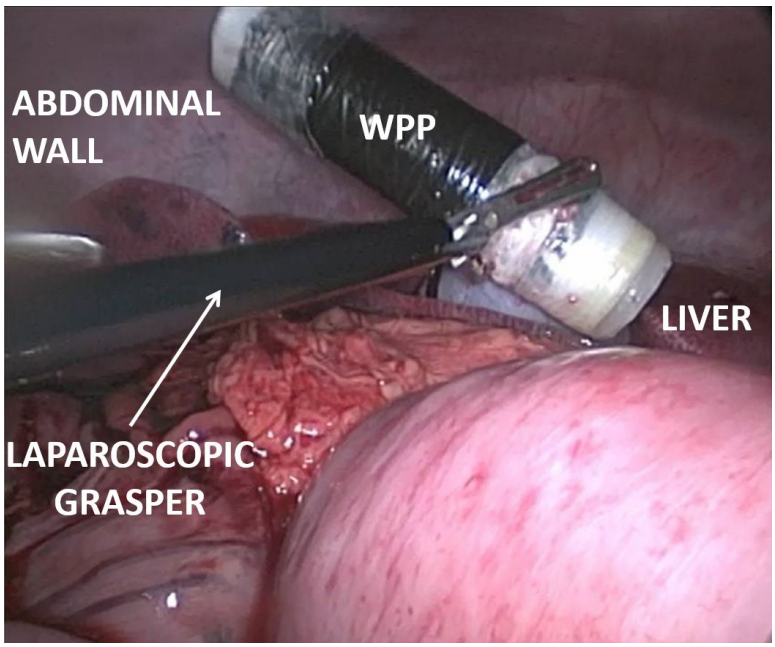

Figure IV.10: Laparoscopic view of the WPP operated by the surgeon through a laparoscopic grasper during *in vivo* trials.

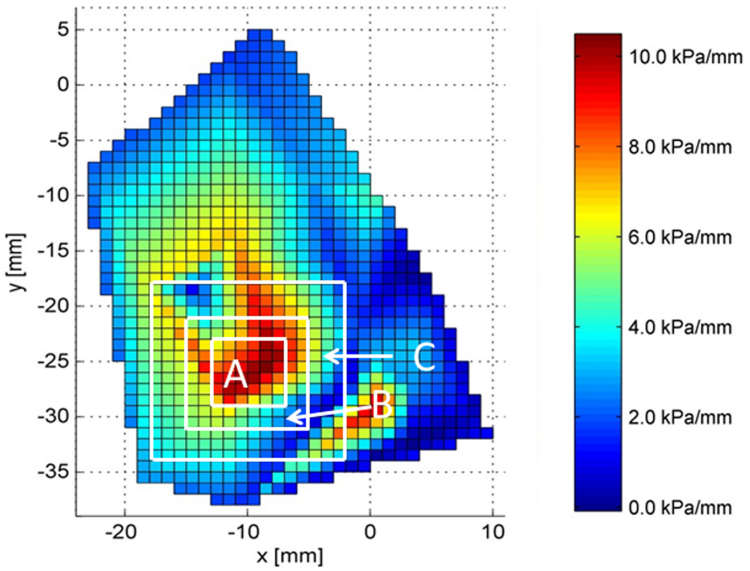

Figure IV.11: Local stiffness map acquired *in vivo* for a 6 cc agar gel lump injected into the liver. Since the surface of the liver was almost flat in the palpated region, a bidimensional projection of the map is shown. The local stiffness values inside areas A, B, and C were compared with the *ex vivo* map represented in Fig. IV.12.

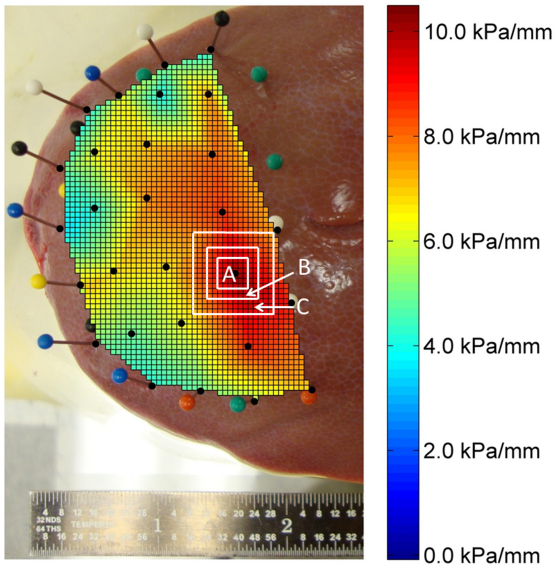

Figure IV.12: Stiffness map obtained with a standard uniaxial MTS, overlayed on the right lateral segment of the explanted porcine liver. The local stiffness values inside areas A, B, and C were compared with the *in vivo* map represented in Fig. IV.11.

palpation tests using a standard uniaxial material testing system (MTS) to create a comparable stiffness map. The force data were divided by the surface area of the cylindrical probe tip to obtain pressure. The local stiffness at each point was determined by computing the slope of a linear regression of the first 0.75 mm of the pressure-displacement curve. Force at depths larger than 0.75 mm were found to be too high due to the rigid platform that the liver was resting on and the relatively small liver thickness. This was not an issue *in vivo* as the liver was pressed against other organs or the rib cage. The two local stiffness maps were then compared with Matlab (grid area is equal to 1 mm^2 for both the maps). In particular, the maximum measured stiffness resulted in 10.0 kPa/mm with the MTS machine versus 10.8 kPa/mm with the WPP, corresponding to a 8% relative error. Then, the average pseudo stiffness of the three different areas A (36 mm^2), B (64 mm^2) and C (156 mm^2) centered on the maximum point were compared. Area A is a square sided 6 mm, area B is the frame with outer dimension 10 mm and inner dimension 6 mm, while the area C is the frame with outer dimension 16 mm and inner dimension 10 mm. The average stiffness was equal to $E_{A_{MTS}} = 9.64$ kPa/mm and $E_{A_{WPP}} = 8.87$ kPa/mm (average relative error 7.96%), $E_{B_{MTS}} = 9.20$ kPa/mm and $E_{B_{WPP}} = 6.58$ kPa/mm (average relative error 28.5%) and $E_{C_{MTS}} = 8.64$ kPa/mm and $E_{C_{WPP}} = 4.82$ kPa/mm (average relative error 44.2%).

As concerns the qualitative measures of interest, no instrument clashing was reported.

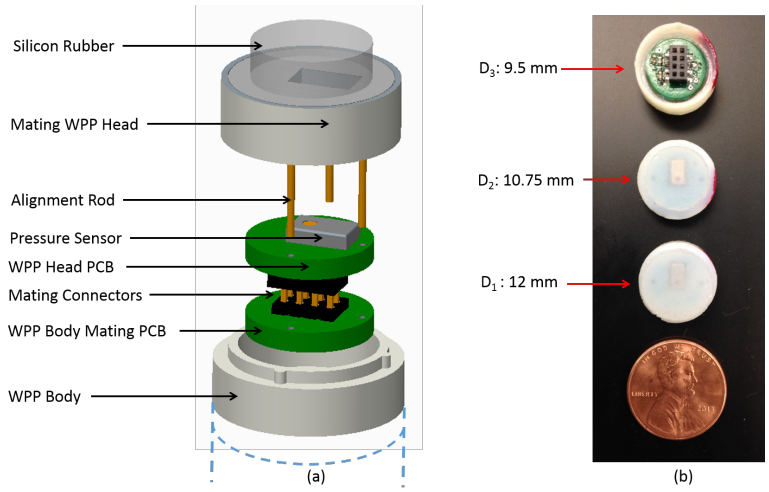

Figure IV.13: The WPP head explosion view (a), the fabricated heads of different diameters (b).

However, the length of the WPP limited the range of motion whenever the target of palpation was too close to the ribcage. The operator workload was minimal, since the surgeon was able to use a standard laparoscopic instrument to operate the WPP. Relevant learning occurred just at the beginning of the procedure, when the surgeon had to understand how strong to grasp the WPP to prevent slippage. This required about 20 minutes. After that, the surgeon was able to operate the WPP without losing the grip. The wireless link was always reliable, resulting in an average RSSI of -33.4 dBm with losses between 4.8% and 6.2% of the total packages. Battery operation was effective for the entire procedure.

IV.4 Wireless Tissue Palpation: characterization of the head probe to improve detection of tumors in soft tissue

In this chapter, we implemented a new calibration methodology to reduce the error introduced by the rubber nonlinearities on the pressure measurements, and thus reconstruct the measured pressure more accurately. The method was verified with different diameter heads fabricated according to a new design that allows for exchangeability and disposability of the WPP heads. Finally, we studied the effect of the mounted head diameter on the device's ability to detect different size lumps embedded into the silicone. Although this work used a specific probe (*i.e.*, the WPP), the contribution of the calibration procedure described in this paper can be generalized to any probing system in which silicone rubber is interposed between the target tissue and the mechanical sensor. For more details the reader is invited to check the publication [34]

After initial fabrication, the head was placed in a degassing oven and subjected to the

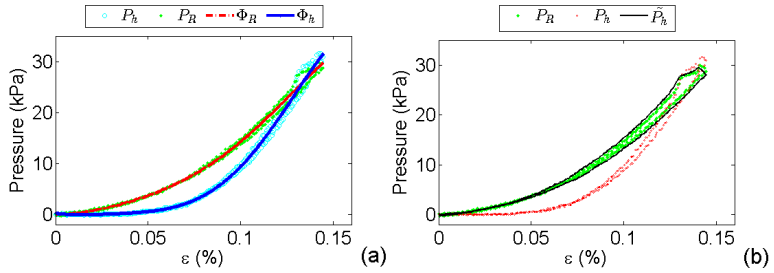

Figure IV.14: The raw pressure data, the reference pressure, and their numerical functions' interpolations (a), the raw and calibrated pressure data compared with the reference pressure P_R (b).

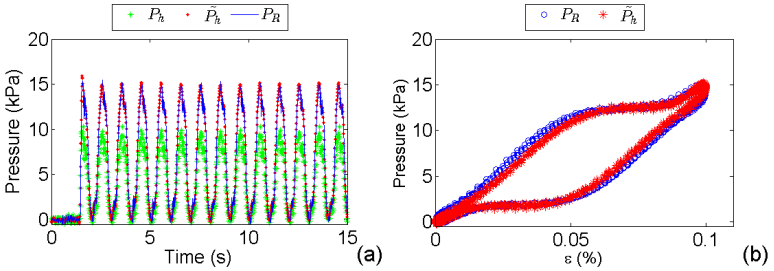

Figure IV.15: The WPP head is tested under a dynamic strain at a frequency of 1 Hz (a) The results of the stress-strain curve for the loading unloading cycles (b).

680 cmHg vacuum pressure for 2 min and 30 sec (any decrease in the amount of air remaining in the material was negligible after this amount of time). Three different diameters (*i.e.*, $d_1 = 12\ mm$, $d_2 = 10.75\ mm$, and $d_3 = 9.5\ mm$) of material on the head, shown in Fig. IV.13(b), were chosen to test the effects of the sensing surface area on the device's accuracy and precision during palpation. The quantity of material used for each diameter was 0.50 g, 0.45 g, and 0.40 g, respectively, within a tolerance of 0.01 g.

Fig.IV.14(b) shows the result of the calibration for the for the three different diameters.

Dynamic Assessment The calibration was then validated under a variable speed to verify that the dynamic stress over time did not perturb the system performance. For this purpose, the WPP was moved with a sinusoidal displacement at a frequency of 1 Hz on the rigid surface. This frequency is comparable to clinical usage, in which the WPP is grasped and pushed against tissue with a surgical grasper. For this trial, the silicone rubber was compressed from the contact point to 10 % of its thickness. The trial consisted of 14 loading/unloading cycles, as shown in Fig. IV.15(a), where the measurements for the reference pressure $P_R(t)$ and both the raw and calibrated sensor data are displayed. The

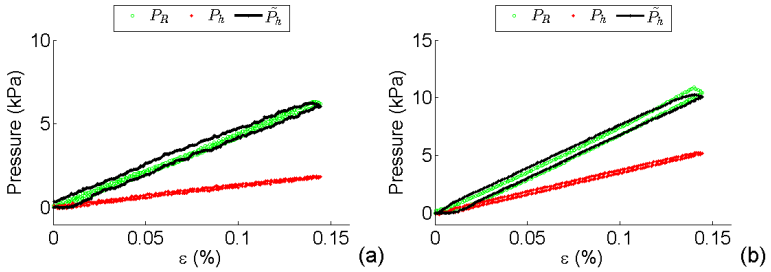

Figure IV.16: Palpation of the two different stiffness samples. Unfiltered sensor data (in red) and filtered sensor data (in black)

plot shows that the calibration is not affected by the dynamic response of 1 Hz load/unload cycles. In particular, using the data from the load/unload cycles, we can plot the value of the pressure as a function of the strain for each cycle, as represented in Fig IV.15(b). Based on the experimental results, we can conclude that though the silicone layer embedding the barometric pressure sensor introduces nonlinearities in the sensor response, these effects can be corrected, reducing the relative error of the reference pressure down to 2.1 %.

Tissue samples fabrication Finally, we tested the WPP ability to detect differing stiffnesses of two synthetic tissue samples. The samples were fabricated by combining two ratios of liquid plastic and hardener (PVC Regular Liquid Plastic and Regular Liquid Plastic Hardener, MF Manufacturing, USA Sample 1: 1 to 5 ratio, Sample 2: 1 to 3 ratio). The samples were 30 mm thick with lateral sides of 100 mm. As in the previous trials, the WPP was mounted on the distal side of the load cell to indent the samples. Five loading/unloading trials reaching an indentation depth of approximately 15 % of the sample thickness were performed for each tissue sample at a constant speed of 1 mm/s.

The stiffnesses measured by the load cell were equal to $E_1 = 43.65$ kPa and $E_2 = 76.63$ kPa, respectively, and for the WPP were $E_{1\ WPP} = 43.18$ kPa, $E_{2\ WPP} = 75.77$ kPa. Experimental plots obtained from a single loading are represented in Fig.IV.16. The results show that the WPP was effective in detecting the stiffness of different samples with an average relative error equal to 1.1 % for the first sample and 2.4 % for the second sample. Overall, with the introduced method the WPP is able to measure the stiffness of different samples with an average relative error below 2%.

Tissue abnormality detection by different diameter WPP heads

Tissue samples palpation validation

Bench experiments were conducted to investigate the efficacy of the WPP in identifying buried lumps of different sizes embedded into tissue phantoms at different depths. These

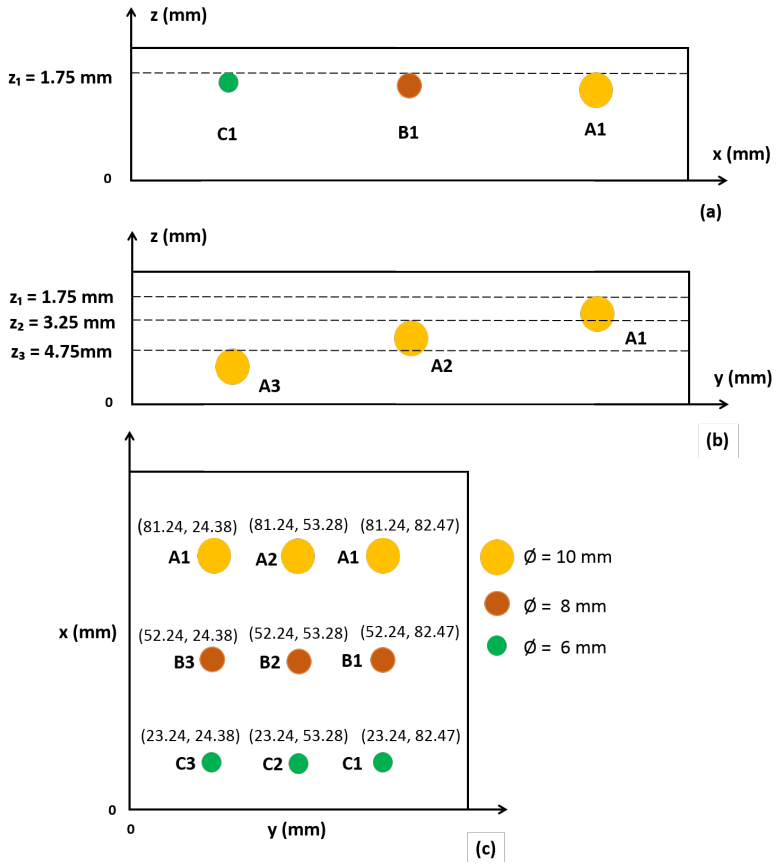

Figure IV.17: Dimensions of the fabricated phantoms with the embedded lump locations (a) and their relative depth (b).

phantoms, PH_1 and PH_2, were constructed similarly to [87] by combining different proportions of liquid plastics and hardener (PVC Regular Liquid Plastic and Regular Liquid Plastic Hardener, MF Manufacturing, USA PH_1: 1 to 5 ratio, PH_2: 1 to 4 ratio). The nine embedded spherical lumps were made using rapid prototyping (Material Elastic modulus 40-60 MPa). The dimensions of the phantoms and the lump locations, dimensions, and depths are shown in Fig. IV.17(a), Fig. IV.17(b) and Fig. IV.17(c).

Experimental Protocol

The elastic moduli of the two silicone phantoms were measured by conducting multiple indentation tests on the tumor-free areas, and resulted as $PH_1 = 42.78 \pm 1.45$ kPa and $PH_2 = 21.88 \pm 1.78$ kPa. These values are typical for human tissues, as reported in [67]. Uniaxial palpation was performed on both the phantoms with the WPP mounted on the end effector of the robotic manipulator and perpendicular to the phantom's surface. The manipulator was programmed to perform indentations along the phantoms' x-axes

at intervals equivalent to half of the head diameter. This created an r by c matrix of indentation points. The number of points for each row was set equal to the number of columns, creating an area of about 90 $\times$ 90 mm^2 to be indented with the three WPP diameters. The largest diameter head had $r_{d_1} = c_{d_1} = 16$ row and column combinations, resulting in 16×16 indentation points. The other two heads had $r_{d_2} = c_{d_2} = 18$, and $r_{d_3} = c_{d_3} = 20$ row and column numbers respectively. Placing the origin at the phantom corner, the first indentation point P_0, was set at $x = 25$ mm and y = 25 mm.

The phantom surface is not perfectly even, thus the contact point with the surface needs to be estimated for each of the indented points. Therefore, before the start of the palpation procedure, the standard deviation of the sensor measurements was calculated with no load applied. The WPP then approached the phantom surface from a distance of about 20 mm and a speed of 2 mm/s until the sensor pressure measurement exceeded three times its standard deviation. When this condition was verified, the manipulator z position was assumed to be in contact with the phantom surface. Then, the WPP indented the phantom at a speed of 1 mm/s until the programmed indentation depth was achieved. Motion in the opposite direction with the same speed was performed until the WPP returned to the depth of the contact point. Here, the probe was moved 20 mm up from the surface and then shifted along the phantoms x-axis to the next indentation point. This procedure was repeated c times (equal to the number of columns in the indentation matrix) before the manipulator shifted along the phantoms y-axis to begin a new path. The silicone phantoms were found to have an uneven surface with average surface height along their z-axes of 33 $\pm$ 0.57 mm and 33 $\pm$ 0.26 mm, respectively.

To evaluate the robustness and repeatability of the probe, indentation palpation trials were repeated five times for each of the different diameter heads with an indentation depth of 3 mm and 5 mm.

Data Analysis

After completion of the palpation experiments, pressure indentation maps of the two phantoms for the different head and indentation depth combinations were generated. Embedded lumps are stiffer than the surrounding silicone, and their location in the map is represented by a higher stiffness region (red). Figures IV.18(a) and (c) show the maps obtained from one of the trials by using d_1 mounted on the WPP to palpate PH_1. In this trial, the indentation pressure ranged from 4.75 kPa to 19.5 kPa for the 3 mm indentation depth, and from 19.9 kPa to 60.25 kPa for the 5 mm indentation depth. Figures IV.19(a) and (c) show the pressure map for PH_1, where the indentation pressure ranged from 1.8 kPa to 12.1 kPa for an indentation depth of 3 mm and from 3.4 kPa to 23.15 kPa for an indentation

Phantom 1						
Head Diameter	d_1		d_2		d_3	
Indentation Depth	$\delta = 3$	$\delta = 5$	$\delta = 3$	$\delta = 5$	$\delta = 3$	$\delta = 5$
Embedded Lump	A_1					
$S(mm^2)$	128	121	108	104	89	82
Error (x;y)		(1.7;1.2)		(0.5;1.9)		(1.6;1.5)
Embedded Lump	A_2					
$S(mm^2)$	98	102	97	94	78	85
Error (x;y)		(0.8;0.3)		(0.5;1.3)		(0.3;0.1)
Embedded Lump	A_3					
$S(mm^2)$	92	107	105	107	74	89
Error (x;y)		(1.7;0.1)		(0.4;3.2)		(1.3;3.2)
Embedded Lump	B_1					
$S(mm^2)$	71	74	63	69	54	61
Error (x;y)		(1.2;0.8)		(2.2;1.4)		(0.2;0.3)
Embedded Lump	B_2					
$S(mm^2)$	58	67	52	61	57	64
Error (x;y)		(1.5;1.1)		(1.2;1.5)		(1.4;2.2)
Embedded Lump	B_3					
$S(mm^2)$	51	65	54	57	58	60
Error (x;y)		(1.2;1.1)		(3.2;2.9)		(1.3;1.4)
Embedded Lump	C_1					
$S(mm^2)$	-	39	18	32	15	19
Error (x;y)		(1.0;1.2)		(1.3;1.2)		(2.4;2.1)
Embedded Lump	C_2					
$S(mm^2)$	-	-	-	35	-	31
Error (x;y)		(0.4;.2)		(1.5;1.2)		(0.3;1.4)
Embedded Lump	C_3					
$S(mm^2)$	-	-	-	-	-	22
Error (x;y)		(0.1;1.1)		(1.3;2.4)		(0.3;0.5)

Table IV.1: Position error and the resulting surface for the embedded spherical lumps is reported for Phantom 1.

depth of 5 mm. In both tissue phantoms, the measured stiffer values corresponded to the lumps larger and closer to the surface (*i.e.*, A_1).

To characterize the effectiveness of the different WPP heads in localizing the embedded lumps, a contour map of the indented surface was generated for all the trials. The plot consisted only of the regions where the indentation pressure exceeded a certain threshold, specifically, the sum of the minimum pressure measured by the map and 5 times the sensor standard deviation. Figures IV.18(b) and (d) and Figures IV.19(b) and (d) show the resulting contour maps for the same trials. Each individual palpation point is represented by a single point (shown in black), while the spherical embedded lumps are marked by dotted circles (shown in purple) of their actual size.

The effectiveness of the WPP in detecting different size lumps is reported in Table IV.1 and Table IV.2 for PH_1 and PH_2, respectively. These tables report the average errors for the trials between the stiffness peaks and the ground truth lumps' center locations

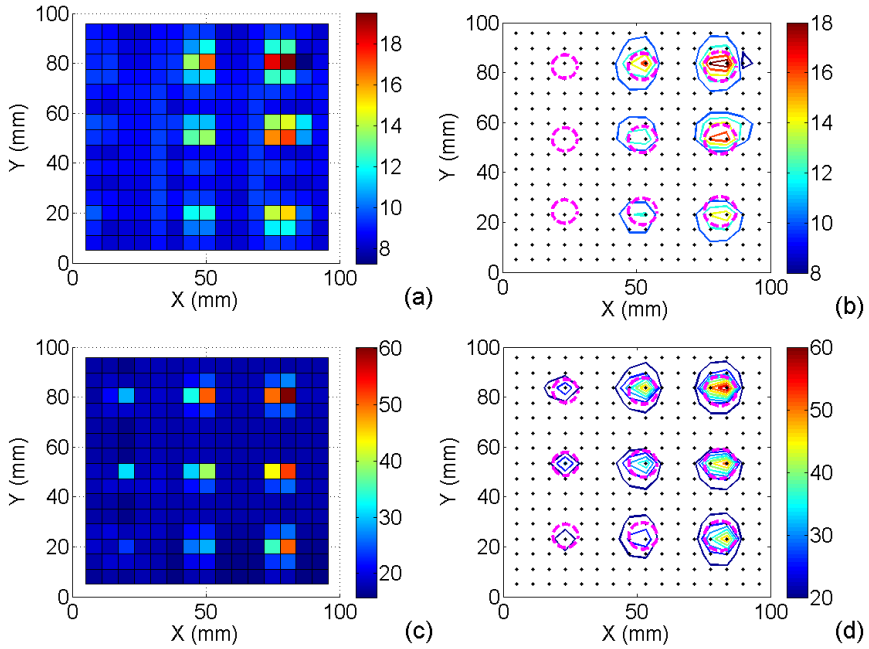

Figure IV.18: Pressure maps obtained respectively by palpating the hardest phantom, PH_1, with 3 mm (a) and 5 mm (b) indentation depth and the resulting contour maps (c) and (d) for the same indentation values.

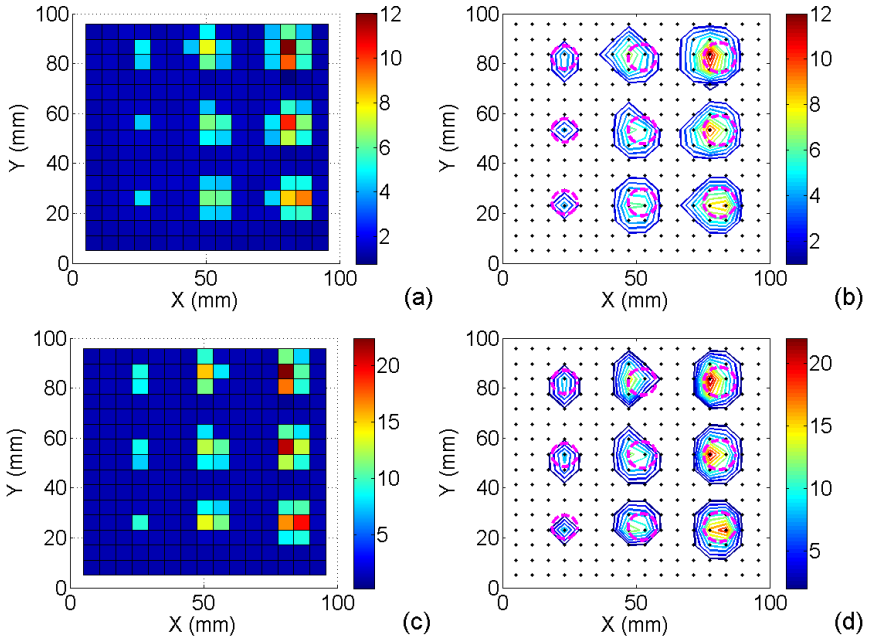

Figure IV.19: Pressure maps obtained respectively by palpating the softest phantom, PH_2, with 3 mm (a) and 5 mm (b) indentation depth and the resulting contour maps (c) and (d) for the same indentation values.

Phantom 2						
Head Diameter	d_1		d_2		d_3	
Indentation Depth	$\delta = 3$	$\delta = 5$	$\delta = 3$	$\delta = 5$	$\delta = 3$	$\delta = 5$
Embedded Lump	A_1					
$S(mm^2)$	187	203	187	192	95	82
Error (x;y)		(0.4;.9)		(1.5;2.5)		(1.4;2.3)
Embedded Lump	A_2					
$S(mm^2)$	184	177	168	153	82	78
Error (x;y)		(1.4;2.1)		(0.4;.3)		(0.7;.4)
Embedded Lump	A_3					
$S(mm^2)$	172	165	144	147	94	103
Error (x;y)		(.4;1.3)		(1.4;1.2)		(2.3;1.2)
Embedded Lump	B_1					
$S(mm^2)$	141	144	124	127	95	81
Error (x;y)		(2.1;1.2)		(2.9;1.4)		(0.1;1.3)
Embedded Lump	B_2					
$S(mm^2)$	147	154	121	132	87	74
Error (x;y)		(2.6;1.2)		(1.5;1.4)		(2.5;3.1)
Embedded Lump	B_3					
$S(mm^2)$	138	141	107	115	69	81
Error (x;y)		(1.5;2.4)		(0.5;2.1)		(2.5;1.2)
Embedded Lump	C_1					
$S(mm^2)$	42	45	32	41	19	29
Error (x;y)		(1.7;1.5)		(0.3;1.4)		(2.4;1.5)
Embedded Lump	C_2					
$S(mm^2)$	28	34	27	35	14	24
Error (x;y)		(3.1;2.4)		(0.5;1.7)		(3.2;1.7)
Embedded Lump	C_3					
$S(mm^2)$	25	32	19	33	17	21
Error (x;y)		(2.1;1.5)		(3.3;.4)		(2.3;0.7)

Table IV.2: Position error and the resulting surface for the embedded spherical lumps is reported for Phantom 2.

along with the average detected lump area for all the trials. Overall, for all trials on both phantoms, the average relative location error in detecting the lumps was equal to E_x=1.4 mm, E_y=1.2 mm when palpation was performed with the d_1 spatial resolution, E_x=1.4 mm, E_y=1.6 mm for d_2 spatial resolution, and E_x=1.5 mm, E_y=1.5 mm for d_3 spatial resolution. The average area detected for 10 mm lumps A_1, A_2, and A_3 resulted in an average surface of 144 mm^2 when palpation was performed with d_1 (average relative error equal to 82.28 %), 133 mm^2 for d_2 (average relative error equal to 68.35 %), and 85 mm^2 for d_3 (average relative error equal to 7.6 %). The 8 mm lumps B_1, B_2, and B_3 resulted in average surfaces of S_{d_1} = 104 mm^2 (average relative error 103 %), S_{d_2} = 90 mm^2 (average relative error 80.7 %), and S_{d_3} = 70 mm^2 (average relative error 40.5 %), respectively. Finally, the 6 mm lumps, C_1, C_2, and C_3, resulted in an average surface of S_{d_1} = 35 mm^2 (average relative error 55.4 %), S_{d_2} = 30 mm^2 (average relative error 39.9 %), and S_{d_3} = 21 mm^2 (average relative error 25.4 %), respectively. The resulting average resulting lump detection success rate was equal to 86 % for d_1, 92 % for d_2, and 94.4 % for d_3, and by increasing δ to 5 mm, all lumps were detected, regardless of the head's diameter. The results suggest that the number of visible embedded lumps in the map increases with indentation depth, δ. Furthermore, the resulting evidence shows that lumps were detected more easily on the softest of the two phantoms (*i.e.*, PH_2). In fact, the trials on PH_1 confirmed that lumps C_2 and C_3 were never detected for the 3 mm indentation depth. Trials on PH_2, on the other hand, resulted on a 100 % detection rate for all lumps with both indentation depths.

The experiments suggest that the smallest diameter head (*i.e* d_3) is more effective in estimating the lump areas when compared to the larger diameter heads. The spatial distribution of the indentation points in our experimental set-up in fact depended on the actual diameter of the probe. The larger the diameter of the head, the larger the indentation point spacing, as well as the sensing area. Therefore, when palpating nearby the lumps at points along x and y, some lumps were perceived by the bigger heads, causing wider surface error. To overcome this problem and reduce the errors, a smaller spatial resolution can be adopted when indenting.

Palpation trials were thus repeated on PH_2 with d_1 and d_2 mounted on the WPP. For both heads, the indentation points were changed assuming palpation was performed with d_3 mounted, thus resulting in a smaller spatial resolution. Figure IV.20 shows the trials performed with d_1 on PH_1 for both the indentation depth. The average area detected by the two heads for the 10 mm lumps (A_1, A_2, and A_3) resulted in surface of 106 mm^2 (average relative error 36 %). The 8 mm lumps (B_1, B_2, and B_3) resulted in an average surface of 60.3 mm^2 (average relative error 20.4 %) and finally the 6 mm lumps, (C_1, C_2,

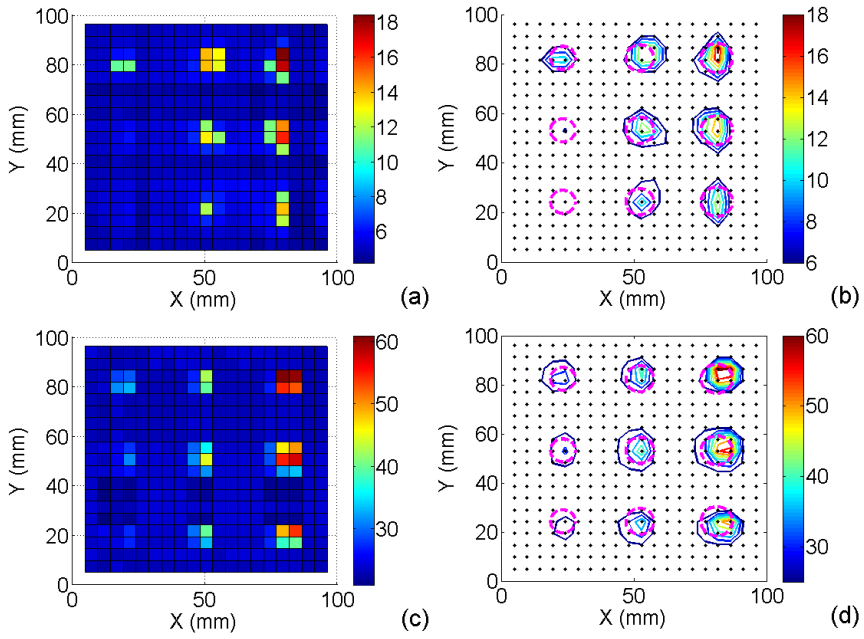

Figure IV.20: Pressure maps obtained respectively by palpating the hardest phantom with 3 mm (a) and 5 mm (b) indentation depth with the smaller spatial resolution. The resulting contour maps for the same indentation values: 3 mm (c) and 5 mm (d).

and C_3), had an average surface of 31.4 mm^2 (average relative error 12 %). For both the head diameters, the resulting maps showed an average resulting lump detection rate equal to 94.4 % and the same ability to detect lumps as the smaller head. These results suggest that better lump detection can be achieved with the combination of greater indentation depth and smaller spatial resolution.

The palpation procedure performed took respectively 8 min and 26 s ± 1 s for d_1, 10 min and 41 s ± 1 s for d_2, and 13 min and 21 s ± 1 s for d_3 with the probe moved by the robotic manipulator. If we consider the case of a MIS procedure, where the probe is manipulated by a surgical grasper and the surgeon is assumed to palpate at a frequency of 0.5 Hz, the same area of the phantoms used in the bench-top trials would be covered in less than 10 m. This amount of time is a reasonable expectation for MIS surgery and is completely within the probe battery capacity.

Results

The new calibration methodology was implemented for the WPP to reduce the error introduced by rubber nonlinearities on pressure measurements, thus enabling reconstruction of the measured pressure from the silicone rubber indentation. The method was validated with different diameter heads fabricated according to a new design that allows for exchangeability

and disposability of the pressure sensing element. The bench-top experiments showed good repeatability and accuracy in quantitative measurements of different elastic moduli with a relative error below 3 %, regardless of the mounted head diameter. Furthermore, the device proved its ability to effectively detect different size lumps embedded into a silicone tissue simulator: the diameter of the head does not affect the device's ability in lump detection and there is no need for preoperative surface registration. Trials with the greater indentation depth demonstrated how buried lumps can be effectively detected without exceeding 6 N, a force value which can lead to tissue damage [88].

The identification of precise margins for curative resection, overall, showed an overestimated malignant area especially when the indentation points are not close to each other. However, during tissue resections, a clearance of at least 1 cm is recommended to prevent positive tumors margins [89]. As such, the overestimated area does not comport any disadvantage to the WPP usability in MIS, and it can considerably aid surgeons in procedures that involve the accurate targeting of malignant areas, both near the surface and further buried.

IV.5 *Ex-vivo* trials on human prostates

This sections describes the results from performing tissue palpation on *ex-vivo* human prostates. Using the same procedure described in section IV.3 and by injecting agar gel into human prostate we simulated harder lumps into it. As is shown in Fig. IV.21(a) we injected the gel in three different regions. After palpating the prostate, for about 1 minute with the device as represented in Fig. IV.21 (b), all three tumors were correctly visualized on the stiffness map with a spatial resolution of 3 mm. The planar dimensions for each tumor measured by the proposed method were 9×6 mm^2 for α, 18x×15 mm^2 for β, and 6×6 mm^2 for γ. If compared to the planar dimensions of each tumor, the localization error was 9±9 mm^2. The measured stiffness range was 0.9±0.2 kPa for lump α, 0.850.27 kPa for lump β, and 0.79±0.21 kPa for lump γ. Surrounding tissue stiffness was 0.07±0.04 kPa for regions without features, increasing to 0.35±0.2 kPa in case of buried structures such as the urethra. In the human cadaveric prostate, the probe accurately measured sub-surface tissue densities and relative positions, which can be represented on 3-dimensional mapping. This has the potential to provide important, real-time information of tumor location which may allow for more precise surgical dissection of the prostate to ensure negative surgical margins and improved outcome

IV.6 Conclusions

This chapter presented an MCR to restore tactile feedback in MIS through wireless tissue palpation. Wireless tissue palpation can localize tumor margins intraoperatively by creating

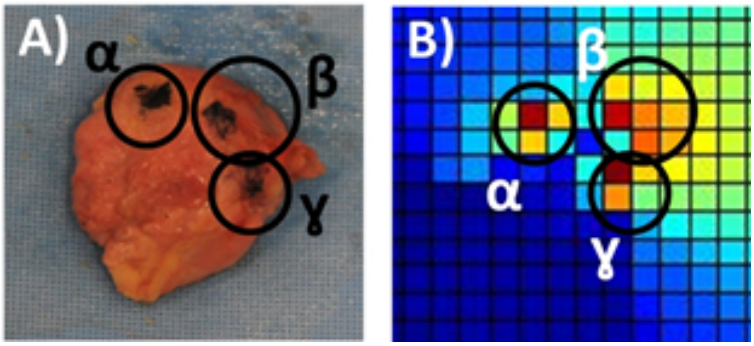

Figure IV.21: (a) Cadaveric prostate with identified target lesions. (b) Simulated map of corresponding lesions

a stiffness distribution map in real-time. The MCR is manipulated directly by the surgeon through a standard grasper, thus improving autonomy, precision, and maneuverability. Wireless operation effectively prevents instrument clashing and removes from the need of a dedicated access port. Preliminary *in vivo* results showed the feasibility of acquiring a stiffness map during a minimally invasive procedure. In the future, this map can be used to guide liver resection without sacrificing excess normal tissue and preventing postoperative organ failure.

The identification of precise margins for curative resection, overall, showed an overestimated malignant area especially when the indentation points are not close to each other. However, during tissue resections, a clearance of at least 1 cm is recommended to prevent positive tumors margins [89]. As such, the overestimated area does not comport any disadvantage to the WPP usability in MIS, and it can considerably aid surgeons in procedures that involve the accurate targeting of malignant areas, both near the surface and further buried.

IV.7 Discussion

While the indentation pressure is acquired by a sensor mounted on board, the position and the indentation depth measurements rely on an external source of static magnetic field. This imposes a constraint on the workspace, since magnetic field strength drops exponentially with distance. With the proposed platform, the workspace is a cylinder with a diameter of 35 cm and a length of 35 cm, centered on the source of static magnetic field. Considering that the abdominal wall thickness for severely obese patients (Body Mass Index $\leq$ 40 kg/m^2) is usually below 4 cm [90], the proposed platform is easily applicable to the vast majority of patients undergoing abdominal surgery. Nevertheless, if a larger workspace is required, either the source of magnetic field or the on-board magnetic field

sensors can be adapted to meet the desired requirements. As previously mentioned, motion of the organ during the creation of the map or poor background support for the tissue may result in localization artifacts. If this occurs, the surgeon needs to restart the acquisition of stiffness values. This issue is common for intraoperative palpation and can be addressed with appropriate surgical planning.

The current embedded sensor package dimensions do not guarantee the fabrication of WPP head diameters smaller than 8 mm, limiting the maximum number of embedded sensors. Thus, a smaller package pressure sensor can be integrated (*e.g.*, BMP180, Bosh, USA) or triaxial force sensors can be explored as valid alternatives [91, 92]. The current calibration methodology requires the use of a reference force sensor to characterize the embedded sensor response. Analytical characterization of the silicone rubber's mechanical properties and geometry can substitute the calibration procedure by implementing techniques such as those presented in [93], to improve the sensor's spatial resolution and its ability to detect buried structures and further reduce the area of resected healthy tissue.

Chapter V

APPLICABILITY OF THE MODULAR ARCHITECTURE: OTHER EXAMPLES

In this chapter we present four different applications that have been developed with the architecture presented in this dissertation. While the first three devices are MCRs the fourth application demonstrates how this architecture can be successfully applied to other applications not related to the field of MCRs.

V.1 Real-Time Pose Detection for Magnetic Medical Devices

Remote manipulation of capsule endoscopes has the potential to extend the reach of WCE to other GI districts, allowing the physician to have direct control of the camera viewpoints. In [35] and a novel approach to detect in real-time the 6-DOF pose of a magnetic capsule endoscope. The proposed method takes advantage of the external magnetic field generated for manipulation, allowing for actuation and localization at the same time. As regards power consumption, a single 5 ms loop of data acquisition and wireless transmission drains an average of 33.3 mA with a peak of 41.6 mA. This translates in a battery lifetime of about 90 minutes when the device is in active mode. Average current consumption drops down to 2 mA in low power mode. The data synchronization between the device and the external transceiver was tested in open air to estimate the robustness of the protocol. The firmware was ran for 36 consecutive hours without failures and was then stopped. The results included a package loss below 2% and an average RSSI of -13.5 dBm at a distance of 2 m between the device and the external trans-receiver. Complete loss of communication occurs as the RSSI drops below -88 dBm.

V.2 Measurement of Resistant Properties in the GI tract

The order of magnitude of the resistant force that must be exceeded in order to move a WCE in the GI tract is an interesting parameter for the MCR research community. In [36], we designed an MCR based to measure this parameter in an *in vivo* porcine model. In this case, the MCR, shown with his can in Fig. V.1, was magnetically coupled with an external permanent magnet and was able to acquire inertial and magnetic field measurements to determine in real-time its motion profile (i.e., position, velocity and acceleration) and the inter-magnetic force.

The MCR embedded a custom analogue force and motion-sensing module, integrating six Hall effect sensors and a 3DA module. The master module acquired the Hall effect sensor readings with the embedded ADC, and communicated with the 3DA module via the

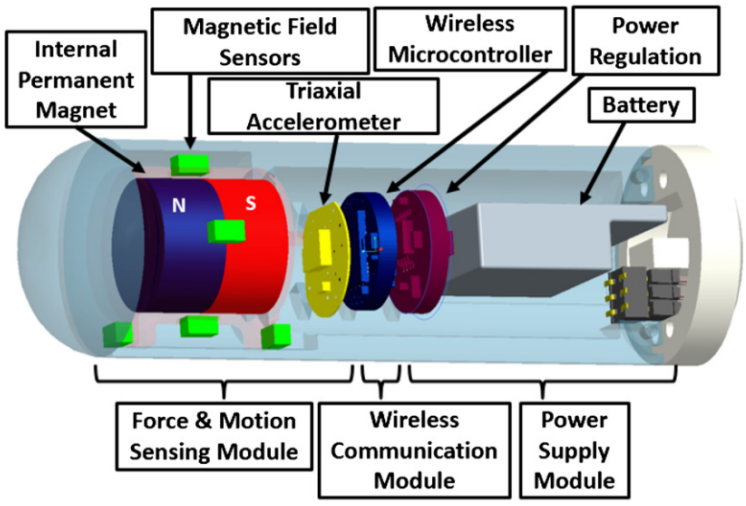

Figure V.1: The CAD of the MCR to measure the resistant properties in the GI tract.

SPI interface. Sensor data were bundled for wireless transmission every 4.4 ms in a 32-byte package. The refresh rate at the workstation was 6 ms. To save power, the MCR sensing front-end was operated in low power mode whenever data acquisition was not required, thus achieving a current consumption of 400μA. This increased up to 20 mA during data acquisition, and to 48 mA for each payload transmission. The battery lifetime was 75 minutes. Thanks to the reliability of the wireless communication and of the hardware, the developed MCR was able to operate for 75 minutes and we performed more than 50 measurements during the procedure. Fig. V.2(A) shows the insertion of the capsule into the colon then, as represented in V.2(B), the device was dragged with the external permanent magnet.

V.3 A magnetic drug delivery capsule based on a coil actuation mechanism

Referring to Fig. V.3(a) where the principle of operation of the device is presented, the MDDC body consists of two main parts magnetically coupled: the capsule body and the drug chamber in order to prevent the drug to be delivered. Three pairs of permanent axially magnetized NdFeB N-52 permanent magnets (h=2.54 mm, d = 3.175 mm) produce the force, FM, which holds the drug chamber together with the body. When a drug release is triggered, as shown in Fig.V.3(b), the current, IC, flowing through the coil generates the force FC which repels the permanent magnet pair one from the other and consequently, the drug inside the chamber is released.

Fig. V.4 shows a design of the MDDC prototype, while its main specifications are listed in Table V.1. The MDDC can be organized in three main units: the drug chamber, the

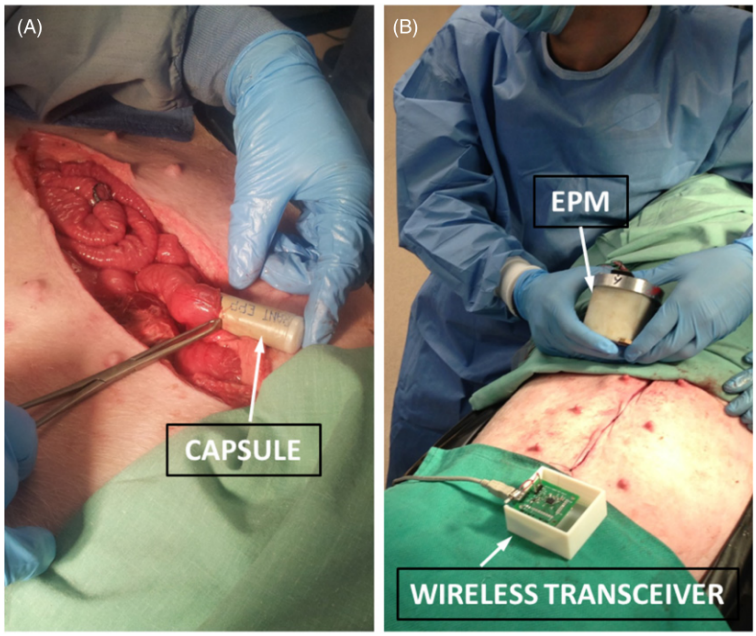

Figure V.2: Photograph of the operative setup during the *in vivo* trial. (A) The MCR being introduced in the porcine large intestinal. (B)The surgical field during the measurements

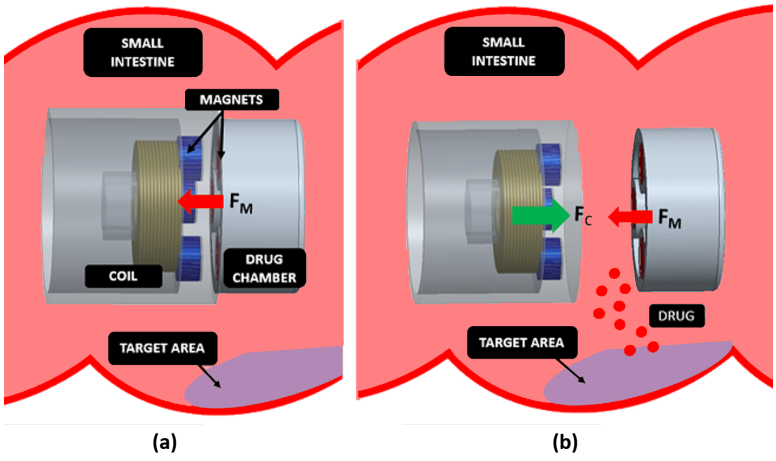

Figure V.3: Principle of operation of the Magnetic drug delivery capsule: (a) the drugs is kept in the chamber by the magnetic force FM, until the coil delivery mechanism is wirelessly triggered (b).

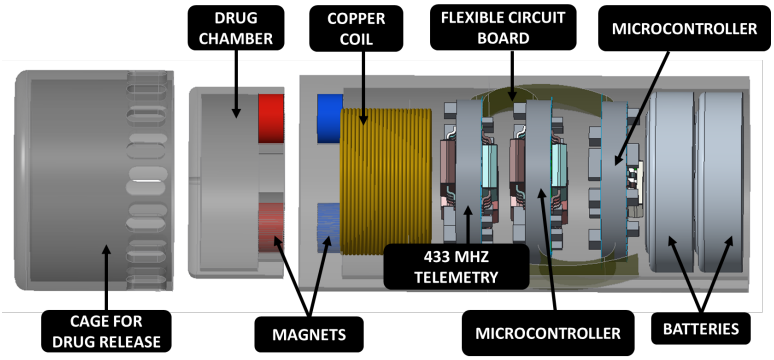

Figure V.4: CAD model of the MDCC prototype

release mechanism, and the embedded electronic circuit. The embedded electronics consists of a flexible circuit which hosts a microprocessor, a 433 MHz radio transceiver, and the circuitry to drive the coil, while power is provided by two coin batteries (389, Energizer). In particular, in order to generate enough current to drive the coil such that is able to actuate the delivery mechanism, the 3 V from the batteries is stepped up to 5 V. The coil (ID 5 mm, OD 8.37 mm, h =2.80 mm) consists of a copper insulated wire (d = 0.1 mm, R = 102 $\pm$ 1 ω). Consequently, the driving current flowing through the coil results in 48.8 $\pm$ 1 mA, and the resulting magnetic field is equal to 2.2 mT which generates a force equal to 0.8 N, which overcomes the force FM. The MDDC has been fabricated with 3D rapid prototyping (Object 3D), and it has a length of 35 mm and a diameter of 13 mm.

Table V.1: The MDCC prototype specifications.

Capsule Volume	3958.41 mm^3
Activation Time	1 ms
Power Source	20 mAh lithium battery
Telemetry	433 MHz
Therapy Delivered	Acetylsalicylic acid, Carbopol 980
Drug reservoir Volume	0.447 mL

Fig. V.5 shows a picture of the MDDC drug releasing mechanism and the unfolded flexible. The research so far has been focused in the design and dimension of the mechanism, while future works aim to characterize the delivery mechanism electro-mechanical properties as well as to implement the user interface.

V.4 Design of a sensorized cane for monitoring walking anomalies

Outside of the MCR field, a sensorized wireless cane was implemented with the proposed architecture. The electronics architecture of the instrumented cane is described in

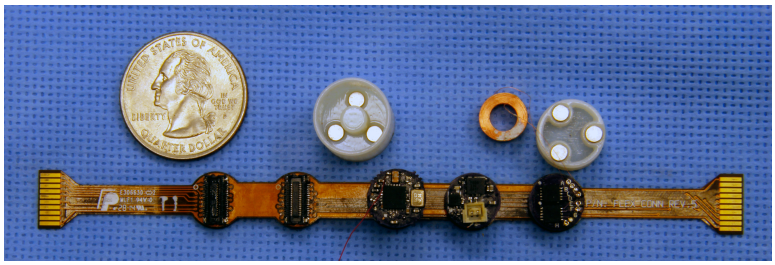

Figure V.5: The MDCC prototype before of being fold inside the shell

Fig V.6(a). This architecture consists of six primary modules [27]: a battery, a power management unit, a wireless microcontroller, two separate 9 DOF inertial measurement units (IMU) located in the cane handle and in the base, respectively, and an eight-channel analog to digital converter (ADC) to acquire force information from the FSRs. Our instrumentation design used two IMUs to detect linear acceleration at the two extreme endpoints of the cane. Two points were chosen because the pattern of acceleration is different at those positions depending on the current phase of walking. Seven FSRs were used on the handle because that amount provided adequate surface area coverage based on observations of several individuals handling of the device. With the exception of the FSRs and the IMU located in the base, all of the electronic modules were assembled into a plastic, semi-cylindrical shell fabricated by rapid prototyping (OBJET 30, Objet Geometries Ltd, USA).

The shell was shaped to easily fit the cane handle with a diameter of 14 mm, a height of 14 mm and a length of 35 mm. Fig. 2 shows the embedded components in the cylinder. Each of the modules consisted of a separate printed circuit board (PCB) each with a diameter of 9.8 mm and a thickness of 1.6 mm. All the modules were connected by soldering wires between their easily accessible pads. The power manager embedded a low-dropout voltage regulator (TPS73xx, Texas Instruments, USA), and an operational amplifier (ADS8617, Analog Devices, USA) to provide a buffered supply to the FSRs independently of the regulator. This module thus generated the 3.3 V needed for all of the modules. Both the 9 DOF inertial sensors (LSM9DS0, STMicroelectronics, Switzerland) and the eight channel ADC (AD7689, Analog Devices, USA) were controlled by a wireless microcontroller (CC2530, Texas Instrument, USA) through the serial peripheral interface (SPI) at a clock frequency of 1 Mbit/s. The two inertial sensors were configured to measure accelerations in a range of ± 4 g, angular velocities of 450 degrees per second (dps) and a magnetic field in a range of 2 gauss (G) with resolutions of 61 g, 7.5 mdps and 61 G, respectively. The cylinder provides a second connector to access the microcontroller pins to easily debug and

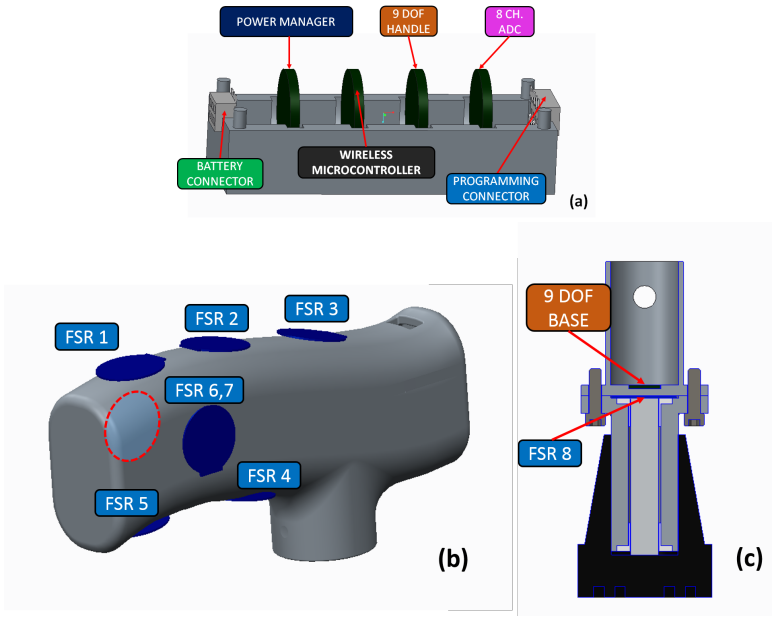

Figure V.6: The drawing prototype of the sensorized cane.

reprogram the canes main application. The FSRs (FSR 402, Interlink Electronics, USA) were mounted on both the cane handle and base as shown in Fig. 3 (a) and Fig. 3 (b), respectively.

The FSRs measured force with a sensitivity range of 0.2 N to 20 N. All of the FSR output signals were acquired by the 16 bit ADC which results in a resolution of 50.3 μV equal to 1500 μN. The electronic components of the base module were connected through the body of the cane to the handle with 1.2 m wire to allow adjustment of the cane length. Of the various power supply alternatives that we designed for, we chose two separate 100 mAh, 3.7 V rechargeable LiPo batteries (Shenzhen Hondark, Electronics Co., Ltd., China, 12 mm $\times$ 15 mm $\times$ 3 mm in size) which were connected in parallel and used as the onboard power supply source. The prototype of the cane is represented in Fig. V.7(a) while Fig. V.7(b)shows the real time plot of the sensed data from the user interface.

V.5 Discussion

In this chapter we have presented four different applications where this architecture was applied to foster the prototyping process of embedded systems, and not necessary MCRs. It is worth to mention that for all these works, the prototyping time was indeed shorten up of less then 2 months and all these works have been published in peer reviewed journals. Although the final prototypes are not optimized in size compared with a custom solution

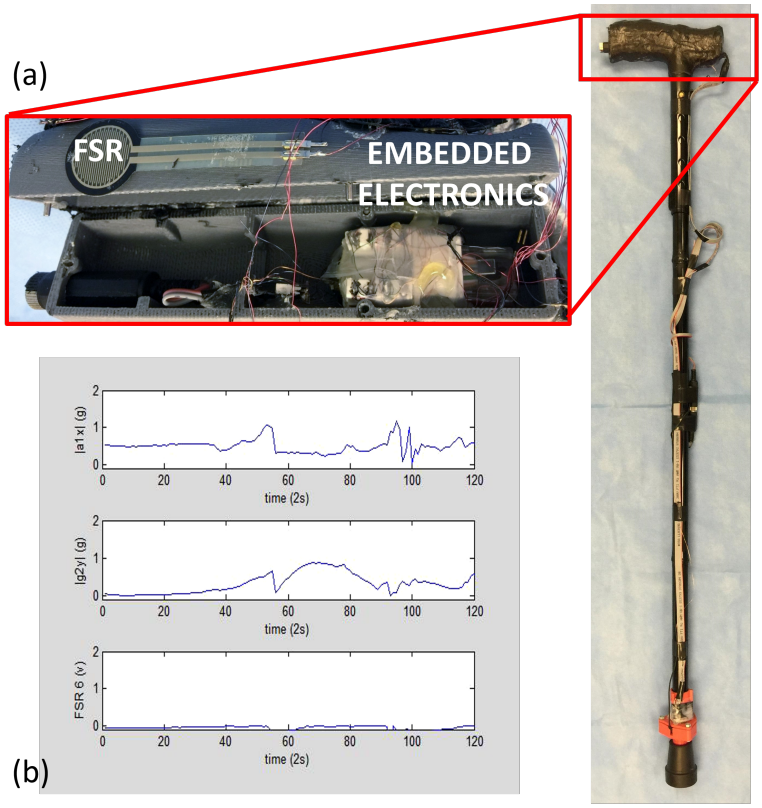

Figure V.7: (a) The cane prototype, the zoom shows the details of the handle where all the electronic has been mounted. (b) Real time data plot of the sensed data.

their final dimension are still comparable with the state of the art being able to led to scientific contributions.

Chapter VI

CONCLUSIONS

VI.1 Summary

The use of robotic systems in surgical procedures has increased steadily with the design of customized medical robots. In the near future, MCRs, smart capsules that leverage extreme miniaturization, have the potential to revolutionize healthcare by providing advanced diagnostics, biopsy collection, cancer removal and drug delivery functionalities out of reach of other robotic platforms. MCRs target different sites of the human body and they utilize various locomotion techniques, and integrate a diversity of sensors and actuators. However their design development requires significant skills and efforts in the prototyping, programming, debugging and miniaturizing of the device as well the expensive and time consuming practice of developing custom circuits and mechanical enclosures.

Because there are no hardware and software development platform for MCRs, researchers groups are usually forced to create their own MCRs from the ground up. This amounts to a duplication of efforts by different research groups, which could be better applied to the innovation of MCR with a platform that can shorten up their development time. **This doctoral dissertation proposed** a modular architecture to enable rapid prototyping of MCRs which can address the aforementioned technological gaps. The architecture consists of both hardware and software for a systematic approach to designing pill-size medical devices. Different variants of MCR to prove its performances and usability have been developed and included in this dissertation.

In Chapter II we described the architecture hardware and software components. Firstly, we defined the MCR requirements all the hardware modules are here described then each miniature module is described with its distinct functionality: wireless communication, powering, digital or analogue sensing, actuation, vision and illumination. Then, the three-layer stack of the architecture are presented. The low power operation, safety and reliability of wireless communication were experimentally assessed via *in vitro* and *in vivo* trials.

In Chapter III we discussed the further development of the architecture: the limitations have been here addressed by introducing a flexible backbone with connectors for an easily module exchangeability. The time to assembly an emblyMCR is shorten up and developers are not anymore required to solder. Finally we presented a TinyOS based MCR application

to demonstrate how this operative system can be used to program a device and perform typical MCR tasks.

Chapter IV presented the research outcomes of a Wireless Tissue Palpation probe, an MCR developed with the proposed architecture aiming to restore tissue palpation in MIS. We presented the feasibility of wireless tissue palpation on a single degree of freedom with via *in vitro* and *in vivo* trials. Then, the device has been further improved by embedding a tactile sensor on the tip embedded in silicone rubber as well as a 5 DOFs magnetic localization. *In vivo* trials on a porcine model assessed the ability of the device to detect a stiffer lesion created by injecting an agar gelatine into the liver. In the same chapter we presented the characterization of the silicon rubber response to improve the device ability to measure tissue stiffness. With the developed methods the device accuracy in measuring tissue stiffness resulted in an error below 5% when compared with a standard indenter. Different materials and head diameters have been characterized when mounted on the device to assess the best combination (material / head diameter) which detect lumps into the tissue. Finally Wireless Tissue Palpation (WTP) probe was used in *ex vivo* trials on human prostate and was able to successfully detect stiffer regions embedded inside regions.

In Chapter V we discussed the applicability of the proposed modular architecture to the field of MCR by presenting applications where the presented architecture was successfully adopted. In details, we presented MCRs to enable magnetic localization, to measure the resistant properties of the GI tract, and to release a drug in the GI tract. All these devices have been used intensively in both *in vitro* and *in vivo* trials leading to scientific journal publications. Finally the architecture was adopted an application outside of the MCR field consisting on a sensorized walking cane for gait recognition.

VI.2 Discussion and Future Works

This doctoral dissertation lays the foundation for the creation of an open source environment to enable rapid prototyping of MCR. The designer, regardless of his/her level of experience, will be able to focus on selecting pre-designed modules and programming the MCR to fulfill a specific task, rather than designing, fabricating, and connecting together miniature electronic boards. Furthermore, this approach can be applied to adjacent segments of medical technology, such as wearable monitoring systems and implantable healthcare devices were low power and miniaturized embedded systems are required. This architecture goes in the direction of creating an extensible library of hardware and software modules.The MCRs presented along side with this work would have required more development time if not implemented with the current architecture modules. The architecture demonstrated how it is possible to speed up the time-to-prototype, reducing the gap from

concept to experimentation. In addition the prototyping costs are reduced without the need for the developers to build custom circuitry.

This works complements the previous work in in addressing the common requirements of MCRs [61] with a complete design environment to build MCRs. Table VI.1 clearly shows the flexibility and the potential impact of the proposed approach to the field of MCRs.

Regarding the hardware, future work will aim to extend the library to include additional microprocessors, sensor and actuator modules, and wireless transceivers implementing different communication protocols and carrier frequencies (e.g. Low Power Bluetooth). In particular, the authors are exploring to extend the proposed platform to ARM Cortex microprocessors (e.g. the CC2650 from Texas Instruments). This module consists of a 2.4 GHz radio and a high performance ARM CPU, which will further reduce the folded capsule size. Other devices that integrate similar CPUs and other wireless communication protocols will be made available in the future.

On the software side, the application of TinyOS and the corresponding web-based design environment was a significant step towards developing reusable software components and composing embedded applications on resource constrained hardware platforms. However, the scope of the visual representation is limited to the static structure of software artifacts: *temporal behavior, energy and resource consumption and hardware dependencies* are hidden or implicit in the model. Providing analysis, validation and verification tools in these domains require more detailed, multifaceted models to be built. However, continuous refinement of the visual language is one of the strengths of the underlying configurable framework.

As part of our ongoing efforts, this work lays its fundamental to a state machine-based representation for the module components where designers can easily reason about potential application states and valid transitions with corresponding triggering events. This feature will help the designers to develop and modify their applications rapidly and will provide a high-level view of the application's logic in one place. Currently, the same information is hidden across several functions and is spread over multiple source files. Moreover, we are developing a higher level modeling abstraction, where instead of building from fine-grained TinyOS components, an MCR application is created by selecting and configuring a handful of composite *features*, such as wireless communication, imaging, self-propelled movement, or self-localization. Such larger design partitions include pre-built templates of TinyOS components, optional surrogate simulation models, hardware dependencies (concrete hardware modules and their placement on the flexible circuit board), power profile and application-level interfaces. Our goal with the higher abstraction level and coarse-grained modules is

MODULE / MCR	Master	3DA	3DG	3DM	3DAG	3DAM	3DAMG	PT	8ADC	2AF&ADC	BSDCC	BSLDCC	VI	PMM
Beccani et al, [31]	√	X	X	X	X	X	X	X	X	√	X	X	X	√
Beccani et al, [32]	√	√	X	X	X	X	X	√	√	X	X	X	X	√
Di Natali et al, [36]	√	√	X	X	X	X	X	X	X	X	X	X	X	√
Beccani et al, [37]	√	X	X	X	X	X	X	X	X	X	√	X	X	√
Wade et al, [38]	√	X	X	X	X	X	√ (2)	X	√	X	X	X	X	√
Carta et al, [94]	√	X	X	X	X	X	X	X	X	X	√	X	X	√
Tortora et al, [21]	√	X	X	X	X	X	X	X	X	X	√	X	X	√
De Falco et al, [12]	√	X	X	X	X	X	X	X	X	X	√	X	√	√
Valdastri et al, [22]	√	X	X	X	X	X	X	X	X	X	X	√	X	√
Valdastri et al, [40]	√	X	X	X	X	X	X	X	X	X	X	√	X	√
Simi et al, [19]	√	X	X	X	X	X	X	X	X	X	X	√	X	√
Chen et al, [95]	√	X	X	X	X	X	X	X	X	X	X	√	√	√
Ciuti et al, [96]	√	√	X	X	X	X	X	X	X	X	X	X	X	√
Ciuti et al, [20]	√	√	X	X	X	X	X	X	X	X	√	X	X	√
Yim et al, [97]	√	X	X	X	X	X	X	X	√	X	X	X	√	√
Miller et al, [98]	√	X	X	X	X	X	X	X	√	X	X	X	√	√
Cavallotti et al, [52]	√	X	X	X	X	X	X	X	X	X	√	X	√	√
Valdastri et al, [99]	√	X	X	X	X	X	X	X	X	X	X	√	√	√
Al-Rawhani et al, [100]	√	X	X	X	X	X	X	X	X	√	X	X	√	√
Valdastri et al, [101]	√	X	X	X	X	X	X	X	X	X	X	√	X	√
Quaglia et al, [15]	√	X	X	X	X	X	X	X	X	X	X	X	X	√
Woods et al, [13]	√	X	X	X	X	X	X	X	√	√	X	√	√	√
Chen et al, [14]	√	X	X	X	√	X	X	X	X	X	X	√	X	√
Nagy et al, [102]	√	X	X	X	X	X	X	X	X	X	X	√	X	√
Tortora et al, [28]	√	X	X	X	X	X	X	X	X	X	X	√	√	√
Lehman et al, [30]	√	X	X	X	X	X	X	X	X	X	X	√	√	√
Platt et al, [25]	√	X	X	X	X	X	X	X	X	X	√	X	√	√
Liu et al, [26]	√	X	X	X	X	X	√	X	X	X	X	X	√	√
Zazzarini et al, [29]	√	X	X	X	X	X	X	X	X	√	X	√	√	√

Table VI.1: The modules required to implement the MCRs reported in the literature.

to provide a truly intuitive and rapid design-space exploration tool with analysis, simulation and synthesis capabilities. Note that, in contrast with the lower-level more generic TinyOS component model, these modeling abstractions will target MCRs and our hardware ecosystem specifically.

The proposed approach for rapid prototyping of capsule robots follows the "democratization" of embedded systems promoted by the introduction of Arduino and other open source platforms, and lends itself to adoption well beyond medical research. While it is too soon to speculate on the broader implications of the adoption of our approach, we hope that lowering the barriers to the design of new medical capsule robots will lead to a day when colorectal cancer screening will be as easy as swallowing a capsule.

Bibliography

[1] S. P. R., , O. K. L., and V. P., "Technical research update in capsule endoscopy," *World Journal of Gastroenterology*, vol. 21, pp. 10 528–10 541, 10 2010.

[2] A. C. Society:, "Available from: www.cancer.org," accessed on 28 June 2014.

[3] T. O'Callaghan, "Introduction: The prevention agenda," *Nature*, vol. 471, no. 7339, pp. S2–S4, 2011.

[4] D. A. Joseph, A. S. DeGroff, N. S. Hayes, F. L. Wong, and M. Plescia, "The Colorectal Cancer Control Program: partnering to increase population level screening," *Gastrointestinal Endoscopy*, vol. 73, no. 3, pp. 429–434, Dec. 2014.

[5] G. Iddan, G. Meron, A. Glukhovsky, and S. P., "Wireless capsule endoscopy," *Nature*, vol. 405, no. 6785, pp. 417–418, 2000.

[6] G. Imaging, "Available from: http://www.givenimaging.com," accessed on 28 June 2014.

[7] Medimetrics, "Available from: http://medimetrics.com/home," accessed on 30 November 2015.

[8] P. Valdastri, M. Simi, and R. J. Webster III, "Advanced technologies for gastrointestinal endoscopy," *Annual Review of Biomedical Engineering*, vol. 14, no. 5, pp. 397–429, 2012.

[9] L. J. Sliker and G. Ciuti, "Flexible and capsule endoscopy for screening, diagnosis and treatment," *Expert review of medical devices*, vol. 11, no. 6, pp. 649–666, 2014.

[10] P. Slawinski, K. L. Obstein, and P. Valdastri, "Emerging issues and future developments in capsule endoscopy," *Techniques in Gastrointestinal Endoscopy*, 2015, in press, available on-line.

[11] P. Valdastri, G. Ciuti, A. Verbeni, A. Menciassi, P. Dario, A. Arezzo, and M. Morino, "Magnetic air capsule robotic system: proof of concept of a novel approach for painless colonoscopy," *Surgical Endoscopy*, vol. 26, no. 5, pp. 1238–1246, 2012.

[12] I. De Falco, G. Tortora, P. Dario, and A. Menciassi, "An Integrated System for Wireless Capsule Endoscopy in a liquid-distended Stomach." *IEEE Trans. Bio-Med. Eng.*, vol. 61, no. 3, pp. 794–804, 2013.

[13] S. P. Woods and T. G. Constandinou, "Wireless capsule endoscope for targeted drug delivery: mechanics and design considerations," *IEEE Trans. Bio-Med. Eng.*, vol. 60, no. 4, pp. 945–953, 2013.

[14] Y. Chen, J. Liang, and I. W. Hunter, "Modular continuum robotic endoscope design and path planning," in *Robotics and Automation (ICRA), 2014 IEEE International Conference on*, 2014, pp. 5393–5400.

[15] C. Quaglia, S. Tognarelli, E. Sinibaldi, N. Funaro, P. Dario, and A. Menciassi, "Wireless robotic capsule for releasing bioadhesive patches in the gastrointestinal tract," *Journal of Medical Devices*, vol. 8, no. 1, p. 014503, 2014.

[16] P. Valdastri, R. J. Webster, C. Quaglia, M. Quirini, A. Menciassi, and P. Dario, "A new mechanism for mesoscale legged locomotion in compliant tubular environments," *Robotics, IEEE Transactions on*, vol. 25, no. 5, pp. 1047–1057, 2009.

[17] G. Ciuti, P. Valdastri, A. Menciassi, and P. Dario, "Robotic magnetic steering and locomotion of capsule endoscope for diagnostic and surgical endoluminal procedures," *Robotica*, vol. 28, no. 2, pp. 199–207, 2010.

[18] G. Ciuti, A. Menciassi, and P. Dario, "Capsule endoscopy: from current achievements to open challenges," *Biomedical Engineering, IEEE Reviews in*, vol. 4, pp. 59–72, 2011.

[19] M. Simi, P. Valdastri, C. Quaglia, A. Menciassi, and P. Dario, "Design, fabrication, and testing of a capsule with hybrid locomotion for gastrointestinal tract exploration," *IEEE/ASME Trans. Mechatronics*, vol. 15, no. 2, pp. 170–180, 2010.

[20] G. Ciuti, N. Pateromichelakis, M. Sfakiotakis, P. Valdastri, a. Menciassi, D. Tsakiris, and P. Dario, "A wireless module for vibratory motor control and inertial sensing in capsule endoscopy," *Sensors and Actuators A: Physical*, vol. 186, pp. 270–276, 2012.

[21] G. Tortora, P. Valdastri, E. Susilo, A. Menciassi, P. Dario, F. Rieber, and M. O. Schurr, "Propeller-based wireless device for active capsular endoscopy in the gastric district," *Minimally invasive therapy & allied technologies: MITAT : official journal of the Society for Minimally Invasive Therapy*, vol. 18, no. 5, pp. 280–90, 2009.

[22] P. Valdastri, E. Sinibaldi, S. Caccavaro, G. Tortora, A. Menciassi, and P. Dario, "A novel magnetic actuation system for miniature swimming robots," *IEEE Trans. Robot.*, vol. 27, no. 4, pp. 769–779, 2011.

[23] P. Valdastri, C. Quaglia, E. Susilo, A. Menciassi, P. Dario, C. Ho, G. Anhoeck, and M. Schurr, "Wireless therapeutic endoscopic capsule: in vivo experiment," *Endoscopy*, vol. 40, no. 12, p. 979, 2008.

[24] T. Hu, P. K. Allen, N. J. Hogle, and D. L. Fowler, "Insertable Surgical Imaging Device with Pan, Tilt, Zoom, and Lighting," *The International Journal of Robotics Research*, vol. 28, no. 10, pp. 1373–1386, 2009.

[25] S. Platt, J. Hawks, and M. Rentschler, "Vision and task assistance using modular wireless in vivo surgical robots," *Biomedical Engineering, IEEE Transactions on*, vol. 56, no. 6, pp. 1700–1710, 2009.

[26] X. Liu, G. J. Mancini, and J. Tan, "Capsule-shaped Laparoscopic Camera System," in *Robotics and Automation (ICRA), 2014 IEEE International Conference on*, 2014, pp. 2449–2456.

[27] D. Canes, A. C. Lehman, S. Farritor, D. Oleynikov, and M. M. Desai, "The future of NOTES instrumentation: flexible robotics and in vivo minirobots," *Journal of Endourology*, vol. 23, no. 5, pp. 787–792, 2009.

[28] G. Tortora, P. Dario, and A. Menciassi, "Array of robots augmenting the kinematics of endocavitary surgery," *IEEE/ASME Trans. Mechatronics*, vol. 19, no. 6, pp. 1821–1829, 2014.

[29] C. C. Zazzarini, P. Patete, G. Baroni, and P. Cerveri, "Mechatronic design of a fully integrated camera for mini-invasive surgery." *IEEE Trans. Bio-Med. Eng.*, vol. 60, no. 6, pp. 1538–1545, 2013.

[30] A. C. Lehman, J. Dumpert, N. A. Wood, L. Redden, A. Q. Visty, S. Farritor, B. Varnell, and D. Oleynikov, "Natural orifice cholecystectomy using a miniature robot," *Surgical Endoscopy*, vol. 23, no. 2, pp. 260–266, 2009.

[31] M. Beccani, C. Di Natali, M. Rentschler, and P. Valdastri, "Wireless tissue palpation: Proof of concept for a single degree of freedom," in *Robotics and Automation (ICRA), 2013 IEEE International Conference on*, 2013, pp. 711–717.

[32] M. Beccani, C. Di Natali, L. Sliker, J. Schoen, M. Rentschler, and P. Valdastri, "Wireless tissue palpation for intraoperative detection of lumps in soft tissue," *IEEE Trans. Bio-Med. Eng.*, vol. 61, no. 99, pp. 353–361, 2013.

[33] M. Beccani, C. Di Natali, N. E. Hall, C. E. Benjamin, C. S. Bell, and P. Valdastri, "Wireless tissue palpation: characterization of the probe head to improve detection of tumors in soft tissue," *Procedia Engineering*, vol. 87, pp. 352–355, 2014.

[34] M. Beccani, C. Di Natali, C. E. Benjamin, C. S. Bell, N. E. Hall, and P. Valdastri, "Wireless tissue palpation: Head characterization to improve tumor detection in soft tissue," *Sensors and Actuators A: Physical*, vol. 223, pp. 180–190, 2015.

[35] C. Di Natali, M. Beccani, and P. Valdastri, "Real-time pose detection for magnetic medical devices," *Magnetics, IEEE Transactions on*, vol. 49, no. 7, pp. 3524–3527, 2013.

[36] C. Di Natali, M. Beccani, K. L. Obstein, and P. Valdastri, "A wireless platform for in vivo measurement of resistance properties of the gastrointestinal tract." *Physiological measurement*, vol. 35, no. 7, pp. 1197–1214, 2014.

[37] M. Beccani, C. Di Natali, A. Gregorio, B. Claire, and P. Valdastri, "A magnetic drug delivery capsule based on a coil actuation mechanism," *Procedia Engineering*, 2015, in press.

[38] W. Joshua, M. Beccani, A. Myszka, E. Bekele, P. Valdastri, P. Flemming, M. De Riesthal, T. Withrow, and N. Sarkar, "Design and implementation of an instrumented cane for gait recognition," in *in proceedings of IEEE International Conference on Robotics and Automation - ICRA 2015*, 2015, in press.

[39] S. Yim and M. Sitti, "Design and rolling locomotion of a magnetically actuated soft capsule endoscope," *IEEE Trans. Robot.*, vol. 28, no. 1, pp. 183–194, 2012.

[40] P. Valdastri, R. J. Webster, C. Quaglia, M. Quirini, A. Menciassi, and P. Dario, "A new mechanism for mesoscale legged locomotion in compliant tubular environments." *IEEE Trans. Robot.*, vol. 25, no. 5, pp. 1047–1057, 2009.

[41] P. Valdastri, E. Susilo, T. Förster, C. Strohhöfer, A. Menciassi, and P. Dario, "Wireless implantable electronic platform for blood glucose level monitoring." in *Sensors and Actuators A: Physical*, 2009, pp. 1255–1258.

[42] D. C. G. for Medical Device Manufactures, "Available from: http://www.fda.gov," accessed on 28 June 2014.

[43] J. Hatcliff, A. King, I. Lee, A. Macdonald, A. Fernando, M. Robkin, E. Vasserman, S. Weininger, and J. M. Goldman, "Rationale and Architecture Principles for Medical Application Platforms," in *2012 IEEE/ACM Third International Conference on Cyber-Physical Systems*, 2012, pp. 3–12.

[44] I. C. on Non-Ionizing Radiation Protection *et al.*, "Guidelines for limiting exposure to time-varying electric, magnetic, and electromagnetic fields," *Health Physics*, vol. 97, no. 3, pp. 257–258, 2009.

[45] C. finds open source software quality better than proprietary code, "Available from: http://www.zdnet.com," accessed on 28 June 2014.

[46] C. Scan, "Available from: https://scan.coverity.com/projects," accessed on 28 June 2014.

[47] D. Halperin, T. Heydt-Benjamin, B. Ransford, S. Clark, B. Defend, W. Morgan, K. Fu, T. Kohno, and W. Maisel, "Pacemakers and implantable cardiac defibrillators: Software radio attacks and zero-power defenses," in *Security and Privacy, 2008. SP 2008. IEEE Symposium on*, 2008, pp. 129–142.

[48] J. L. Toennies, G. Tortora, M. Simi, P. Valdastri, and R. J. Webster III, "Swallowable medical devices for diagnosis and surgery: the state of the art," *Proceedings of the Institution of Mechanical Engineers, Part C: Journal of Mechanical Engineering Science*, vol. 224, no. 7, pp. 1397–1414, 2010.

[49] T. Instruments, "Available from: http://www.ti.com," accessed on 28 June 2014.

[50] P. Valdastri, A. Menciassi, and P. Dario, "Transmission power requirements for novel ZigBee implants in the gastrointestinal tract," *Biomedical Engineering, IEEE Transactions on*, vol. 55, no. 6, pp. 1705–1710, 2008.

[51] P. Valdastri, A. Menciassi, A. Arena, C. Caccamo, and P. Dario, "An implantable telemetry platform system for in vivo monitoring of physiological parameters," *IEEE Trans. Inf. Technol. Biomed.*, vol. 8, no. 3, pp. 271–278, 2004.

[52] C. Cavallotti, M. Piccigallo, E. Susilo, P. Valdastri, A. Menciassi, and P. Dario, "An integrated vision system with autofocus for wireless capsular endoscopy," *Sensors and Actuators A: Physical*, vol. 156, no. 1, pp. 72–78, 2009.

[53] R. LINKS, "Available from: http://rf-links.com," accessed on 28 June 2014.

[54] M. Ltd, "Available from: http://www.smallestvideocameras.com," accessed on 09 September 2014.

[55] I. SYSTEMS, "Available from: http://www.iar.com," accessed on 28 June 2014.

[56] Eclipse, "Available from: http://www.eclipse.org," accessed on 28 June 2014.

[57] W. P. A. N. Standards, "Available from: http://standards.ieee.org," accessed on 28 June 2014.

[58] P. Bogónez-Franco, R. Bragós, a. Bayés-Genis, and J. Rosell-Ferrer, "Implantable bioimpedance monitor using ZigBee." *Conference proceedings : Annual International Conference of the IEEE Engineering in Medicine and Biology Society. IEEE Engineering in Medicine and Biology Society*, pp. 4868–71, 2009.

[59] P. Levis, S. Madden, J. Polastre, R. Szewczyk, K. Whitehouse, A. Woo, D. Gay, J. Hill, M. Welsh, E. Brewer, and D. Culler, *TinyOS: An Operating System for Sensor Networks*, W. Weber, J. Rabaey, and E. Aarts, Eds. Springer Berlin Heidelberg, pp. 115-148, 2005.

[60] P. Valdastri, A. Menciassi, and P. Dario, "Transmission power requirements for novel zigbee implants in the gastrointestinal tract," *IEEE Trans. Bio-Med. Eng.*, vol. 55, no. 6, pp. 1705–10, 2008.

[61] E. Susilo, P. Valdastri, A. Menciassi, and P. Dario, "A miniaturized wireless control platform for robotic capsular endoscopy using advanced pseudokernel approach," *Sensors and Actuators A: Physical*, vol. 156, no. 1, pp. 49–58, 2009.

[62] P. Dario and M. Bergamasco, "An advanced robot system for automated diagnostic tasks through palpation," *Biomedical Engineering, IEEE Transactions on*, vol. 35, no. 2, pp. 118–126, 1988.

[63] R. Howe, W. Peine, D. Kantarinis, and J. Son, "Remote palpation technology," *IEEE Engineering in Medicine and Biology*, vol. 14, no. 3, pp. 318–323, 1995.

[64] T. Ohtsuka, A. Furuse, T. Kohno, J. Nakajima, K. Yagyu, and S. Omata, "Application of a new tactile sensor to thoracoscopic surgery: Experimental and clinical study," *The Annals of Thoracic Surgery*, vol. 60, no. 3, pp. 610–614, 1995.

[65] M. Ottensmeyer and J. Salisbury, "In vivo data acquisition instrument for solid organ mechanical property measurement," in *Medical Image Computing and Computer-Assisted Intervention – MICCAI 2001*. Springer, 2001, pp. 975–982.

[66] E. Samur, M. Sedef, C. Basdogan, L. Avtan, and O. Duzgun, "A robotic indenter for minimally invasive measurement and characterization of soft tissue response," *Medical Image Analysis*, vol. 11, no. 4, pp. 361–373, 2007.

[67] J. Rosen, J. Brown, S. De, M. Sinanan, and B. Hannaford, "Biomechanical properties of abdominal organs in vivo and postmortem under compression loads," *Journal of Biomechanical Engineering*, vol. 130, no. 021020, pp. 1–17, 2008.

[68] K. Lister, Z. Gao, and J. Desai, "Development of in vivo constitutive models for liver: Application to surgical simulation," *Annals of Biomedical Engineering*, vol. 39, pp. 1060–1073, 2011.

[69] P. Puangmali, H. Liu, L. Seneviratne, P. Dasgupta, and K. Althoefer, "Miniature 3-axis distal force sensor for minimally invasive surgical palpation," *Mechatronics, Transaction on IEEE*, vol. 17, no. 4, pp. 646–656, 2012.

[70] O. Van der Meijden and M. Schijven, "The value of haptic feedback in conventional and robot-assisted minimal invasive surgery and virtual reality training: a current review," *Surgical Endoscopy*, vol. 23, pp. 1180–1190, 2009.

[71] G. Tholey and J. P. Desai, "A compact and modular laparoscopic grasper with tri-directional force measurement capability," *ASME Journal of Medical Devices*, vol. 2, no. 3, pp. 031 001–9, 2008.

[72] B. Kübler, U. Seibold, and G. Hirzinger, "Development of actuated and sensor integrated forceps for minimally invasive robotic surgery," *The International Journal of Medical Robotics and Computer Assisted Surgery*, vol. 1, no. 3, pp. 96–107, 2005.

[73] M. Stark, T. Benhidjeb, S. Gidaro, and E. Morales, "The future of telesurgery: a universal system with haptic sensation," *Journal of the Turkish-German Gynecological Association*, vol. 13, no. 1, pp. 74–76, 2012.

[74] H. Liu, J. Li, X. Song, L. Seneviratne, and K. Althoefer, "Rolling indentation probe for tissue abnormality identification during minimally invasive surgery," *Robotics, IEEE Transactions on*, vol. 27, no. 3, pp. 450–460, 2011.

[75] J. Gwilliam, Z. Pezzementi, E. Jantho, A. Okamura, and S. Hsiao, "Human vs. robotic tactile sensing: Detecting lumps in soft tissue," in *IEEE Haptics Symposium*, 2010, pp. 21–28.

[76] G. McCreery, A. Trejos, M. Naish, R. Patel, and R. Malthaner, "Feasibility of locating tumours in lung via kinaesthetic feedback." *The International Journal of Medical Robotics and Computer Assisted Surgery*, vol. 4, no. 1, pp. 58–68, 2008.

[77] R. E. Goldman, A. Bajo, and N. Simaan, "Algorithms for autonomous exploration and estimation in compliant environments," *Robotica*, vol. 31, no. 1, pp. 71–87, 2013.

[78] P. Culmer, J. Barrie, R. Hewson, M. Levesley, M. Mon-Williams, D. Jayne, and A. Neville, "Reviewing the technological challenges associated with the development of a laparoscopic palpation device," *The International Journal of Medical Robotics and Computer Assisted Surgery*, vol. 8, no. 2, pp. 146–159, 2012.

[79] B. Laulicht, N. J. Gidmark, A. Tripathi, and E. Mathiowitz, "Localization of magnetic pills," *Proceedings of the National Academy of Sciences*, vol. 108, no. 6, pp. 2252–2257, 2011.

[80] E. P. Furlani, *Permanent Magnet and Electromechanical Devices*. Academic Press, 2001, pp. 131–135.

[81] S. R. Platt, J. A. Hawks, and M. E. Rentschler, "Vision and task assistance using modular wireless in vivo surgical robots," *Biomedical Engineering, IEEE Transactions on*, vol. 56, no. 6, pp. 1700–1710, 2009.

[82] C. Song, A. Alijani, T. Frank, G. Hanna, and A. Cuschieri, "Mechanical properties of the human abdominal wall measured in vivo during insufflation for laparoscopic surgery," *Surgical Endoscopy*, vol. 20, no. 6, pp. 987–990, 2006.

[83] C. Di Natali, T. Ranzani, M. Simi, A. Menciassi, and P. Valdastri, "Trans-abdominal active magnetic linkage for robotic surgery: Concept definition and model assessment," in *Robotics and Automation (ICRA), IEEE International Conference on*, 2012, pp. 695–700.

[84] M. Kunkel, A. Moral, R. Westphal, D. Rode, M. Rilk, and F. Wahl, "Using robotic systems in order to determine biomechanical properties of soft tissues," in *Studies in Health Technology and Informatics, Proceedings of the 2nd Conference on Applied Biomechanics*, vol. 133, no. 3, 2008, p. 156.

[85] S. Yim and M. Sitti, "Design and rolling locomotion of a magnetically actuated soft capsule endoscope," *Robotics, IEEE Transactions on*, vol. 28, no. 1, pp. 183–194, 2012.

[86] A. W. Mahoney, D. L. Cowan, K. M. Miller, and J. J. Abbott, "Control of untethered magnetically actuated tools using a rotating permanent magnet in any position," in *Robotics and Automation (ICRA), IEEE International Conference on*, 2012, pp. 3375–3380.

[87] J. C. Gwilliam, Z. Pezzementi, E. Jantho, A. M. Okamura, and S. Hsiao, "Human vs. robotic tactile sensing: Detecting lumps in soft tissue," *2010 IEEE Haptics Symposium*, pp. 21–28, 2010.

[88] M. T. Perri, A. L. Trejos, M. D. Naish, R. V. Patel, and R. A. Malthaner, "Initial evaluation of a tactile/kinesthetic force feedback system for minimally invasive tumor localization," *Mechatronics, IEEE Transactions on*, vol. 15, no. 6, pp. 925–931, 2010.

[89] A. Cucchetti, G. Ercolani, M. Cescon, E. Bigonzi, E. Peri, M. Ravaioli, and A. D. Pinna, "Impact of subcentimeter margin on outcome after hepatic resection for colorectal metastases: A meta-regression approach," *Surgery*, vol. 151, no. 5, pp. 691 – 699, 2012.

[90] S. L. Best, R. Bergs, M. Gedeon, J. Paramo, R. Fernandez, J. A. Cadeddu, and D. J. Scott, "Maximizing coupling strength of magnetically anchored surgical instruments: how thick can we go?" *Surgical Endoscopy*, vol. 25, no. 1, pp. 153–159, 2011.

[91] P. Valdastri, K. Harada, A. Menciassi, L. Beccai, C. Stefanini, M. Fujie, and P. Dario, "Integration of a miniaturised triaxial force sensor in a minimally invasive surgical tool," *Biomedical Engineering, IEEE Transaction on*, vol. 53, no. 11, pp. 2397–2400, 2006.

[92] Y. Hu, R. Katragadda, H. Tu, Q. Zheng, Y. Li, and Y. Xu, "Bioinspired 3-D tactile sensor for minimally invasive surgery," *Journal of Microelectromechanical Systems*, vol. 19, no. 6, pp. 1400–1408, 2010.

[93] P. Wellman and R. Howe, "Extracting features from tactile maps," in *Medical Image Computing and Computer-Assisted Intervention MICCAI99*, vol. 1679, 1999, pp. 1133–1142.

[94] R. Carta, G. Tortora, J. Thoné, B. Lenaerts, P. Valdastri, A. Menciassi, P. Dario, and R. Puers, "Wireless powering for a self-propelled and steerable endoscopic capsule for stomach inspection," *Sensors and Actuators A: Physical*, vol. 25, no. 4, pp. 845–51, 2009.

[95] W. Chen, G. Yan, Z. Wang, P. Jiang, and H. Liu, "A wireless capsule robot with spiral legs for human intestine," *The International Journal of Medical Robotics and Computer Assisted Surgery*, vol. 10, no. 2, pp. 147–161, 2014.

[96] G. Ciuti, P. Valdastri, A. Menciassi, and P. Dario, "Robotic magnetic steering and locomotion of capsule endoscope for diagnostic and surgical endoluminal procedures," *Robotica*, vol. 28, no. 02, p. 199, 2009.

[97] S. Yim and M. Sitti, "3-D localization method for a magnetically actuated soft capsule endoscope and its applications," *IEEE Trans. Robot.*, vol. 29, no. 5, pp. 1139–1151, 2013.

[98] K. M. Miller, M. A. W., T. Schmid, and J. J. Abbott, "Proprioceptive magnetic-field sensing for closed-loop control of magnetic capsule endoscopes," in *2012 IEEE/RSJ International Conference on Intelligent Robots and Systems*, 2012.

[99] P. Valdastri, C. Quaglia, E. Buselli, A. Arezzo, N. Di Lorenzo, M. Morino, A. Menciassi, and P. Dario, "A magnetic internal mechanism for precise orientation of the camera in wireless endoluminal applications," *Endoscopy*, vol. 42, no. 6, pp. 481–486, 2010.

[100] M. A. Al-Rawhani, D. Chitnis, J. Beeley, S. Collins, and D. R. Cumming, "Design and implementation of a wireless capsule suitable for autofluorescence intensity detection in biological tissues," *IEEE Trans. Bio-Med. Eng.*, vol. 60, no. 1, pp. 55–62, 2013.

[101] P. Valdastri, C. Quaglia, E. Susilo, A. Menciassi, P. Dario, C. N. Ho, G. Anhoeck, and M. O. Schurr, "Wireless therapeutic endoscopic capsule: in vivo experiment," *Endoscopy*, vol. 40, no. 12, p. 979, 2008.

[102] Z. Nagy, M. Flückiger, R. Oung, I. K. Kaliakatsos, E. W. Hawkes, B. J. Nelson, E. Susilo, A. Menciassi, P. Dario, and J. J. Abbott, "Assembling reconfigurable endoluminal surgical systems : opportunities and challenges," *Int. J. Biomechatronics and Biomedical Robotics*, vol. 1, no. 1, 2009.